공학박사 학위논문

Transition of Electrochemical Lithium Recovery (ELR) to a Continuous System through Engineering Design

공학적 설계를 통한 전기화학적 리튬 회수 방식의 연속식 시스템으로의 전환

2023년 2월

서울대학교 대학원

화학생물공학부

주 화 주

Transition of Electrochemical Lithium Recovery (ELR) to a Continuous System through Engineering Design

by

Hwajoo Joo

under the supervision of

Professor Jeyong Yoon, Ph. D.

A dissertation submitted in partial fulfillment of the requirements for

the Degree of Doctor of Philosophy

February 2023

SCHOOL OF CHEMICAL AND BIOLOGICAL

ENGINEERING

SEOUL NATIONAL UNIVERSITY

Transition of Electrochemical Lithium Recovery (ELR) to a Continuous System through Engineering Design

공학적 설계를 통한 전기화학적 리튬 회수 방식의 연속식 시스템으로의 전환

지도교수 윤 제 용

이 논문을 공학박사 학위논문으로 제출함

2023년 2월

서울대학교 대학원

공과대학 화학생물공학부

주 화 주

주화주의 공학박사 학위논문을 인준함

2023년 1월

위 원 장 이 규 태 (인)

부 위 원 장 윤 제 용 (인)

위 원 이 창 하 (인)

위 원 이 재 한 (인)

위 원 정 선 엽 (인)

Abstract

Transition of Electrochemical Lithium Recovery (ELR) to a Continuous System through Engineering Design

Hwajoo Joo

School of Chemical and Biological Engineering

The Graduates School

Seoul National University

The climate crisis is approaching reality, and the development of carbon neutral engineering technologies is necessary to respond to it. Electrochemical ion separation (EIONS) technology, one of carbon neutral engineering, is an eco-friendly method for securing water and salt resources. Meanwhile, as the demand for lithium explodes due to the rapid growth of the electric vehicle market, the supply and the demand of lithium are becoming unstable. To respond to this, it is necessary to develop a lithium recovery technology that is faster than existing technologies based on slow solar evaporation.

Electrochemical lithium recovery (ELR) technology is an EIONS technology that satisfies this characteristic. For ELR to become an alternative technology with technological advantage, it must include a continuous process that can rapidly and flexibly to the skyrocketing lithium demand. However, most existing studies are still in the proof-of-concept stage of suggesting a new configuration of electrode pairs under a batch system, and only a few systematic studies on the continuous system

have been conducted. In this study, to convert the ELR process from a batch to a continuous configuration, new systems and reactors were developed that consider the properties of the continuity by the two ways.

First, a pilot-scale ELR system based on a continuous stirred tank reactor (CSTR) was developed as a post-process for treating desalination concentrate. In order to treat a large amount of desalination concentrate containing high concentration of impurity by using an automated system and to facilitate maintenance, a mobile-type electrode configuration in which the electrode moves around the water tank was developed.

Second, an LMO-based flow-type rocking-chair ELR system operating in constant current mode, which is a fully continuous system in which Li^+ capturing and desorption occur simultaneously to produce a solution of uniform quality, was proposed for the first time. The existing 1D computational simulation was expanded to 2D for the analysis of the new system, and the electrode design guideline was developed by analyzing the effects of three electrode design parameters on performance.

This study is significant in that it confirmed the possibility of continuous configuration of the ELR system and led the ELR reactor engineering as shown in **graphical abstract of the dissertation**. I hope that engineering design developed in this study will improve the technological maturity of the ELR system and help commercialization in the future.

Keywords: Electrochemical ion separation (EIONS); Electrochemical lithium recovery (ELR); Continuous system; Engineering design; Mobile-type electrode; Electrode design guideline

Student number: 2016-24679

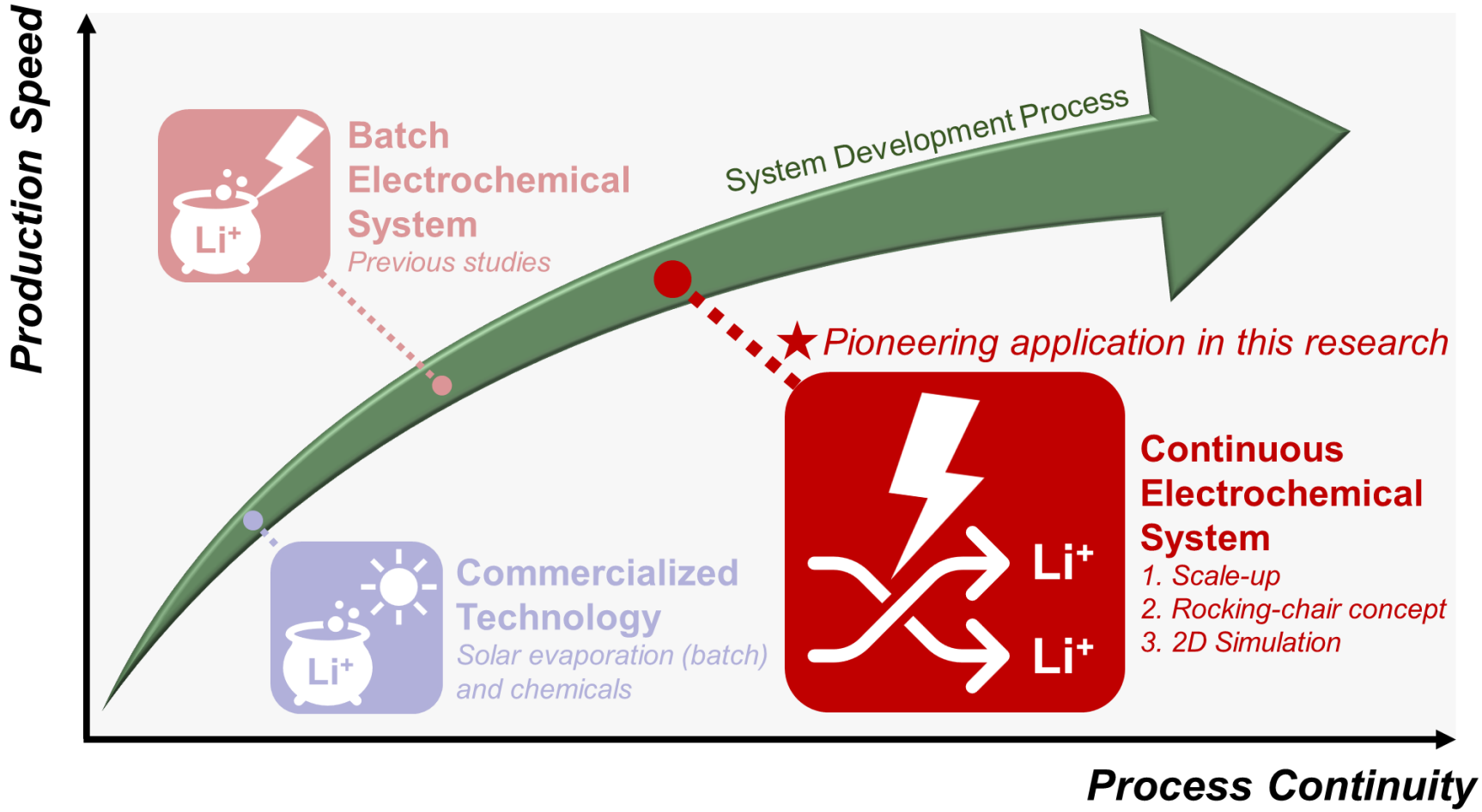

Graphical abstract of the dissertation

Table of Contents

List of figures

List of tables

1. Introduction

1.1. Research background

The world is terrified by the threat of the climate crisis (Magnan et al. 2021). Unpredictable climatic events such as heatwaves, heavy snowfalls, and floods occur so frequently that they become commonplace (Chiang et al. 2021; Ulrich 2022; Rousi et al. 2022). It is no wonder that many countries around the world are trying to reduce their greenhouse gas emissions, the main culprit of climate change, to zero within a few decades. In other words, the transition into a carbon neutral (or net zero) era is taking place (Fankhauser et al. 2022; Meinshausen et al. 2022). For the carbon neutral era, carbon neutral engineering-based technology is essential (Joo and Yoon 2022). These technologies not only do not emit greenhouse gases but also can respond to revolutionary changes in the carbon neutral era such as electrification and circular economy. For securing water and salt resources, electrochemical ion separation (EIONS) corresponds to carbon neutral engineering technology, since EIONS technology is operated based on electric energy rather than chemical substances and thermal energy (Yoon et al. 2019).

Meanwhile, the market for electric vehicles (EV) and energy storage systems (ESS) is growing explosively due to the carbon neutral transition

(Ghosh 2020; Yu et al. 2020). Demand for lithium, a raw material for lithium-ion batteries, is also increasing to an unsustainable level (Tang et al. 2021; Calvo 2021). However, since the currently commercialized lime soda evaporation method includes a solar evaporation process that takes more than one year, there is a clear limit to the production speed of lithium resources (Kim et al. 2015b, 2019). Recently, electrochemical lithium recovery (ELR) has been attracting attention to solve this problem. This technology is a representative EIONS, and the ELR system can produce lithium rapidly and environmentally friendly by using electric energy (Yoon et al. 2019; Battistel et al. 2020; Joo et al. 2020b).

For the industrial application of the ELR technology, the continuous system should be designed to produce lithium continuously on a large-scale (Maljuric et al. 2020). However, most of the existing research has been conducted under the batch-type system, which is difficult to apply industrially (Pasta et al. 2012; Lee et al. 2013; Trócoli et al. 2014; Kim et al. 2018b; Lawagon et al. 2018). These studies are in the proof-of-concept stage to propose a new electrode pair configuration (Joo et al. 2020b). To overcome the limitation of batch-type ELR system, the continuous ELR systems and reactors needs to be developed.

1.2. Objectives of the research

In this dissertation, the purpose is to translate the ELR system into a continuous system for industrial application. To achieve this goal, two engineering design approaches were adopted.

First, a pilot-scale ELR system including CSTR reactor configuration was developed. For this, engineering considerations were needed to increase the size of the ELR system and increase the amount of feedstock it can handle. To achieve this, a mobile-type electrode was developed and introduced. At the rear end of the actual desalination plant, the designed system was installed, operated, and treated 6 ton/day of actual desalination concentrate.

Second, an LMO-based flow-type rocking-chair ELR system was proposed for a fully structured continuous process. To understand this system, numerical simulation was introduced, and the independent effects of the three electrode design parameters were analyzed by the parameter study. A sensitivity analysis was also conducted to figure out the significance of each design parameter and provide the electrode design guideline.

2. Literature review

2.1. Existing lithium recovery technologies for the aqueous resources and their limitations

The most commercialized technology for recovering lithium in water is the lime soda evaporation method (Meshram et al. 2014). It is a method of producing lithium carbonate by evaporating and concentrating brine using solar heat, and then injecting lime and soda to precipitate impurity ions (**Figure 2-1**)(JOGMEC 2010; Fukuda 2019). This method is used in large-scale salt lakes, including Salar de Atacama in Chile, and currently plays a major role in lithium production (Cabello 2021). Since this method follows the traditional chemical process method, it has the advantage of high degree of completeness and reliability of the technology. However, it also has the following fatal disadvantages (Khalil et al. 2022).

First, evaporation takes a very long time, about 1 to 2 years. This period is highly influenced by the weather and may be longer due to less sunlight and less wind. As a result, the payback period of the initial investment is long and large-scale investment is difficult. Therefore, only eight salt lakes are currently developed and operated (Flexer et al. 2018). It is difficult to respond to the rapidly increasing demand for lithium due to delays in production,

which is inherent characteristic in the process, and this is the reason for the delay in the introduction of large-scale facilities (Zhao et al. 2023).

Composition of brine also adds to the difficulty. A high ratio of Mg to Li (over 6) increases the difficulty of process design (Zhang et al. 2019b). This is because Li^+ and Mg^{2+} have similar ionic radii and similar physical/chemical properties, making it difficult to separate them. In fact, during the precipitation process, about 30% of lithium is lost, and in severe cases up to 50% is lost (Flexer et al. 2018). This suggests that the separation efficiency for lithium of existing technique is not very high.

From a sustainability point of view, the technology is unattractive (Lee et al. 2013). In order to construct a reservoir that can efficiently receive solar heat, a large area of land is required. Site contamination due to high salt concentrations and additional contamination due to the use of chemicals in subsequent processes may occur (Chordia et al. 2022). In the trend of strengthening global regulations on environmental factors, this technology seems to have limitations.

Due to these limitations, solvent extraction, ion-sieve adsorption, membrane technology, and electrochemical processes are being studied as next-generation lithium extraction technologies (Song et al. 2017).

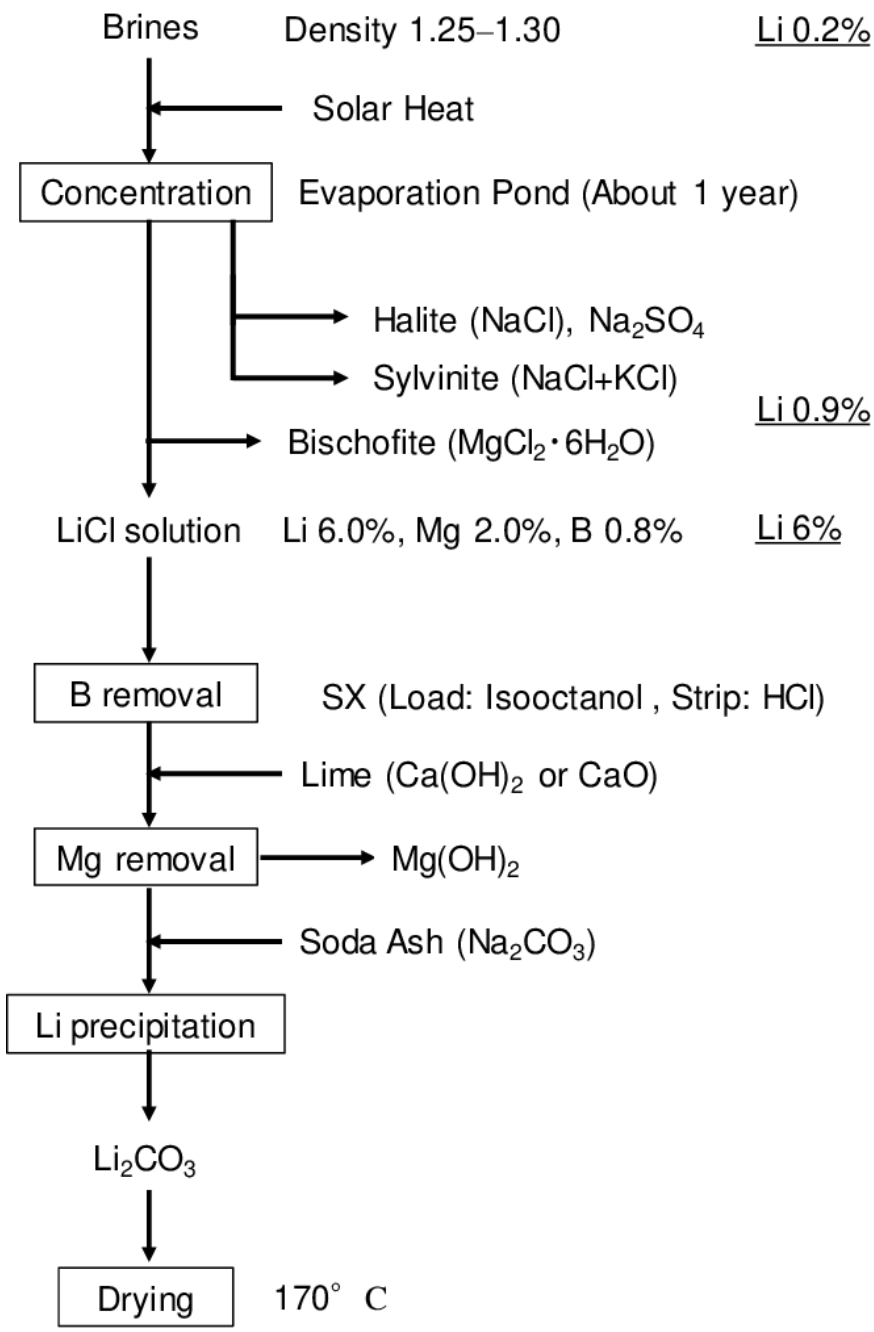

Figure 2-1 A representative flow of lithium carbonate production from brines (JOGMEC 2010)

2.2. Definition of ELR system and timeline of the research

The electrochemical lithium recovery (ELR) system, which is attracting attention as a next-generation lithium extraction technology, is an electrochemical process that separates and concentrates lithium-ion (Li^+) by using lithium selective electrodes (Pasta et al. 2012).

Figure 2-2 shows the operational principle of the ELR system using the spinel $LiMn_2O_4$ electrode. Generally, the system has an electrochemistry cell structure that consists of the working electrode (lithium-ion battery cathode) and the counter electrode. The system operates by repeated conduction of the following two steps. In Step 1, the Li^+ brine water source is inserted between the electrodes so that the system cell spontaneously discharges. This results in Li^+ intercalation into the lithium-ion battery cathode and the oxidation reaction on the counter electrode. After Step 1, the exhausted brine source is replaced by the recovery solution. When the charging current is applied (Step 2), Li^+ de-intercalates from the $LiMn_2O_4$ electrode as the reduction reaction occurs on the counter electrode. Li^+ then diffuses into the recovery solution, which concentrates the product. These two steps are conducted repeatedly until a Li^+ recovery solution with high concentration and purity is produced.

The representative cathode electrodes used for the ELR system are olivine LFP ($LiFePO_4$) and spinel LMO ($LiMn_2O_4$ or λ-MnO_2) (Xu et al. 2016, 2020). Both have sufficient reactivity with Li^+ and proper potential windows for lithium recovery. Yet compared to the LFP electrode, the LMO electrode shows much higher stability for repeated cycles with higher selectivity for Li^+, especially in the high Mg^{2+} concentration solution (Lee et al. 2013). Accordingly, the LMO-based ELR system has been studied more intensively than LFP and the LMO is considered a suitable material.

$LiMn_2O_4$ has a spinel structure which is corresponding with the Fd3m space group (Ooi et al. 1989). Spinel structure consists of three-dimensional pores that cause the steric effect. These small pores, which transport only Li^+, enable selective recovery of Li^+ (Ooi et al. 1988; Xu et al. 2016). $LiMn_2O_4$ has tetrahedral 8a sites for the Li^+, octahedral 16d sites for the Mn^{3+} and Mn^{4+}, and face-centered cubic (FCC) 32e sites for the oxygen anions (Greedan et al. 1998). Intercalation phenomena in the ELR system can be described by the redox mechanism (Ooi et al. 1991; Feng et al. 1992). At the electrochemical reduction step, the valence of the manganese cations is changed from +4 to +3 and Li^+ intercalates in the tetrahedral 8a sites. Contrary to this step, at the electrochemical oxidation step, the valence of the manganese cations is changed from +3 to +4, and Li^+ de-intercalates (Liu et al. 1998).

ELR systems using the LMO electrode are elucidated in this literature review. The timeline in **Figure 2-3** briefly summarizes the research history of ELR systems. The ELR research using the LMO electrode can be classified and discussed in 4 categories: system proposal, LMO electrode modification, system analysis, and application. After the discussion of the literatures, ELR system performance was arranged as a table and discussed further. Based on the trend and development process of the ELR system, the perspectives of ELR research were suggested.

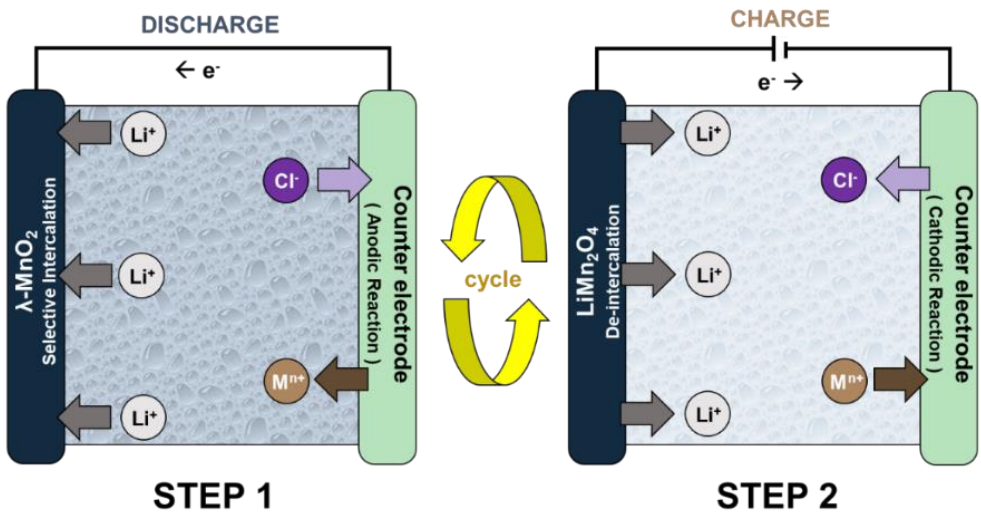

Figure 2-2 The operational principle of the electrochemical lithium recovery (ELR) systems (Joo et al. 2020b)

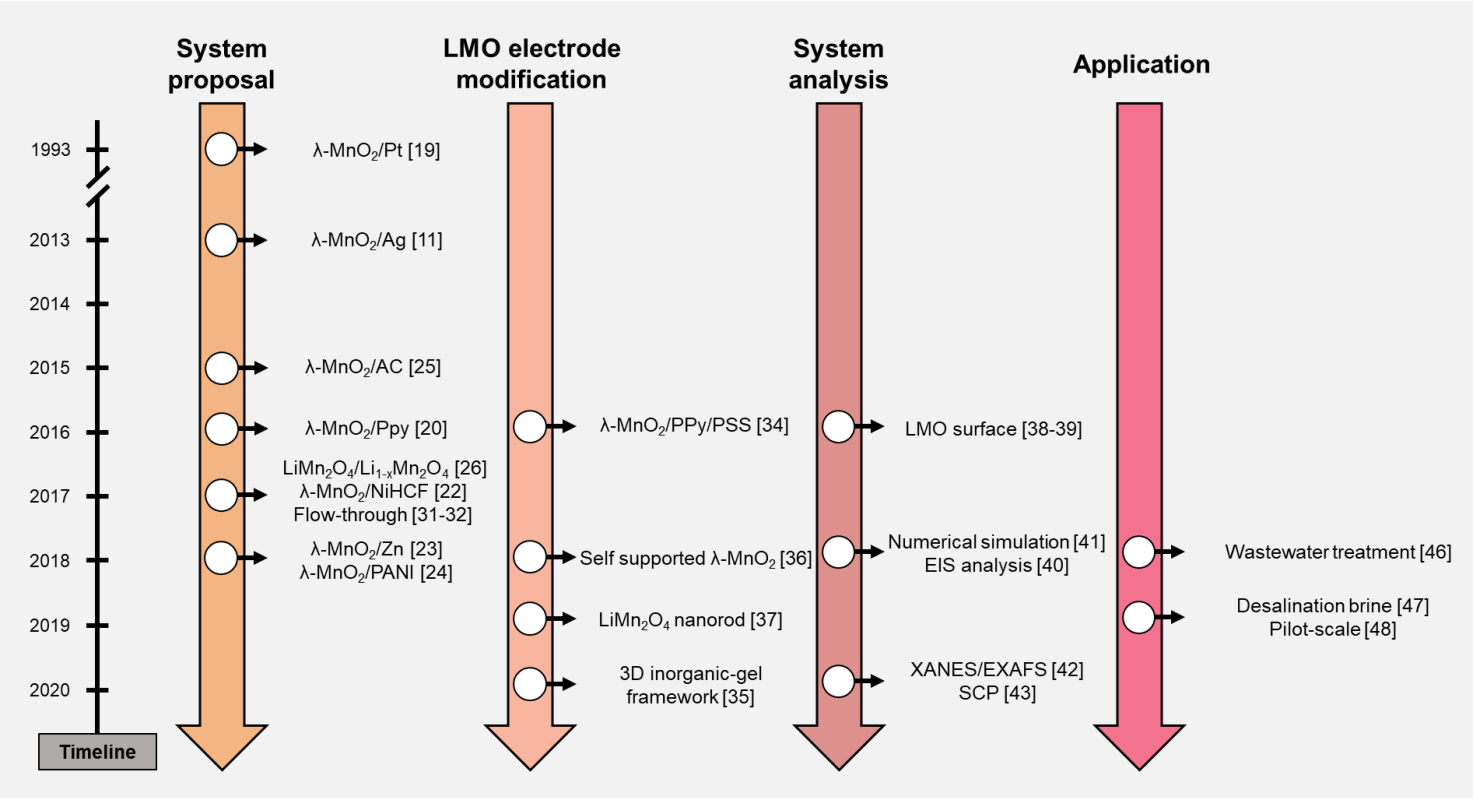

Figure 2-3 Timeline of the electrochemical lithium recovery (ELR) system research (Joo et al. 2020b)

2.3. System proposal

2.3.1 The system with the hydrolysis (λ-MnO_2/Pt system)

The first electrochemical lithium recovery (ELR) system was the λ-MnO_2/Pt system proposed in 1993 (Kanoh et al. 1991, 1993), which is a three-electrode cell consisting of a λ-MnO_2 electrode (working), Pt wire electrode (counter), and Calomel electrode (reference). Li^+ was selectively recovered by the forward sweep method (1.0 to 0.2 V, scan rate: 0.1 mV s^{-1}) of cyclic voltammetry. The lithium capturing reaction is as follows:

$$\lambda - MnO_2 + xLi^+ + xe^- \rightarrow Li_xMnO_2 \text{ (cathode)}$$

$$H_2O + e^- \rightarrow \frac{1}{2}H_2 + OH^- \text{ (hydrolysis, anode)}$$

Kanoh et al. investigated the lithium recovery performance of the λ-MnO_2/Pt system in aqueous solutions of various metal chlorides. From the results of these lithium recovery experiments, they found that the system showed remarkable Li^+ selectivity when the electrolyte contained more than 10 mM of Li^+ while insufficient performance was reported when the electrolyte contained less than 0.1 mM of Li^+. Expectedly, this system showed low energy efficiency due to the hydrolysis occurring at the Pt electrode surface. They also

reported that alkaline earth metal ions had stronger inhibitory effects on lithium recovery than alkaline metal ions due to the electrostatic interaction and complexation ability on the oxide surface. For a system application, lithium was recovered from the geothermal water and the uptake (similar to the capacity) was 11 mg g^{-1}. The first ELR system was well-defined by their pioneering work. Nevertheless, this system was needed to be refined because of the pH variation and high energy consumption that occurred by the hydrolysis.

2.3.2 Asymmetric battery system

For a high-energy efficient and reversible process without pH variation, Lee et al. reported the first battery-type ELR system consisting of a λ-MnO_2 electrode (positive electrode) and silver electrode (Ag, negative electrode) (Lee et al. 2013). The reversible lithium capturing/releasing reaction is as follows:

$$2\lambda - MnO_2 + xLi^+ + xe^- \leftrightarrow Li_xMn_2O_4 \text{ (positive electrode)}$$

$$xAg + xCl^- \leftrightarrow xAgCl + xe^- \text{ (negative electrode)}$$

The system was operated under constant-current mode. By repeating the two steps (capturing and releasing), Li^+ in the source solution was selectively transported to the recovery solution. In this study, an additional lithium recovery test was carried out from the simulated brine (similar to the Salar de Atacama) and the results showed that lithium was selectively recovered with efficient energy consumption (specific energy consumption: 1.0 Wh mol^{-1}). The research on the battery-type ELR system using the LMO was done based on this research. Certain follow-up studies have focused on developing alternatives to the silver electrode due to its high cost. Materials such as polypyrrole (PPy), nickel hexacyanoferrate (NiHCF), zinc, and polyaniline (PANI) were suggested as alternatives. These materials showed enough

electrical capacity, good reversibility, high stability, and high current efficiency to the targeted counter-reaction.

In the study conducted by Massoni et al., PPy, the reversible chloride capturing electrode, was applied to the ELR system (Missoni et al. 2016). The PPy electrode captured and released Cl^- with high reversibility and stability in the natural brine. The reversible chloride capturing reaction is as follows:

$$xPPy + xCl^- \leftrightarrow x[PPy^+Cl^-] + xe^-$$

The system is well-operated under 1 V of cell voltage for 200 cycles, and Li^+ was recovered from the natural brine solution (Salar de Olaroz) and the Faradaic efficiency was around 50%. The specific energy consumption was 5 Wh mol^{-1} (Recovery solution: 25 mM LiCl) and 9.4 Wh mol^{-1} (Recovery solution: brine). Although the Li^+ concentration is considerably high (180 mM), the Faradaic efficiency is relatively low and the energy consumption is relatively high. This is because the LMO/PPy battery cell was operated under a high current (~10 C). For a fair comparison with other ELR systems, this cell should be operated under a lower current (~1 C). They also compared the suitability of PPy, carbon felt, and Pt as the counter electrode. Because the PPy electrode showed few variations in electric potential, the ELR system with the PPy counter electrode had the lowest energy consumption compared to other

electrodes. They concluded that PPy is the most suitable alternative to the silver electrode.

A NiHCF is a Prussian blue analogue material that selectively intercalates K^+ and Na^+. The reversible K^+ and Na^+ capturing reaction is as follows:

$$xK[NiFe(CN)_6] + xMCl + xe^- \leftrightarrow xMK[NiFe(CN)_6] + xCl^-$$

Because the affinity of the NiHCF electrode for Li^+ is low, it can be used as the counter electrode of the ELR system. Trócoli et al. suggested the λ-MnO_2/NiHCF ELR system (Trócoli et al. 2015, 2017). Similar to the λ-MnO_2/Ag system, the λ-MnO_2/NiHCF system showed high selectivity towards Li^+ (1.63, 57.6, and 1633 to K^+, Na^+, and Mg^{2+}, respectively) and relatively low energy consumption (3.6 Wh mol^{-1}). The recovery solution, however, produced by using this system contained a high concentration of K^+ and Li^+ purity is low (70 to 80%). An additional separation process could be required for highly pure lithium products.

Kim et al. proposed zinc as a counter electrode in the ELR system due to its low cost, high stability, and large capacity (Kim et al. 2018b). The ELR cell was divided equally into two compartments with an anion exchange membrane placed between the compartments. The λ-MnO_2 and zinc foil electrodes were placed in each compartment and used as positive and negative electrodes, respectively. When lithium recovery occurs at the λ-MnO_2 electrode, the zinc

electrode was oxidized and converted into zinc ions, which attracted chloride ions of the λ-MnO_2 compartment by the charge compensation. This reaction is the reversible reaction. Zinc, thus, can be used as a negative electrode for the ELR system. The overall reaction is as follows:

$$2\lambda - MnO_2 + xLi^+ + xZn(s) \leftrightarrow Li_xMn_2O_4 + xZn^{2+} + xe^-$$

The specific energy consumption for the lithium recovery from simulated Atacama brine was 6.3 Wh mol^{-1} and the capacity retention was 73% after 100 cycles (1 mA cm^{-2}). This study showed the possibility of using metal electrode usage in the ELR system.

Zhao et al. reported the $Li_xMn_2O_4$/PANI cell for lithium extraction from the simulated Taijinair lake brine (Zhao et al. 2019). The PANI electrode reversibly reacts with chloride ions on the principle of p-doping/de-doping. This reversible reaction is as follows:

$$xPANI + xCl^- \leftrightarrow xPANI^+Cl^- + xe^-$$

The PANI is an affordable and eco-friendly polymer material. Thus, it is suitable as a silver electrode alternative. The $Li_xMn_2O_4$/PANI system shows high current efficiency (95%) with good cyclability (70.8% after 200 cycles). The energy consumption during the process was 3.95 Wh mol^{-1} on average. They insisted that this system showed relatively good performance compared to other ELR systems using the silver alternative electrodes. This result should

be further verified because the specific energy consumption considerably increased with the number of cycles (3.13 Wh mol^{-1} at the first cycle and 5.08 Wh mol^{-1} at the fourth cycle).

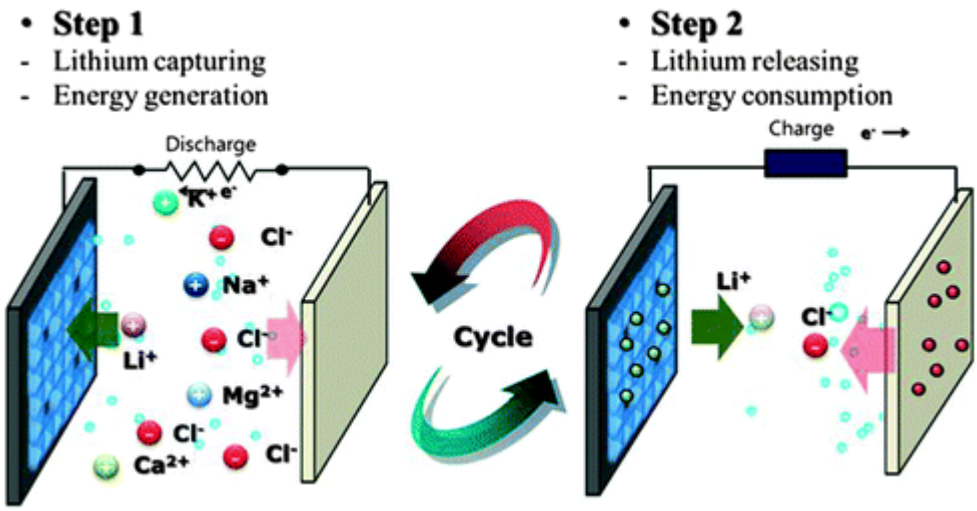

Figure 2-4 Schematic of the lithium ion capturing process in source water (1st step, discharging process) and the lithium ion releasing process in reservoir solution (2nd step, charging process) (Lee et al. 2013)

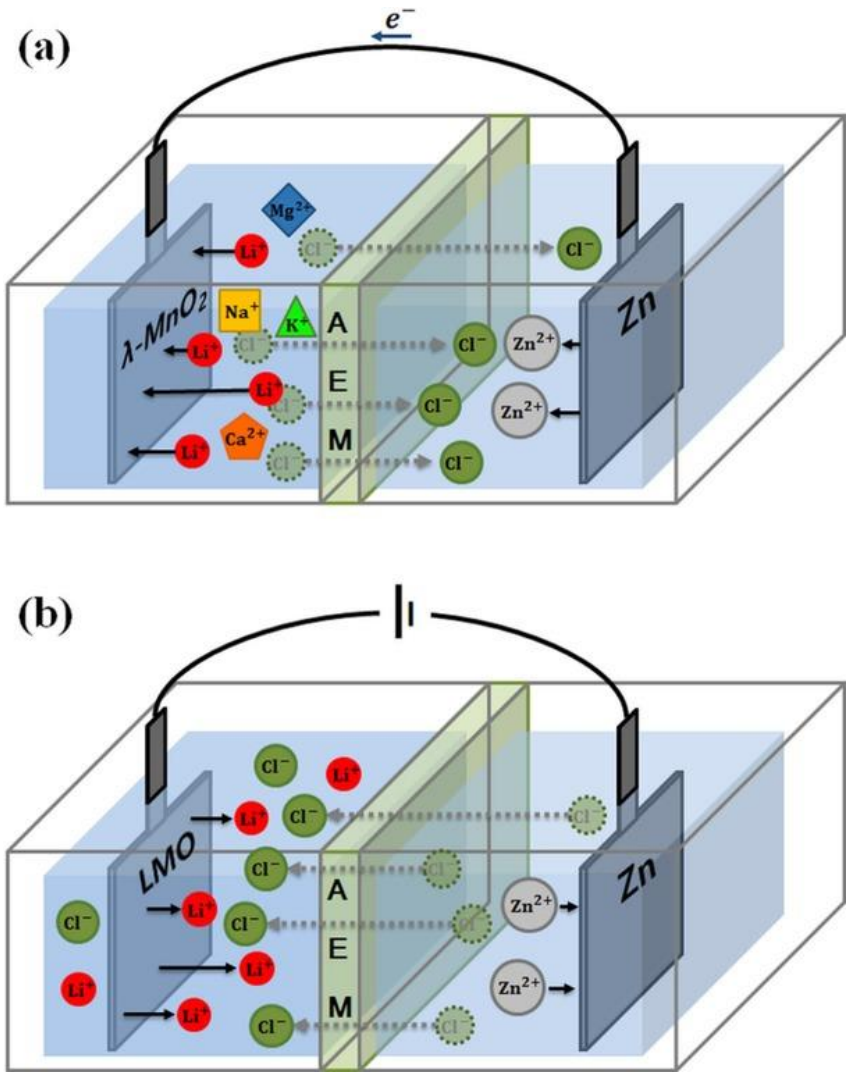

Figure 2-5 Diagrams of the electrochemical lithium recovery process with the LMO-Zn system. (a) Discharging step: lithium ions are selectively captured from the brine water, and zinc oxidation occurs. (b) Charging step: lithium ions are released into the charging solution, and zinc reduction occurs (Kim et al. 2018b).

2.3.3 Hybrid supercapacitor system

A hybrid supercapacitor system was also suggested by Kim et al. (Kim et al. 2015b). In this system, an activated carbon (AC) electrode is used instead of the silver electrode, because of the economic feasibility and system stability. A reversible counter reaction occurred when the AC electrode adsorbed and desorbed the dissolved ions like an electric double-layer capacitor. An anion exchange membrane was placed in front of the AC electrode to prevent the cation adsorption into the electrode. The flow-type reactor was designed to make it easier for the actual chemical processes. The capacity retention was 97% until the 50th cycle of the process with almost 100% coulombic efficiency. The cycling performance that represents the λ-MnO_2/AC hybrid supercapacitor system had excellent long-term stability.

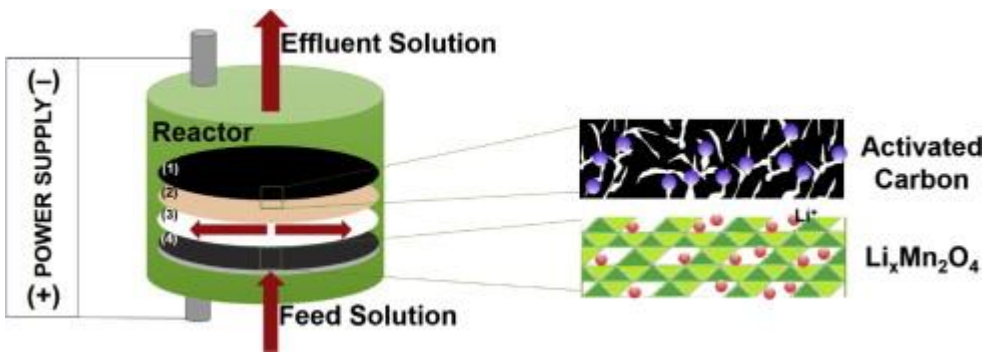

Figure 2-6 Schematic diagram of the continuous lithium recovery system. (1) An activated carbon composite electrode, (2) an anion exchange membrane, (3) nylon as a spacer and (4) a λ-MnO_2 composite electrode are contained in the reactor (Kim et al. 2015b).

2.3.4 Symmetric rocking chair battery-liked system

A symmetric rocking chair battery-like system is a system using $LiMn_2O_4$ as a positive electrode and $Li_{1-x}Mn_2O_4$ as a negative electrode. Two LMO electrodes are capturing and releasing Li^+ simultaneously in the continuous lithium extraction process. Zhao et al. firstly proposed a symmetric rocking chair ELR system using two LMO electrodes (Zhao et al. 2017). In this research, the effects of the potential and temperature on the performance factors (extraction capacity, separation coefficient, current efficiency, and specific energy consumption) were investigated and the optimized conditions (0.6 V, 25 ^oC) were presented according to comprehensive evaluations. Furthermore, the effect of coexisting ions on the recovery performance was evaluated ($Mg^{2+}>Na^+>Ca^{2+}>K^+$), which was explained by the difference in ionic radii and ionic valence. The specific energy consumption of this system was relatively high (16-19 Wh mol^{-1}) since this system operated under the constant-voltage mode (Qu et al. 2016). In the follow-up studies, a rocking chair battery-like system using $LiMn_2O_4$ has been operated under the constant-current mode, and the specific energy consumption is much lower (under 3 Wh mol^{-1}) (Joo et al. 2020a; Romero et al. 2020).

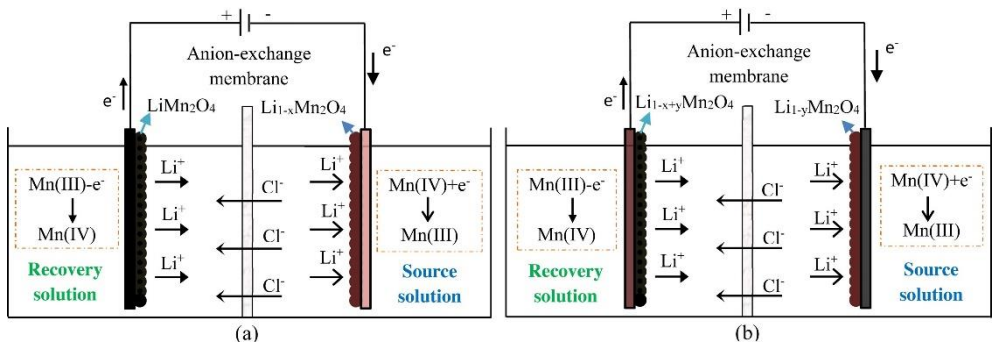

Figure 2-7 Schematic of (a) 1 st step and (b) 2nd step of the $LiMn_2O_4/Li_{1-x}Mn_2O_4$ by electrochemical method (Zhao et al. 2017)

2.3.5 Flow-through type reactor

The Li^+ concentration of the brine source is relatively lower than that of the battery electrolyte, therefore, the concentration polarization is influential to the recovery performance. A flow-through type reactor is one of the solutions for minimizing the negative effect of the concentration polarization. Palagonia et al. operated the flow-through type reactor and analyzed the concentration polarization (Palagonia et al. 2017). The authors compared the lithium recovery performance (specific capacity and rate capability) with and without flow rate and proved that convection mass transport minimized the negative effect of concentration polarization. When the brine from Salar de Atacama was used as a lithium source, the specific capacity with the flow was 5 times higher than without flow. In their follow-up parameter study, the effect of the current density and mass loading on the recovery performance was also examined (Palagonia et al. 2019) by using the optimized flow-through reactor and obtained the 100 mM LiCl recovery solution (purity: 94%) from the 1 mM LiCl+100 mM NaCl source water. By evaluating the economic feasibility of the process with the pumping energy, it was calculated to be commercially valuable when the source water contained more than 1 mM of Li^+. It is verified that the flow-through type reactor is an efficient recovery method even for the

low Li^+ concentration brine. Subsequent studies should focus on controlling the convection mass transport to further improve performance.

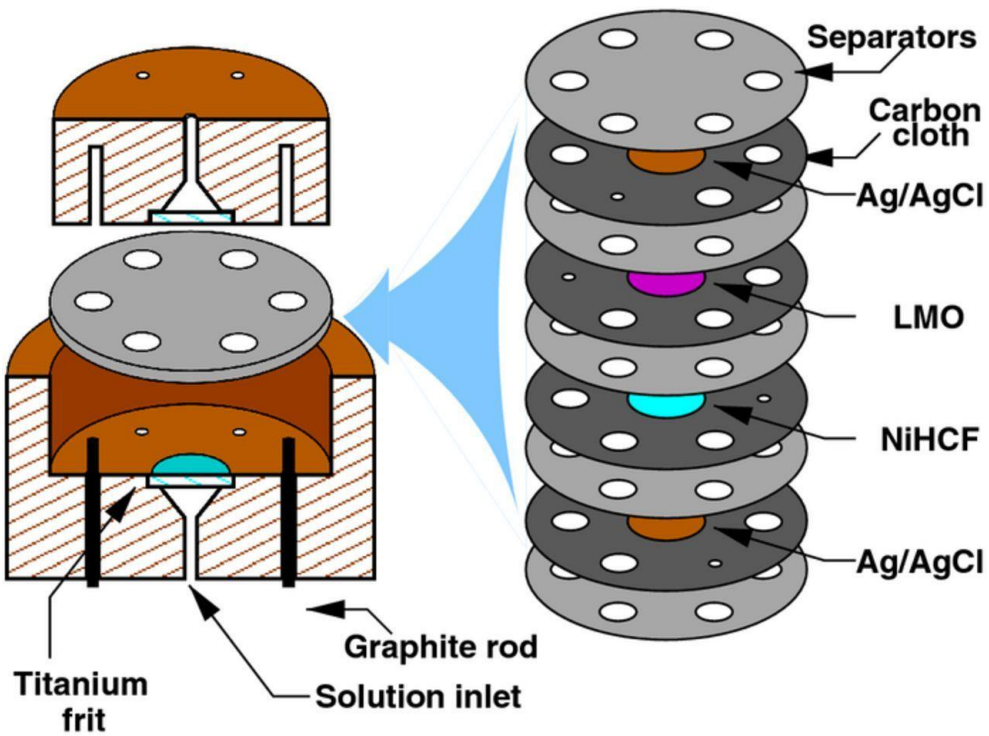

Figure 2-8 Representation of the cell (vertical section) on the left. The gray disk represents the electrode. On the right, the arrangement of the electrodes, one in top of the other, separated by a filter paper of the same size (Palagonia et al. 2017)

2.4. LMO electrode modification to enhance the Li^+ recovery performance

The most widely used methods for LMO synthesis are the solid-phase combustion method and the hydrothermal method, which are simple and economical (Xiao et al. 2013; Xu et al. 2016). The pristine LMO fabricated by these methods has high selectivity to Li^+, but its rate capability, long-term stability, and energy efficiency need to be improved. For this, strategies to refine the LMO electrodes have been proposed.

The first strategy is a polymer film coating to prevent capacity loss and improve capacity. Du et al. fabricated the λ-MnO_2/PPy/PSS electrode (Du et al. 2016). The λ-MnO_2 nanorod electrode was fabricated by hydrothermal synthesis, and polypyrrole (PPy) and polystyrene sulfonate (PSS) films were covered by the unipolar pulse electrodeposition (UPED). PSS-doped PPy acted as a cation exchanger, allowing λ-MnO_2/PPy/PSS electrodes to have higher Li^+ selectivity than the pristine λ-MnO_2 electrode. A high lithium recovery capacity of 35.2 mg g^{-1} was shown using this electrode, which is near the theoretical value (38.3 mg g^{-1}). Assuming the Faradaic efficiency is 100%, the capacity of the LMO electrode is 135 mAh g^{-1}, which is the highest value among the ELR studies. The authors elucidate that the nanorod morphology provided a high surface area with the enhancement of the ionic conductivity of the electrode

structure by a polymer film. Further verification, however, is needed because the operating voltage range is slightly out of the potential window where the redox reaction of LMO occurs (Battistel et al. 2020). LMO covered by a three-dimensional nanostructured hybrid inorganic-gel framework is developed as an electrode for electrochemical lithium extraction (Zhao et al. 2020b). PPy and Al_2O_3 are used as the framework to prevent capacity loss caused by the dissolution of manganese. The synthesis process is as follows. First, the LMO was fabricated by the solid combustion method. Then, Al_2O_3 was coated on the LMO particle by using the sol-gel method. Last, PPy was coated on the Al_2O_3/LMO by the oxidative polymerization and PPy/Al_2O_3/LMO was fabricated. The PPy/Al_2O_3/LMO electrode showed enhanced cyclability (91.66% after 30 cycles at the 1C rate) compared to the pristine LMO electrode (77.70% in the same condition). The lithium recovery performance of the continuous hybrid capacitor system using this electrode showed a high purity of the product (97.37%, the highest value among the ELR studies) with efficient energy consumption (1.41 Wh mol^{-1}).

Another strategy is to modify the physical properties of the LMO electrode. A self-supported λ-MnO_2 film electrode was developed for the ELR system by Xu et al. (Xu et al. 2018). MnO_2 film on the platinum plate was fabricated by the cathodic deposition, which is followed by the aerobic

oxidation and lithiation step (hydrothermal method). Because this electrode was fabricated without any binder material, the electrode had high electrical conductivity and high ion transfer efficiency. The ELR system using this electrode showed higher rate capability (100 mAh g^{-1} at the current density of 50 mA g^{-1} in 30 mM Li^+ aqueous solution) and better long-term cyclability (91% of the capacity remained after 100 cycles) than the λ-MnO_2 powder electrode (80 mAh g^{-1} of capacity and 76% of the capacity remained at the same conditions). Xie et al. have reported a $LiMn_2O_4$ nanorod electrode applied to the ELR system. $LiMn_2O_4$ nanorod was fabricated by a continuous process of the hydrothermal method, grounding, and sintering (Xie et al. 2020). The average diameter and length of the nanorod are 500 nm and 4-7 μm, respectively (the pristine LMO is micron-sized and spherical-like). Because of the large surface area of the nano-sized electrode, the charge transport reaction at the LMO electrode accelerated and Li^+ was selectively recovered in a highly energy-efficient way (1.76 Wh mol^{-1}). The limited cycling performance of the electrode (37.4% of the capacity retention after 200 cycles) is required to be improved for practical application.

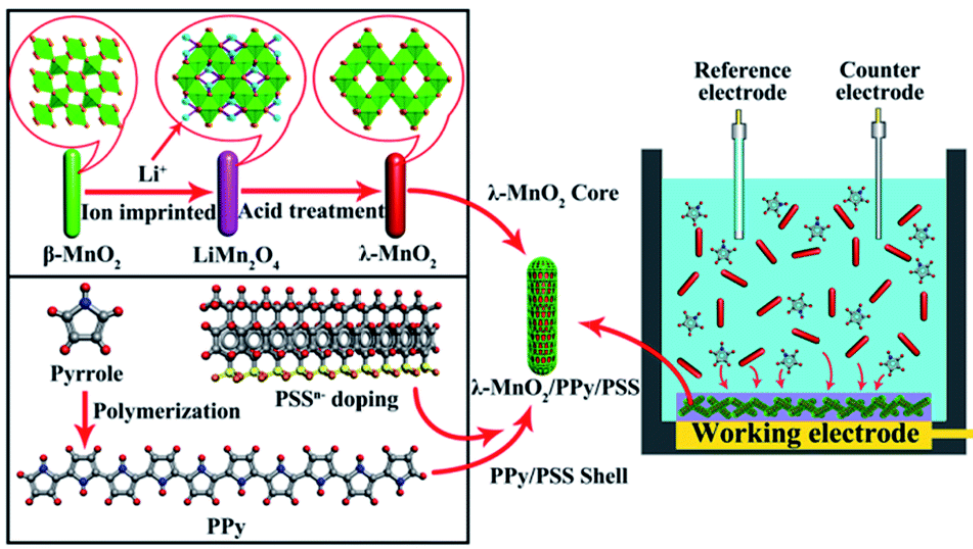

Figure 2-9 Schematic of the formation of the λ-MnO2/PPy/PSS core–shell nanorod film on an electrode (Du et al. 2016)

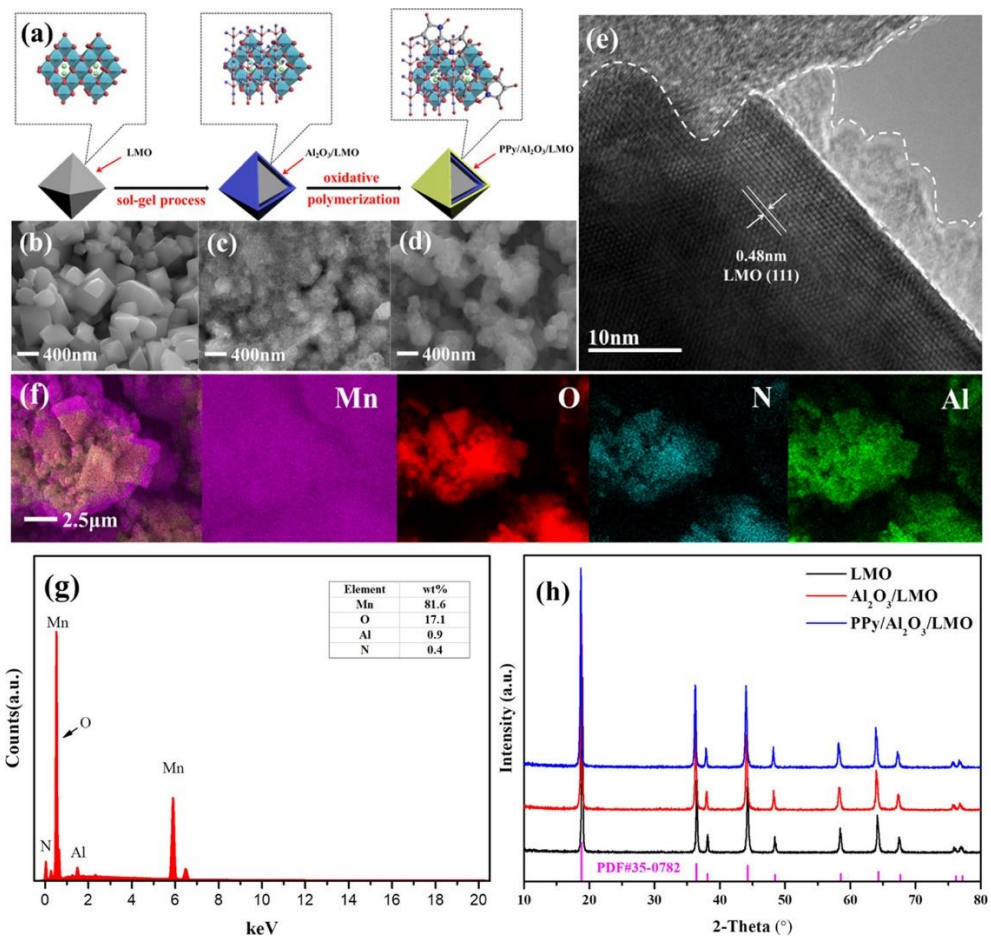

Figure 2-10 (a) Schematic diagram of material synthesis; SEM images of (b) LMO, (c) Al_2O_3/LMO, and (d) PPy/Al_2O_3/LMO samples; (e) high-resolution TEM images of surface-treated PPy/Al_2O_3/LMO particles; (f) EDS mapping and (g) spectroscopy of PPy/Al_2O_3/LMO; (h) XRD patterns of LMO, Al_2O_3/LMO, and PPy/Al_2O_3/LMO (Zhao et al. 2020b).

2.5. System analysis

Understanding the mechanism and behavior of the ELR system is important for further development. Some research utilizing electroanalysis, X-ray measurement, and numerical simulation has been reported. In recent years, selective concentration polarization was analyzed.

2.5.1 Electroanalysis

Marchini et al. have studied surface chemistry and ion exchange behavior of the LMO electrode through electroanalysis (Marchini et al. 2016). The cyclic voltammetry (CV) and galvanostatic intermittent titration technique (GITT) measurements were used to show how the Li^+ was stably and reversibly intercalated/de-intercalated in the natural brine (Salar de Olaroz). The diffusivity of Li^+ in the nanocrystalline structure was measured as 10^{-10} cm^2 s^{-1} using the chronoamperometry method. The ratio of Mn/O at the surface and initial Mn^{IV}/Mn^{III} of the crystal was measured as 1:2 and 1:1, respectively, by photoelectron spectroscopy. The content of Mn^{III} was depleted when the potential exceeds 1.1 V (vs. Ag/AgCl) and dominant when the potential is less than 0.4 V (vs. Ag/AgCl). The same research group investigated LMO surface composition and crystal structure affected by the electrode potential in the brine

(Marchini et al. 2018a). They found that the intercalation/de-intercalation reactions of the LMO consist of 2 steps involving two cubic phase transitions in an aqueous brine solution resembling the behavior in organic electrolytes. They found that the oxide surface of LMO adsorbed the sodium ion, but the intercalation of sodium ion into the crystal structure did not occur. They also analyzed the interface of LMO in the LiCl and natural brine solution by using electrochemical impedance spectroscopy (EIS) with a modified Randles equivalent electrical circuit model (Marchini et al. 2018b). Unlike with the organic solvent, a solid-electrolyte interface (SEI) was not created on the LMO electrode in the aqueous brine solution, which results in a single semicircle in the Nyquist plot. It was also found that the R_{ct} value was at the minimum for a specific state-of-charge value (0.25 and 0.75) when the intercalation site was half-filled with Li^+ at each phase. The overall behavior of Li^+ intercalation in aqueous brine solution was precisely analyzed by this research group. By using this result, the operation condition for efficient lithium recovery can be provided with analytical evidence.

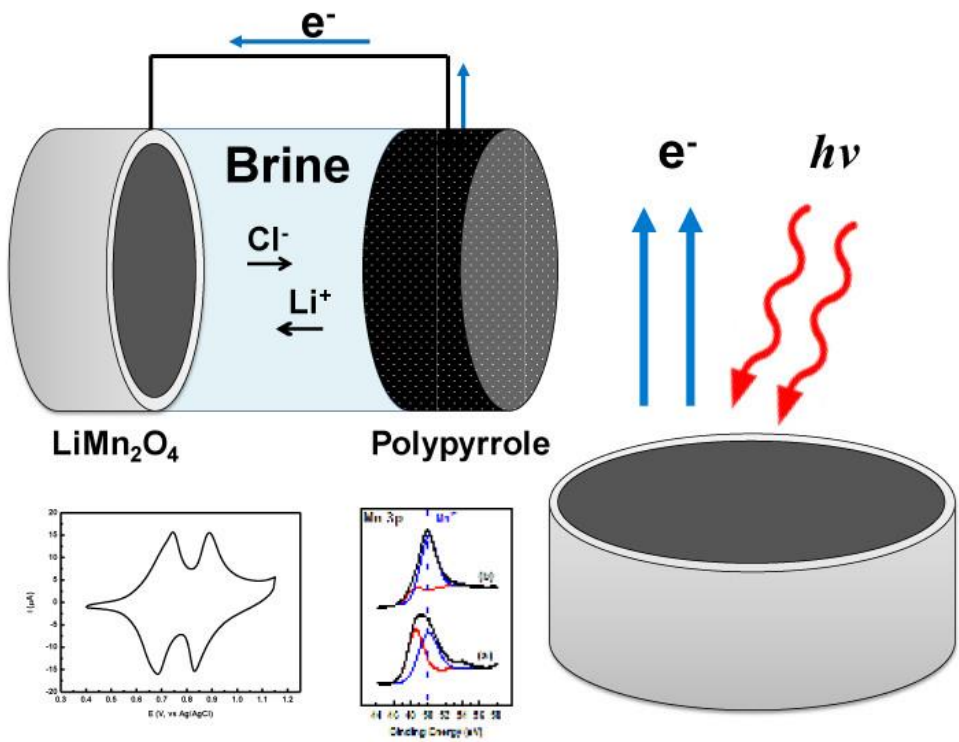

Figure 2-11 Schematic diagram of $LiMn_2O_4$/PPy system and surface chemistry analysis (Marchini et al. 2016)

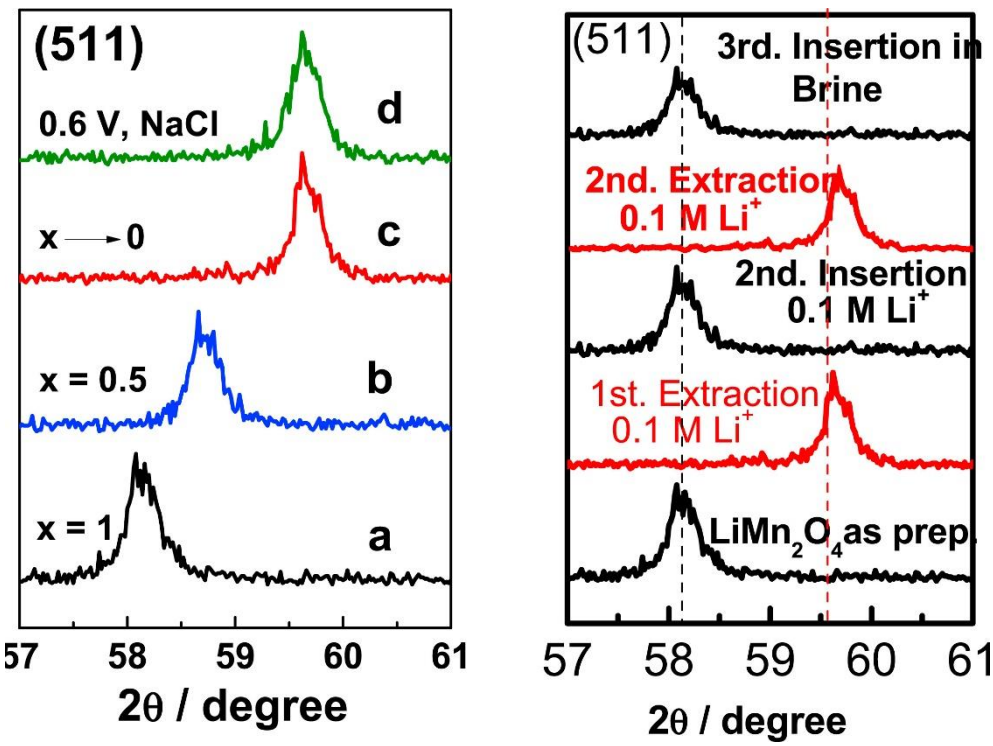

Figure 2-12 X-ray diffraction patterns of a stainless steel electrode cast with the $Li_xMn_2O_4$ slurry in the 2θ region from 57° to 61° (Cu-Kα), where (511) peak appears. Peaks indicated as (a), (b) and (c) correspond to different states of charge represented with the x value and reached after 1 h polarization at different potentials: 0.6 V for peak (a), 0.85 V for peak (b) and 1.1 V for peak (c), in LiCl 0.1 M. Peak (d) corresponds to the resulting pattern after 1 h polarization of the delithiated structure of peak (c) at 0.6 V in 0.1 M NaCl. Right top: Lithium insertion from natural brine (Marchini et al. 2018a).

2.5.2 Numerical simulation

Romero et al. numerically simulated the LMO/PPy and LMO/AC systems in the one-dimensional domain using COMSOL Multiphysics software (Romero et al. 2018). This is the first study that analyzed the ELR system behavior by using computational modeling and simulation. The model was constructed based on the pseudo-2D model (P2D) widely used in lithium-ion battery research. The concentration profiles of Li^+, Na^+, K^+, Mg^{2+}, $B_2O_7^{2-}$, cell voltage and electrolyte potential with the constant-current operation were calculated. Besides, Romero et al. tested and numerically simulated a 3D packed bed reactor consisting of a porous petroleum coke electrode covered with $LiMn_2O_4$ (Romero et al. 2020). They found that the degree of de-lithiation of the $Li_{1-x}Mn_2O_4$ electrode determines the amount of recovered Li^+. The effect of flow rate on the electrolyte concentration distribution was also investigated and it was concluded that a specific value of flow rate is needed for the uniform concentration distribution in the flow channel. The authors proposed a direction of designing the scaled-up ELR system such as increasing the volume fraction of LMO and decreasing electrode particle size and contact resistance between electrode particles.

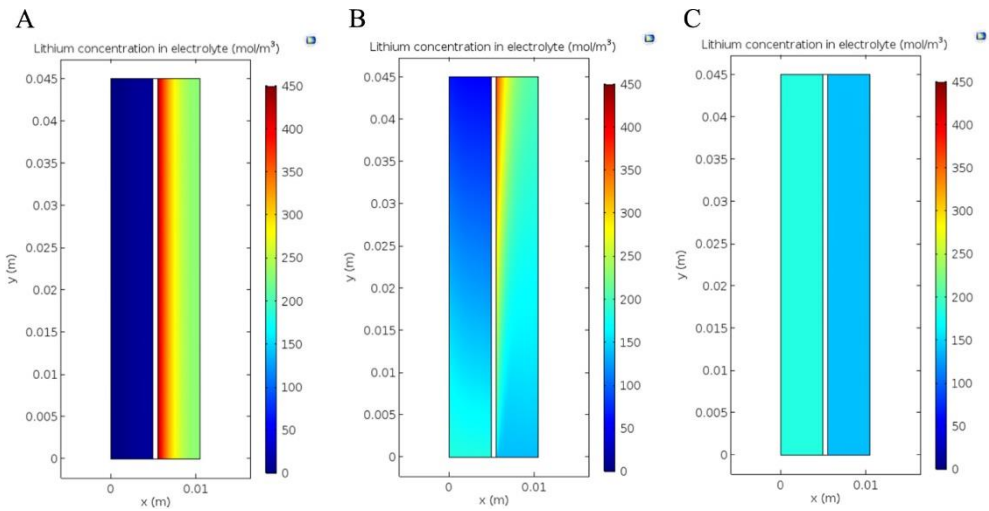

Figure 2-13 2D lithium concentration profiles simulated at different flow rate values uy: 0 (A), 10^{-5} (B) and 0.012 $m \cdot s^{-1}$ (C) at 100 mA and ε_{LMO} = 0.0077 after 3865 s (1.11 h) or final time of electrolysis (Romero et al. 2020).

2.5.3 X-ray measurement

Kim et al. analyzed the physicochemical behavior of the LMO electrode at various concentrations and current density conditions (Kim et al. 2020). From the X-ray absorption near edge structure (XANES) and extended X-ray absorption fine structure (EXAFS) spectra, the structural transition of the LMO electrode after the recovery process was investigated. The λ-MnO_2 electrode was found to have three chemical states during the recovery process: depletion, transition, and saturated regions. The authors presented that the depletion state is dominant when the concentration of Li^+ is low or the current density is high. To reduce this negative effect, they suggested the ball-milling method for decreasing the particle size of LMO and improving the capacity of the system. This result justified why small-sized electrode particles are essential for the high-performance ELR system.

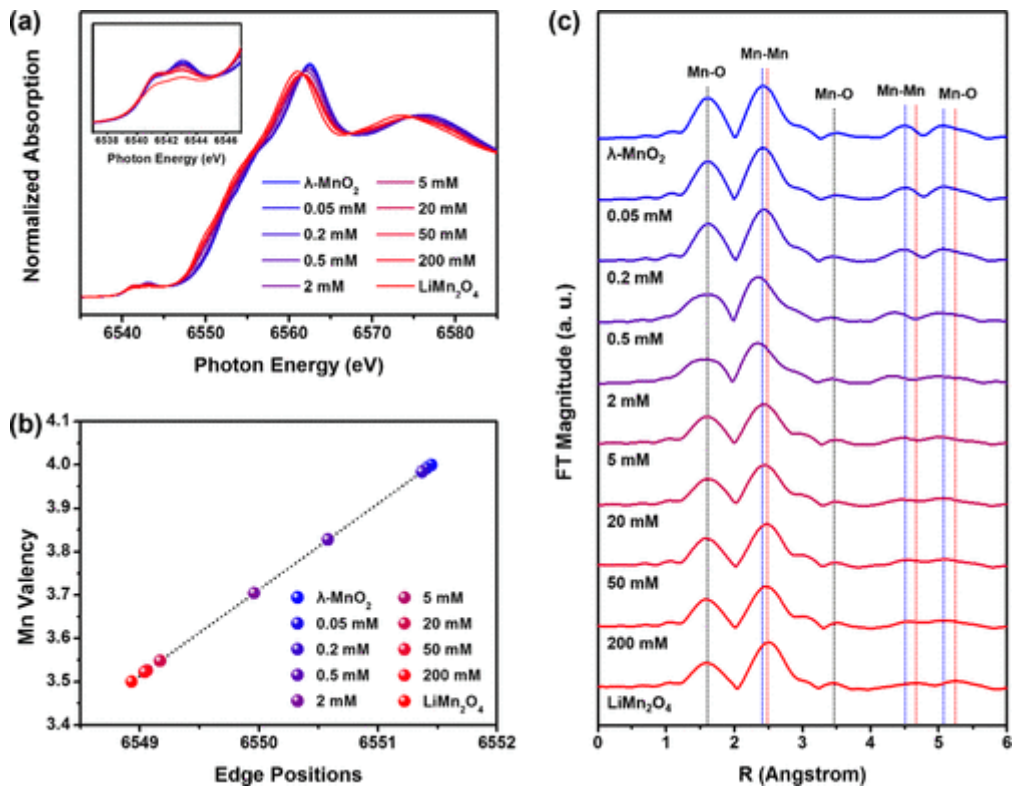

Figure 2-14 (a) Mn K-edge XANES spectra of λ-MnO_2 electrodes after lithium recovery from source waters with diverse Li^+ concentrations at 25 mA/g. The inset shows the enlarged prepeaks. (b) Oxidation state of Mn calculated from the edge positions of the XANES spectra displayed in (a). (c) k^3-weighted Fourier transform of the EXAFS spectra at Mn K-edge of λ-MnO2 electrodes after the operation in source waters with various Li^+ contents. XANES and EXAFS spectra of λ-MnO_2 and $LiMn_2O_4$ were added for comparisons (Kim et al. 2020).

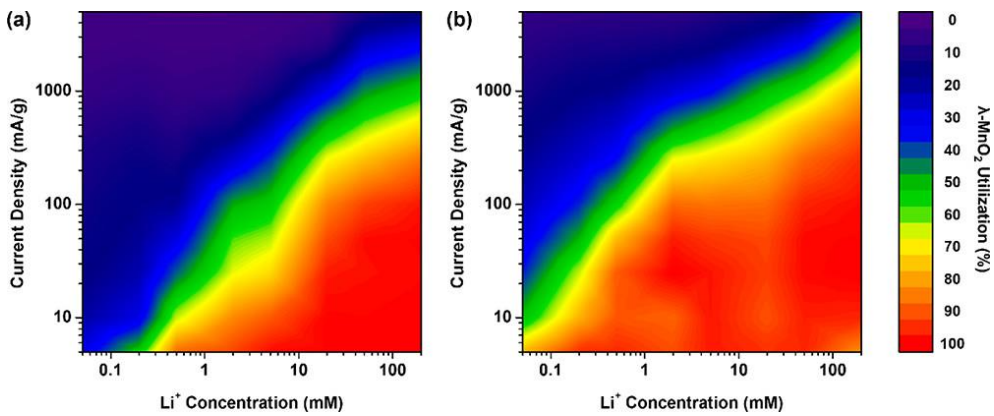

Figure 2-15 Contour diagrams showing utilization rate of λ-MnO_2 in electrochemical lithium recovery by using (a) pristine and (b) ball-milled particles at diverse operation current densities and Li^+ concentration (Kim et al. 2020).

2.5.4 Selective concentration polarization

The negative effect of the concentration polarization on the system performance was analyzed by Guo et al (Guo et al. 2020). Contrary to the lithium-ion battery, the electrolyte of the ELR system contains a low concentration of Li^+ and a high concentration of coexisting ions like Na^+ and Mg^{2+} (Zhao et al. 2013; Pramanik et al. 2020). Therefore, the LMO electrode of the ELR system is vulnerable to concentration polarization and exhibits low-rate capability and high energy consumption. They named this unique phenomenon found only in the ELR system as selective concentration polarization (SCP), which is caused by the depletion of Li^+ and the accumulation of coexisting ions in the boundary layer. Mg^{2+} is an ion that strongly induces SCP more than other cations whose strength of SCP is followed by Na^+, Ca^{2+}, and K^+, in that order. They also proved that stirring can reduce the negative effect of SCP in the experiment. This study identified the reason for the performance degradation in the ELR system, which is distinguished from the battery system. This suggests the development direction of a flow-type ELR system which has been studied recently.

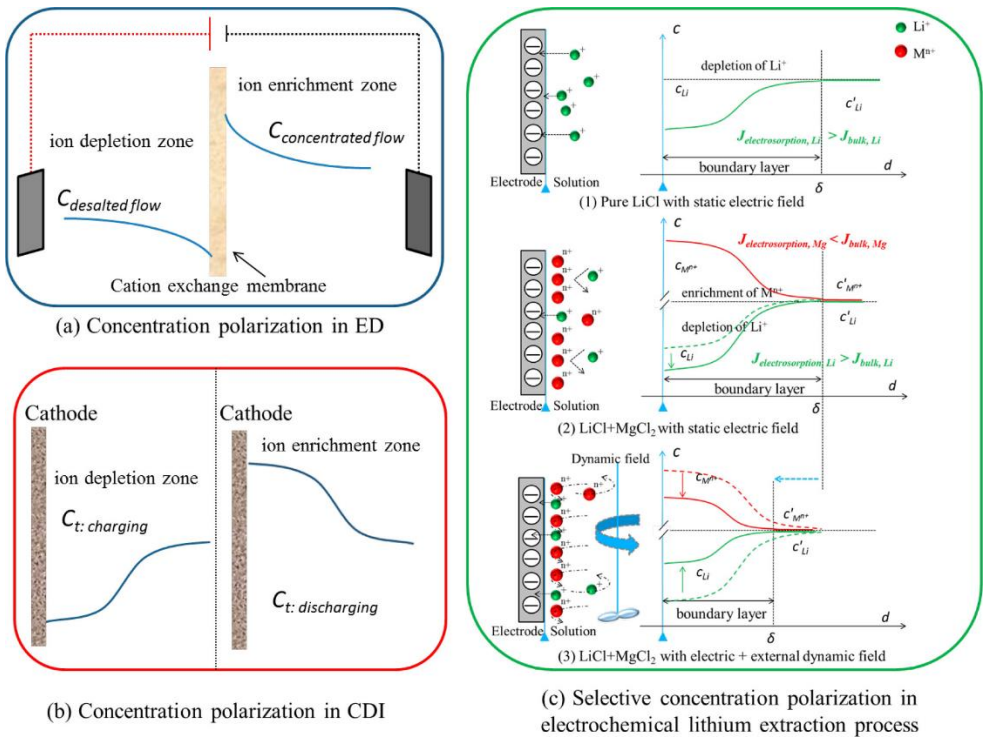

Figure 2-16 Schematic diagrams of concentration polarization in (a) ED and (b) CDI and (c) selective concentration polarization in the electrochemical lithium extraction process (Guo et al. 2020a).

2.6. Application

Lithium can be recovered from various sources, such as wastewater and desalination brine. For this, it is necessary to design the ELR systems considering the special characteristic of the source water.

2.6.1 Lithium recovery with the wastewater treatment

Kim et al. suggested the λ-MnO_2/BDD bi-functional system to recover Li^+ from the wastewater discharged from the actual battery recycling plant (Kim et al. 2018a). The wastewater contained a relatively high concentration of Li^+ (270 mM) but also contained lots of organic pollutants that should be treated. To decompose dissolved organics, a boron-doped diamond (BDD) electrode was adopted as an oxidant-generating electrode (counter). Using the system, a high purity recovery solution (98.6 mol% of Li^+) was produced and DOC (dissolved organic carbon) of the wastewater was reduced to 65%. This study is meaningful in that the range of electrolytes that can be applied to the ELR system has been increased through the development of a bi-functional cell system.

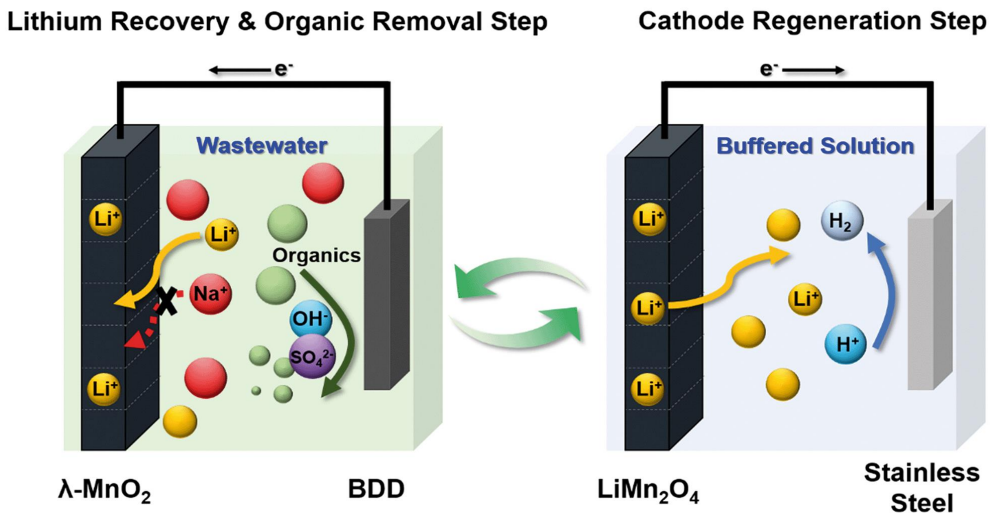

Figure 2-17 Schematic of the electrochemical system for simultaneous lithium recovery and organic pollutant removal (Kim et al. 2018a).

2.6.2 Lithium recovery from the desalination concentrate

A λ-MnO_2/Ag system that recovers lithium from the desalination brine was developed and evaluated by Kim et al. (Kim et al. 2019). The desalination brine contained extremely low concentrations of Li^+ (0.063 mM), which makes it impossible to manufacture the product with high Li^+ concentration and purity through a one-stage ELR system. Accordingly, the research team invented a two-consecutive recovery process that recovers Li^+ once again from the Li^+ recovered solution. The two consecutive recovery processes produced a recovery solution with high purity (up to 99.0%) and high Li^+ concentration (190 mM). The authors compared the lithium recovery performance of the adsorption and ELR process and confirmed that the ELR system is much faster at capturing and releasing steps.

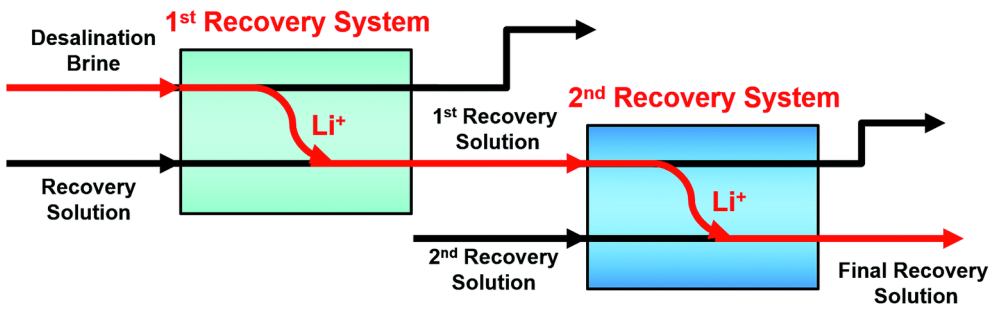

Figure 2-18 Schematic illustration of the consecutive process for lithium recovery from desalination brine (Kim et al. 2019).

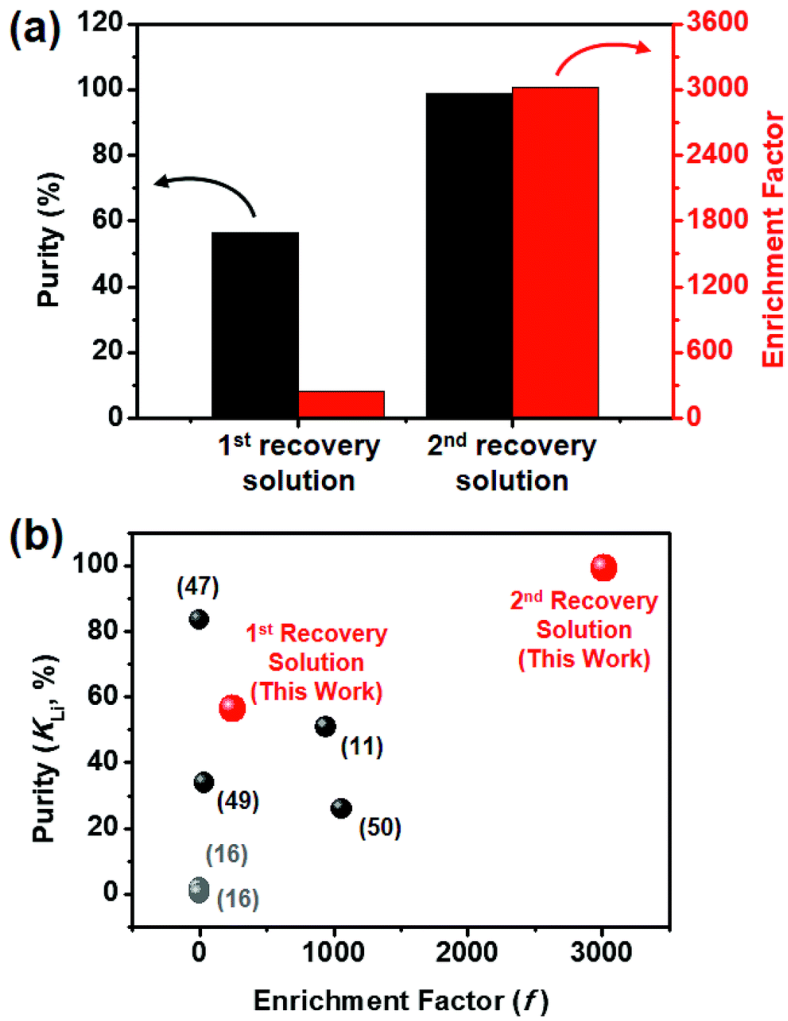

Figure 2-19 (a) Purity (K_{Li}) and enrichment factor (f) of the desalination brine, 1st recovery solution, and 2nd recovery solution of the consecutive lithium recovery process. (b) Comparisons of the K_{Li} and f with those from previous reports on adsorption and electrodialysis processes for recovering lithium from seawater or desalination brine (black balls: adsorption process; grey: electrodialysis process, and red: this study) (Kim et al. 2019).

2.7. Summary of the system performance and perspectives

ELR systems using LMO electrodes have been intensively studied since 2013. The research trend in this field is gradually shifting from quantitative research to qualitative research. In other words, improving the performance of the ELR system is a major concern in the present and the future. In this section, the system performance of the literature is summarized (as shown in **Table 2-1**) and the perspectives are presented.

Table 2-1 Performance of the ELR system using LMO electrode

LMO	Mass loading (mg cm^{-2})	Electrode dimension (cm×cm or cm^2)	Counter	Solution composition	Operation mode	Capacity (mAh g_{LMO}^{-1})	Energy consumption (Wh mol_{Li}^{-1})	Ref.
λ-MnO_2	-	1.0×1.0	Pt	Geothermal (Li^+: 0.74 mM)	Forward sweep	85	-	(Kanoh et al. 1993)
λ-MnO_2	-	3.0×3.0	Ag	Simulated brine: Salar de Atacama (Li^+: 210 mM)	CC mode (0.5 mA cm^{-2})	-	1.0	(Lee et al. 2013)
λ-MnO_2	-	-	AC	30 mM LiCl, NaCl, KCl, $MgCl_2$, and $CaCl_2$	CC mode (0.5 mA cm^{-2})	-	4.2	(Kim et al. 2015b)
λ-MnO_2	0.52	Plane: 3.0×2.0 Total: 56.0 cm^2	PPy	Brine (Salar de Olaroz) (Li^+: 180 mM)	CC mode (2.5 mA cm^{-2})	-	9.4	(Missoni et al. 2016)
λ-MnO_2 /PPy/PSS	-	5×5 (porous)	Pt	30 mM LiCl and NaCl	CV mode	135	-	(Du et al. 2016)
LMO	-	2 cm^2	NiHCF	Simulated brine: Salar de Atacama (Li^+: 42 mM)	CC mode (1 C)	100	3.6	(Trócoli et al. 2017)
$LiMn_2O_4$	-	3.5×3.0	$Li_{1-x}Mn_2O_4$	Simulated brine (Li^+: 21 mM) and concentrated seawater (Li^+: 32 mM)	CV mode (0.6 V)	77-97	17.89-18.67	(Zhao et al. 2017)

λ-MnO_2	28.6	8.75 cm^2	BDD	Wastewater: battery recycling plant (Li^+: 276.5 mM)	CC mode (2.9 mA cm^{-2})	88	8.71	(Kim et al. 2018a)
$LiMn_2O_4$	-	2.5×4.0	Zn	Simulated brine: Salar de Atacama (Li^+: 210 mM)	CC mode (0.5 mA cm^{-2})	-	6.3	(Kim et al. 2018b)
Self-supported λ-MnO_2	-	3.0×3.0	Ag	30 mM LiCl, NaCl, KCl, $MgCl_2$, and $CaCl_2$	CC mode (50 mA g^{-1})	100	4.14	(Xu et al. 2018)
$LiMn_2O_4$	25-35	2.0×2.0	PANI	Simulated brine: Taijinair (Li^+: 64 mM)	CC mode (0.5 mA cm^{-2})	~90	3.95	(Zhao et al. 2019)
$LiMn_2O_4$ nanorod	5	-	NiHCF	Simulated brine: Taijinair (Li^+: 31.7 mM)	CC mode (1 C)	105	1.76	(Xie et al. 2020)
λ-MnO_2	-	Diameter: 5 cm	Ag	Desalination brine (Li^+: 0.063 mM)	CC mode (0.01 mA cm^{-2})	-	17.2 (1^{st} step)	(Kim et al. 2019)
λ-MnO_2	5	2.0×2.0	$LiMn_2O_4$	30 mM LiCl	CC mode (0.0625 mA cm^{-2})	128	0.56	(Joo et al. 2020a)
PPy/Al_2O_3/LMO	-	1 cm^2	AC	Simulated diluted brine (Li^+: 23.48 mM)	CC mode (0.75 mA)	~50	1.41	(Zhao et al. 2020b)
$Li_{1-x}Mn_2O_4$	0.76	15.5×4.5 (packed bed)	$LiMn_2O_4$	Simulated brine: Hombre Muerto (Li^+: 190 mM)	CC mode (1.43 mA cm^{-2})	~100	2.76	(Romero et al. 2020)

2.7.1 System proposal and operation

In recent years, the number of studies on the flow-type ELR system is increasing. This trend is different from the past when batch-type or semi-batch-type systems were actively investigated. Compared with the batch-type reactor, the flow-type reactors have the advantages of reducing SCP and producing a uniform quality of Li^+ solution. This feature is advantageous for applying the ELR system to practical usage. Future ELR system research is expected to be conducted for the optimization and design of the flow-type system.

To evaluate the newly developed system, it is necessary to compare it with the system that was previously developed. However, it is not possible to directly compare the performance of each system because the current density and electrolyte conditions are different. These parameters have a great effect on performance. Thus, for a fair comparison, a definite standard for the solution composition and operation mode is required to evaluate the system objectively (Hawks et al. 2019).

Most ELR systems were operated under the constant-current (CC) mode and showed energy consumption of less than 10 Wh mol^{-1} as shown in Table 1. This value is lower than the energy consumption of the ELR system operated under constant-voltage (CV) mode (over 10 Wh mol^{-1}). CC mode consumes less energy than CV mode because of lower resistive dissipation in the

operation (Qu et al. 2016). However, CC mode consumes more time than CV mode. Considering the benefits and drawbacks of CC and CV mode, an appropriate combination of operating mode is a promising strategy for rapid and energy-efficient processes.

2.7.2 LMO electrode modification

As mentioned in previous sections, one of the main problems of the LMO is that only the surface of the LMO particle is utilized at the low Li^+ concentration sources, so the total capacity of the LMO is limited. To solve this problem, a small-sized LMO particle to increase the surface-to-volume ratio is required to be developed. Little research has been reported on the ELR system (only nanorod). Therefore, various types of nano sized LMOs need to be investigated to increase the capacity and rate capability of the LMO electrode used in the low Li^+ concentration sources.

Another problem is that the capacity of the LMO decreases with the number of cycles due to the manganese dissolution. To solve this problem, it is necessary to develop a protection method for the electrode particle to prevent manganese dissolution. Only two coating methods (λ-MnO_2/PPy/PSS and PPy/Al_2O_3/LMO) were reported in the previous literature, and these electrodes showed high capacity and cyclability during the process. Various types of coating methods should be examined to increase the stability of the LMO electrode during the long-term process.

2.7.3 System analysis

The behavior of LMO electrodes used in the ELR system is different from the behavior of LMO electrodes used in the battery system. Most of the solutions used for ELR research were electrolytes containing equivalent moles of salt or simulated brine, which normally contains 30-300 mM of Li^+. This value is considerably low compared to lithium-ion battery electrolyte (typically, 1 M) (Ravikumar et al. 2018). Meanwhile, the solutions used for ELR studies contain a lot of impurities such as Mg^{2+}, Na^+, and Ca^{2+}. Recent studies have begun to analyze the behavior of the ELR system such as SCP, and more future research is required to fully understand the special phenomena that occur only in the ELR system, not lithium-ion battery systems.

2.8. Summary

In this section, ELR systems using the LMO electrode are reviewed. The λ-MnO_2/Pt system, λ-MnO_2/Ag battery system, λ-MnO_2/AC hybrid supercapacitor, $LiMn_2O_4$/$Li_{1-x}Mn_2O_4$ rocking chair battery-liked, and the flow-type system were proposed as representative electrode systems. Activated carbon, polypyrrole, nickel hexacyanoferrate, zinc, and polyaniline were suggested as alternatives for the silver electrode. LMO modification research was conducted in addition to developing λ-MnO_2/PPy/PSS, PPy/Al_2O_3/LMO, self-supported λ-MnO_2, and $LiMn_2O_4$ nanorod electrodes. To understand the behavior of the LMO, the surface and crystal of the LMO were analyzed by electrochemical and X-ray measurements. Interest in the hydrodynamics of the ELR system is growing recently, and computational simulation and the concept of concentration polarization have been used to analyze the system with convection mass transport. For a practical demonstration of the process, ELR systems were applied to the wastewater treatment of the battery recycling plant and desalination plant. Because of the high Li^+ selectivity and stability of the LMO electrode, the ELR system can be applied to various lithium resources with a high concentration of impurities such as salt brine, wastewater, geothermal water, desalination brine, and even

seawater. ELR technology will be a promising extraction method in the green energy society of the future.

3. Pilot-scale design and demonstration of an electrochemical system for lithium recovery from the desalination concentrate

3.1. Introduction

Ever since the beginning of human culture, the scarcity of freshwater has been an unresolved problem for a large number of populations (Rock 1998; Hoekstra et al. 2012). Given that 97% of the water on our planet is held by the seas and oceans, seawater desalination is undoubtedly the clearest answer to solve this problem (Corcoran 2010; Elimelech and Phillip 2011; Ghaffour et al. 2013). Therefore, intensive efforts have been made for the removal of salts (typically NaCl) from seawater. Recent advances in desalination technologies have resulted in the production of approximately 97.4 million tons of freshwater daily from seawater (International Desalination Association 2019). In the meantime, seawater desalination also produces large amounts of concentrated brine (i.e., desalination concentrate), which has raised concerns about their adverse impact when discharged, such as the disruption of marine ecosystems (Abu Qdais 2008; Lattemann and Höpner 2008; Missimer and Maliva 2018; Panagopoulos et al. 2019). For this reason, various attempts have been made to treat and utilize desalination concentrate

in an economical and environment-friendly manner. One typical approach is the extraction of valuable resources (Kim 2011; Xu et al. 2013; Morillo et al. 2014; Shahmansouri et al. 2015; Giwa et al. 2017).

Seawater is known to contain huge amounts of lithium (230 billion tons), but lithium ions (Li^+) in seawater are often considered unlikely to be useful owing to their low concentration (e.g., 0.17 mg/L) and low proportion (less than four orders of magnitude compared with sodium). This makes it extremely challenging to separate lithium using conventional technologies based on evaporation or adsorption processes (Chitrakar et al. 2001; Chung et al. 2008; Wang et al. 2009; Hoshino 2013a, b, 2015; Choubey et al. 2017; Yang et al. 2018). An increase in the price of lithium has brought lithium in seawater into the limelight, and recently developed electrochemical lithium recovery systems are regarded as one of the most promising techniques to extract lithium from seawater (Kanoh et al. 1993; Pasta et al. 2012; Marchini et al. 2018c; Kim et al. 2018a; Lawagon et al. 2018; Yoon et al. 2019). Based on a battery-like λ-MnO_2/Ag system with high Li^+ selectivity proposed by our research group, this system is highly feasible when applied to the desalination concentrate containing two to three times higher concentrations of lithium ions than seawater (Lee et al. 2013; Kim et al. 2019). However, few attempts have been made to bring this technology from lab-scale experiments to

industry-level applications.

Herein, a pilot-scale electrochemical lithium recovery system employing λ-MnO_2 and Ag electrodes is reported for the capture and release of lithium and chloride, respectively, from desalination concentrate. Before designing the system, three steps are defined necessarily for the proper and continuous operation of the system: Li^+-capturing step (Step 1), washing step (Step 2), and Li^+-releasing step (Step 3); these are schematically illustrated in **Figure 3-1**. In Step 1, Li^+ in desalination concentrate is captured by discharging the electrochemical cell by applying current, and λ-MnO_2 and Ag are simultaneously converted into $Li_xMn_2O_4$ and $AgCl_x$ ($0 < x < 1$), respectively. In Step 2, electrodes are washed with pure water to remove impurities including ionic species (e.g., Na^+, Mg^{2+}, K^+, and Ca^{2+}) smeared on the electrode surface. In Step 3, Li^+ is released from the electrode to the recovery solution by electrochemically charging the cell. This step not only leads to the production of concentrated Li^+ solutions but also regenerates the electrodes into λ-MnO_2 and Ag, enabling the system to run continuously and repeatedly.

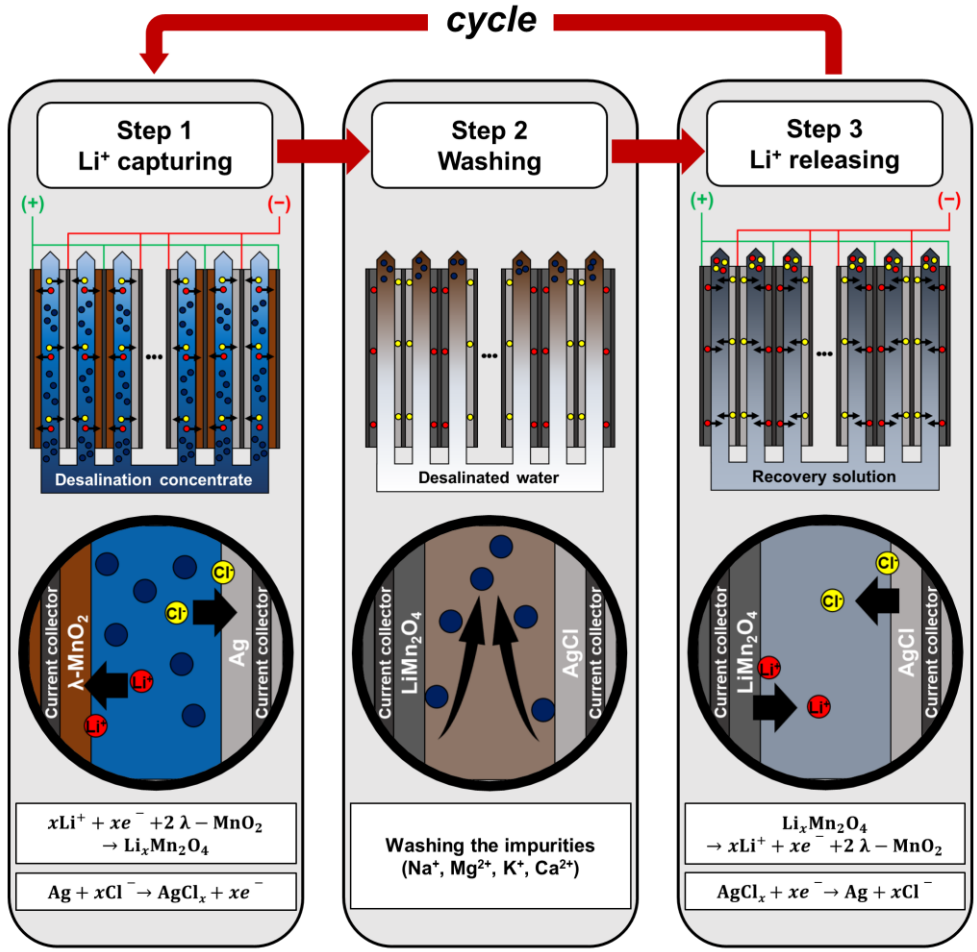

Figure 3-1 Schematic description of the electrochemical lithium recovery process using the λ-MnO_2/Ag electrode stack. In a cycle, there were three steps including Li^+-capturing step (discharging), washing, and Li^+-releasing step (charging)

3.2. Experimental section

3.2.1 Electrode fabrication

The electrochemical monopolar-type stack cell based on 14 pairs of λ-MnO_2 and Ag electrodes was used in the primary recovery process (**Figure 3-2a**). Rectangular graphite plates with 200 mm length, 100 mm width and 2 mm thickness were used as current collectors (**Figure 3-2b**). λ-MnO_2 electrodes were prepared by the acid treatment of $LiMn_2O_4$ composite electrodes in 0.5 M of HCl solution for 1 hour. $LiMn_2O_4$ composite electrode was fabricated by the following steps. First, 80 wt % $LiMn_2O_4$ (TOB New Energy, China) as the active material, 10 wt % Super P (Timcal, Switzerland) as the conductive material, and 10 wt % polyvinylidene fluoride (PVDF, Sigma-Aldrich) as the binder were mixed with the 1-methyl-2-pyrrolidone (NMP, Sigma-Aldrich) solution and the slurry was made. Then, the slurry was cast on the current collector with a thickness of 300 mm, followed by solvent evaporation at the temperature of 120 °C in the vacuum oven. Ag electrodes were prepared in the following steps. 80 wt % silver powder (Ag, Sigma-Aldrich) as the active material, 10 wt % Super P (Timcal, Switzerland) as the conductive material, and 10 wt % polytetrafluoroethylene (PTFE, Sigma-Aldrich) as the binder were mixed with the ethanol (99%, Sigma-Aldrich) and

the slurry was made. The slurry was roll-pressed with a thickness of 300 mm and dried at the temperature of 120 °C in the vacuum oven. After the solvent evaporation, Ag electrodes were attached onto the current collector with the carbon paint (TED PELLA INC., USA).

The electrochemical cell used in the secondary recovery process was comprised of single electrode pair of the λ-MnO_2 and Ag electrode (**Figure 3-2c**). As a current collector, circular graphite sheets with 100 mm diameter and 0.2 mm thickness were used (**Figure 3-2d**). The electrodes used in this process were fabricated in a similar way to the previous one.

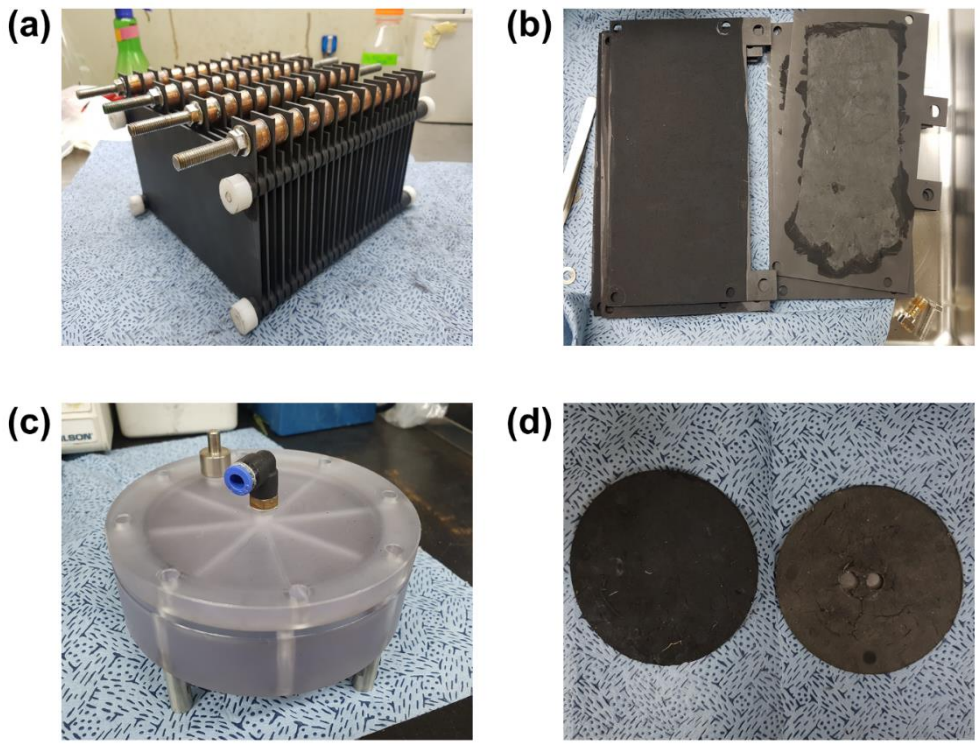

Figure 3-2 (a) The electrode stack used in the primary recovery process and (b) the electrodes comprising the stack. (c) The electrochemical cell used in the secondary recovery process and (d) the electrode comprising the cell

3.2.2 Physicochemical characterization and operation

Physicochemical characterization and operation of the electrochemical cell were conducted by the battery cycler (WBCS3000; WonATech, Korea) and the automated program (CIMON, Korea). The cation concentrations of the intermediate product and the final product were measured by ion chromatography (IC-1100; Thermo-fisher, United states). A pH meter (Lab 860, SI Analytics GmbH) and a conductivity meter (F-74BW, Horiba) were used to characterize the desalination concentrate. TDS and element composition of the desalination concentrate were calculated from the chloride concentration measured by the Ion chromatography (DX-120, Thermo Fisher Scientific Inc.) and the composition of standard seawater (Gerlach 1981).

The performance indicators were defined as follows. Purity is the molar amount of recovered Li^+ divided by the sum of the molar amount of recovered cations, and enrichment factor is the ratio of the Li^+ concentration of the product over the desalination concentrate.

3.2.3 Development of a mobile-type electrode based ELR process

A new electrode configuration, mobile-type electrode, was introduced for scaling up the system while improving product purity and economic efficiency. When mobile-type electrode is applied, the electrode stack can be moved from tank to tank, and its position changes when the step is switched. It is different from the pre-existing fixed-type electrode configuration in which the type of inflow water changes when the step is switched (**Figure 3-3**). In terms of product purity and economy, it is expected that the mobile-type electrode is superior to the fixed-type electrode.

First, it is advantageous to improve product purity. Desalination concentrate is highly concentrated seawater and can act as an impurity when mixed with the recovery solution. Therefore, to effectively separate and purify low-concentration lithium, a process of maximally separating the desalination concentrate and the recovery solution is required. In the fixed-type electrode configuration, these solutions are mixed in the process of repeatedly supplying and draining solutions. As the size of the reactor increases, the opportunity for such a mixing process to occur increases since it is difficult to realize complete drainage in the large reactor. In the case of mobile-type electrode, it can be freed from this problem because the desalination concentrate and the recovery solution can be completely

separated by the partition.

Second, the mobile-type electrode can be used more advantageously and economically for the development of ELR reactor due to easy monitoring and maintenance of the electrode stack. Since fixed-type electrodes are packed inside the cell, it is difficult to monitor and maintain the electrode stack condition. Monitoring and maintenance were easier for the mobile-type electrode because the electrode stack was exposed to the outside. Also, the mobile-type electrode method was an efficient way to save the budget as much as possible because there was almost no need to redesign and manufacture the entire reactor once the frame of the reactor was fabricated.

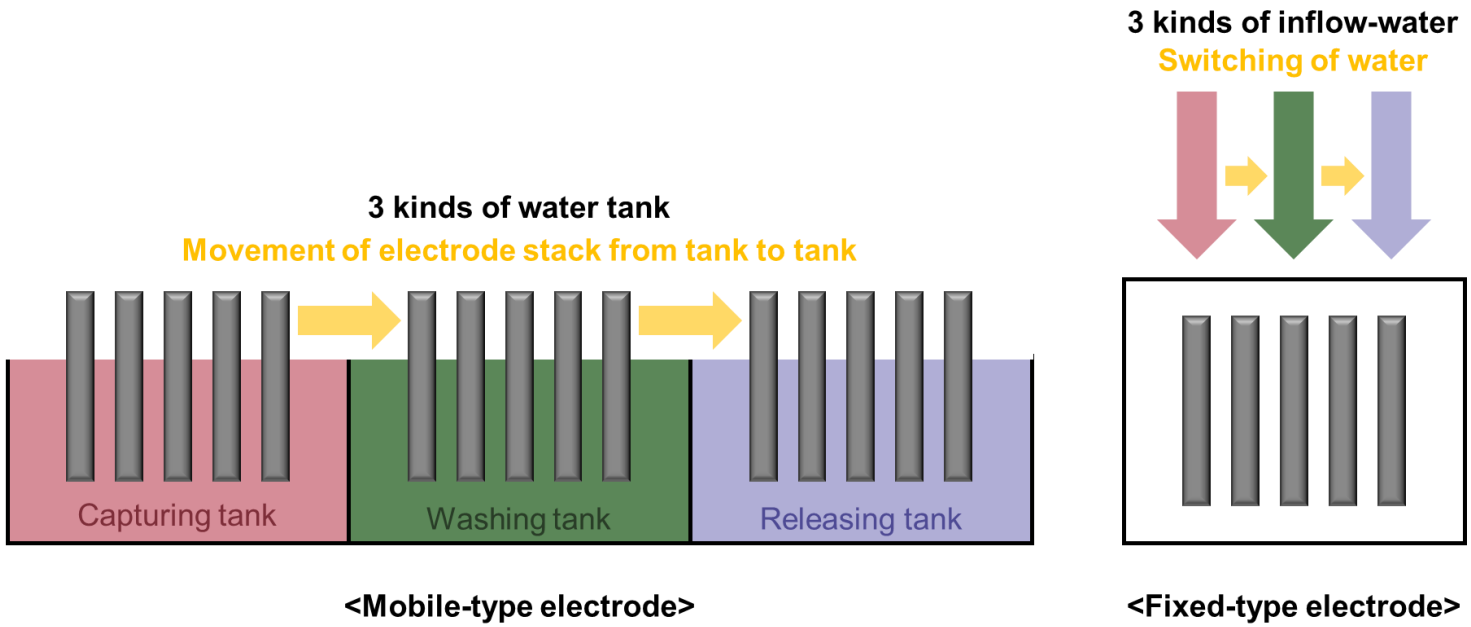

Figure 3-3 Difference between mobile-type and fixed-type electrode configuration

3.3. Results and discussion

3.3.1 Design and installation of the pilot-scale ELR system

Based on these three fundamental steps, the pilot-scale electrochemical lithium recovery system was designed (a photograph of the system is shown in **Figure 3-4**). The system was directly connected to the desalination plant that included reverse osmosis and membrane distillation processes that supplied the desalination concentrate (data of the water quality analysis is shown in **Table 3-1**). The Li^+ concentration of the desalination concentrate was relatively higher than that of seawater. The processes were automated so that the water flow, cell stack movement, and current were controlled by the program. **Figure 3-5** shows the overall constitution of the system whose operation consists of a two-stage consecutive process: the primary recovery process where lithium is recovered directly from desalination concentrate, and the secondary recovery process for further enrichment of lithium ions in final products. In the primary recovery process, three tanks containing desalination concentrate (capturing tank for Step 1), desalinated water (washing tank for Step 2), and recovery solution (releasing tank for Step 3) were used. Since Li^+ concentration in desalination concentrate is extremely low (approximately 0.035 mM), which implies that the amount of lithium

being recovered is likely to be limited by the mass transport of Li^+, the surface area of the electrodes was increased. A stack of 14 pairs of λ-MnO_2 and Ag electrodes in parallel connection was used, and rigid graphite plates were used as current collectors. The system was continuously operated by moving the stack along the conveyor belt and sequentially submerging it in the solutions in the three different tanks.

① Control panel (pump)
② Control panel (primary recovery)
③ Primary recovery system
④ Computer
⑤ Battery cycler
⑥ Secondary recovery system
⑦ Filter (100 μm)
⑧ Pumps and tank
⑨ Pipe lines of the system
⑩ Pipe lines for influents
⑪ Pipe lines for effluents

Figure 3-4 Overview and specification of the pilot-scale electrochemical lithium recovery (ELR) system

Table 3-1 Characterization of the desalination concentrate

Measured properties		
pH	8.0	
Conductivity (S/m)	6.53	
TDS (mg/L)	43895	
Composition		
Compound	Concentration	
	mg/L	mM
Chlorine	25246	712
Sodium	14463	629
Magnesium	1732	71
Sulfur	1215	38
Calcium	553	14
Potassium	536	14
Bromine	90	1
Carbon	38	3
Strontium	11	0.121
Boron	6	0.559
Silicium	3	0.096
Fluorine	2	0.092
Lithium	0.24	0.035
Nitrogen	0.20	0.014
Rubidium	0.16	0.002
Phosphorous	0.08	0.003
Iodine	0.08	0.001

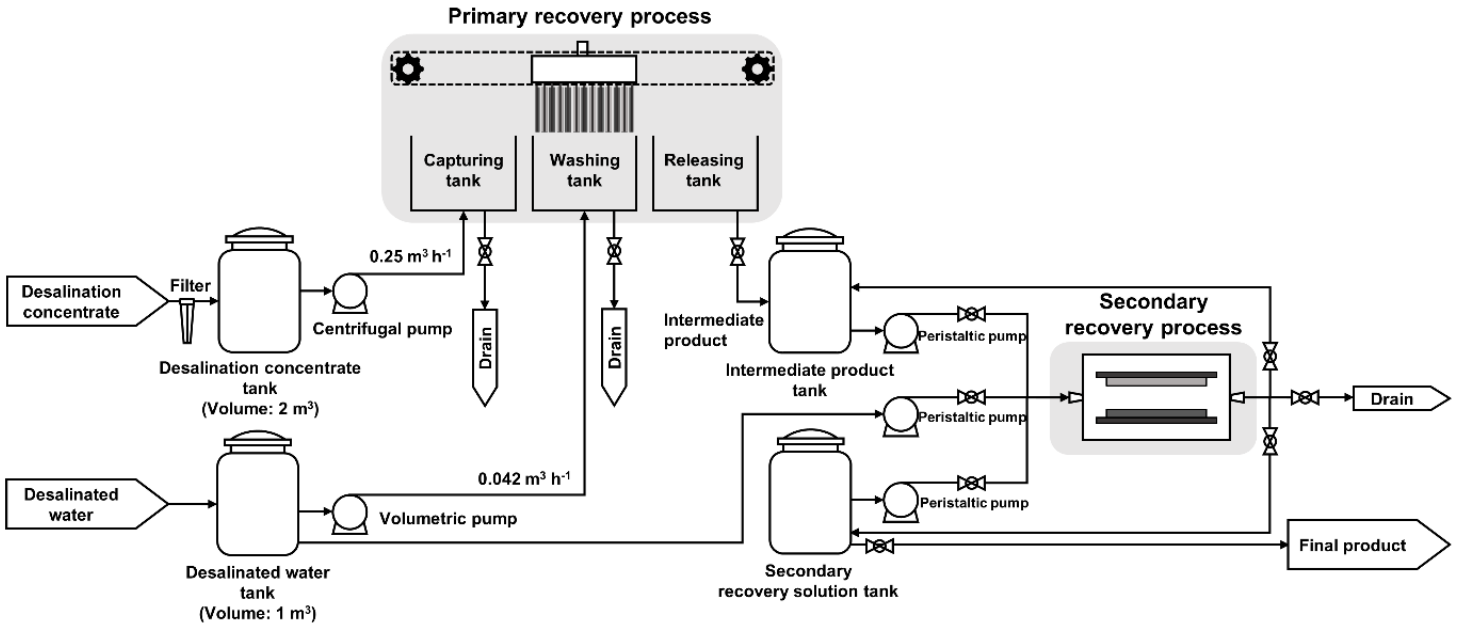

Figure 3-5 Schematic description of pilot-scale electrochemical lithium recovery system

3.3.2 Performance analysis of pilot-scale ELR system

Detailed procedures of the primary recovery process are as follows. In Step 1, after locating the electrodes in the capturing tank where the desalination concentrate flows at a rate of 0.25 m^3/h, lithium ions were extracted by discharging the system by applying –10 μA/cm^2 of current until the voltage decreased to 0.2 V (see the black line of the voltage profile in **Figure 3-6a**). After capturing Li^+, the electrodes were transferred to the washing tank and impurities were removed using desalinated water with a flow rate of 0.042 m^3/h (Step 2). Then, the electrodes were transferred to the releasing tank, and +50 μA/cm^2 of current was applied until the voltage reached 1.2 V (see the red line of the profile in **Figure 3-6a**) to release Li^+ from the electrodes to the electrolyte (Step 3). The operating voltage range was determined by considering the reduction peaks (0.6 to 0.2 V) and oxidation peaks (0.5 to 1.1 V) of a λ-MnO_2 electrode in LiCl solution via cyclic voltammetry analysis (see **Figure 3-7**). This three-step cycle was repeated five times before moving the recovery solution to the secondary recovery process.

For Li^+ enrichment in the secondary recovery process, a pair of stationary electrodes was used to constitute a flow-type reactor with a small volume (for the details, see **Figure 3-2c** and **d**). The reasons are because (i)

the amount of solution used to capture Li^+ is much smaller compared with the primary stage; (ii) more thorough washing of impurities is necessary to obtain a purified final product; and (iii) the volume of the recovery solution should be minimized to obtain a final product with high Li^+ content. The secondary process also consists of the three steps discussed above. In Step 1, the recovery solution from the primary stage, hereafter denoted as the intermediate product, was fed into the cell from the intermediate product tank (the semi-batch process, see **Figure 3-5**), followed by Li^+ capture by discharging (at –10 μA/cm^2, see the black line of the profile in **Figure 3-6b**). After the completion of the capturing step, the solution was returned to the tank by the control of the streamline and valves, and Step 2 (washing) was accomplished by flowing the desalinated water from the desalinated water tank. For Step 3, the secondary recovery solution was circulated to the cell from the secondary recovery solution tank, and lithium ions were released by applying +50 μA/cm^2 of current (see the red line of the profile in **Figure 3-6b**). After the Li^+-releasing step, the recovery solution returned to the tank. The secondary recovery process was also repeated five times, and the final product was obtained.

The concentrations of Li^+, Na^+, Mg^{2+}, and Ca^{2+} in desalination concentrate, intermediate product, and final product were measured, and the

results are summarized in **Table 3-2** and **Figure 3-6c** to **Figure 3-6e**. As depicted in **Figure 3-6c**, the concentration of Li^+ in the desalination concentrate was 0.035 mM, whereas those of Na^+, Mg^{2+}, and Ca^{2+} were 630, 71, and 14 mM, respectively. By the primary recovery process, Li^+ was separated from the desalination concentrate with high selectivity. The concentration of Li^+ increased to 0.12 mM, while the amounts of Na^+, Mg^{2+}, and Ca^{2+} were reduced to 3.0, 0.66, and 0.31 mM, respectively (see **Figure 3-6d**). After the secondary process, Li^+ concentration further enriched to 62 mM, while the content of other ions remained close to those of the intermediate product. The concentrations of Na^+, Mg^{2+}, and Ca^{2+} were 2.6, 3.0, and 2.8 mM, respectively (see **Figure 3-6e**).

In order to evaluate the lithium selectivity of the pilot-scale system, the selectivity coefficient ($K_{Li/M}$, the amount of recovered Li^+ divided by the amount of cation M) was calculated for each ion at different stages of operation. In desalination concentrate, $K_{Li/M}$ was extremely small in all cases (5.6×10^{-5}, 4.9×10^{-4}, and 2.5×10^{-3} for Na^+, Mg^{2+}, and Ca^{2+}, respectively). However, it increased by 724, 373, and 158 times for Na^+, Mg^{2+}, and Ca^{2+}, respectively, after the primary process. In the final product, regardless of M, the $K_{Li/M}$ values were greater than 20. These results confirm that lithium ions were selectively transferred from the desalination concentrate to the final

product in the pilot-scale system. Furthermore, the purity (K_{Li}, the molar amount of recovered Li^+ divided by sum of the molar amount of recovered cations) and enrichment factor (f, the ratio of the Li^+ concentration of the product and the desalination concentrate) were calculated in desalination concentrate, intermediate product, and final product. As shown in **Figure 3-6f**, the purity of Li^+ increased from 0.0048% to 88% after the operation of our pilot-scale system, and Li^+ was enriched by 1800 times as seen from the values of f in **Figure 3-6g**.

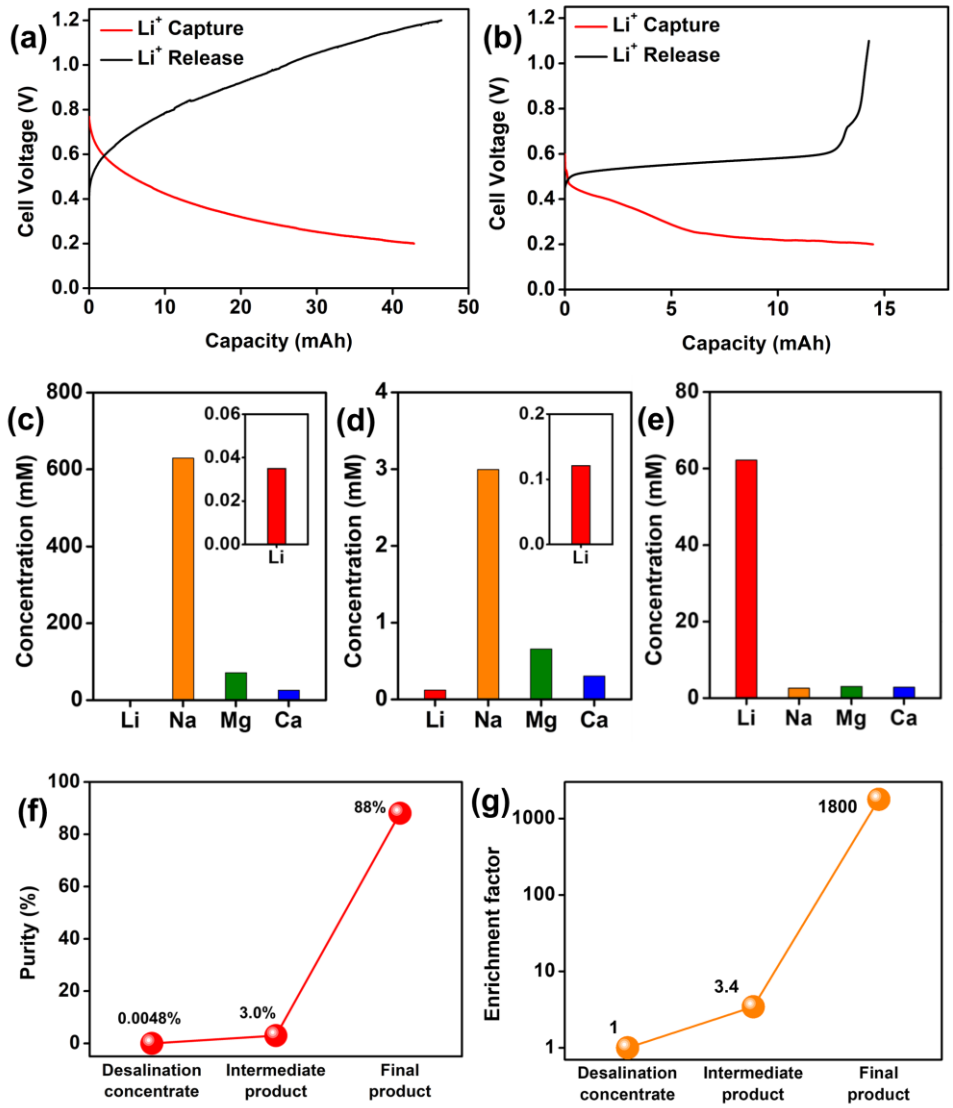

Figure 3-6 Analysis of the pilot-scale electrochemical lithium recovery system: Cell voltage profile with capacity at (a) the primary recovery process and (b) the secondary recovery process under the current density of –10 μA/cm^2 (Li^+-capturing step) and +50 μA/cm^2 (Li^+-releasing step); Concentration of the representative cations dissolved in (c) the desalination concentrate, (d) the intermediate product, and (e) the final product; (f) purity and (g) enrichment factor of the desalination concentrate, intermediate product, and final product.

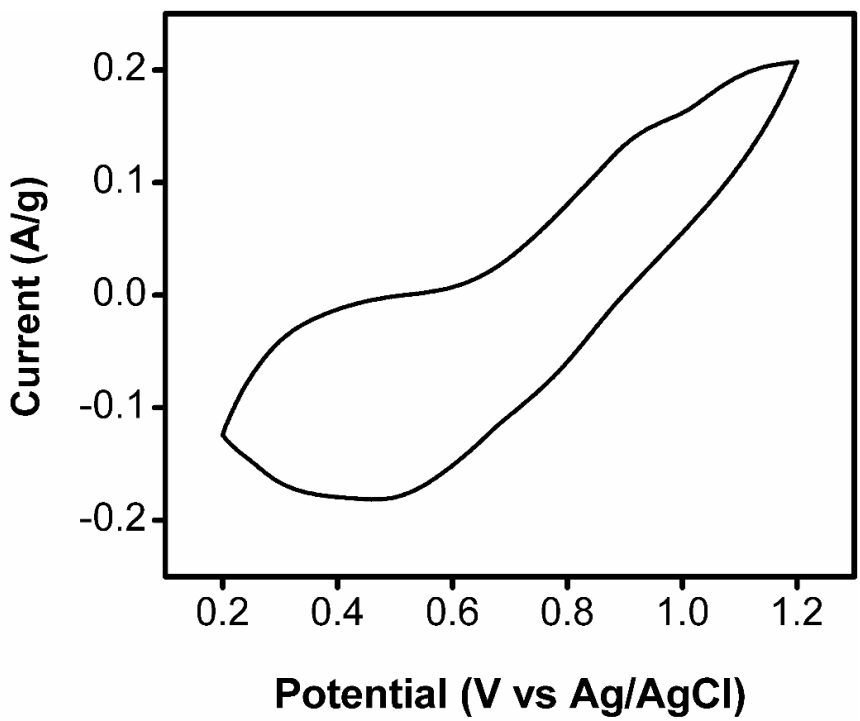

Figure 3-7 Cyclic voltammogram of λ-MnO_2 electrode (1 M LiCl, 1 mV/s)

Table 3-2 Concentrations of Li^+, Na^+, Mg^{2+}, and Ca^{2+} of the desalination concentrate, intermediate product, and final product

	Desalination concentrate	Intermediate product	Final product
C_{Li} (mM)	0.035	0.12	62
C_{Na} (mM)	630	3.0	2.6
C_{Mg} (mM)	71	0.66	3.0
C_{Ca} (mM)	14	0.31	2.8

3.4. Summary

In this research, a pilot-scale electrochemical lithium recovery system based on λ-MnO_2/Ag electrode pairs was designed and demonstrated. Although this work is the first demonstration of the large-scale operation of an electrochemical lithium recovery system, Li^+ was successfully extracted and enriched, and a final product with Li^+ enriched by 1800 times and 88% purity was obtained using two consecutive processes for Li^+ recovery from desalination concentrate. This work not only verifies the feasibility of electrochemical lithium recovery technology but also provides insights on various considerations for designing large-scale electrochemical systems, such as the importance of properly combining multiple steps. It is expected that these efforts lead to the development of improved systems and advance the commercial use of diverse electrochemical separation technologies.

4. Application of flow-type electrochemical lithium recovery system with λ-MnO_2/$LiMn_2O_4$: Experiment and simulation

4.1. Introduction

Lithium is one of the most widely used metal resources in the world, and its value has become significant owing to the explosive expansion of the rechargeable battery market in the past 25 years (Vikström et al. 2013; Martin et al. 2017; Park et al. 2019; Sung et al. 2019). The demand for lithium is expected to soar dramatically after the 2020s, outstripping the supply of this valuable metal (Wanger 2011). To overcome the potential risk of lithium deficiency, it is necessary to develop a well-designed system to acquire lithium resources. One of the prominent candidates is the electrochemical lithium recovery (ELR) system. Using this system, aqueous lithium resources can be recovered faster and in a more environment-friendly manner compared to the conventional technology—lime soda evaporation (Zhao et al. 2019; Calvo 2019).

Most previous studies on the ELR system have mainly focused on electrode materials. In an early study, an electrochemical system, composed of λ-MnO_2 and Pt electrodes, was demonstrated for Li^+ recovery from

geothermal water (Kanoh et al. 1993). In this system, the λ-MnO_2 obtained from spinel $LiMn_2O_4$ was chosen as the lithium intercalating electrode material because this absorbent material has high lithium selectivity against inert cations, especially magnesium ions. The Pt/λ-MnO_2 system exhibited high Li^+ selectivity but low energy efficiency. Therefore, battery systems with low energy consumption were required for subsequent studies. Representative lithium-ion battery cathode materials such as λ-MnO_2 (Lee et al. 2013) and olivine $LiFePO_4$ (Pasta et al. 2012) were introduced into the systems and an Ag/AgCl electrode was introduced as the Cl^- capturing anode. To improve the Li^+ recovery performance, λ-MnO_2/polypyrrole (PPy)/polystyrene sulfonate (PSS) core–shell nanorod coated (Du et al. 2016), λ-MnO_2 graphene composite (Zhang et al. 2019a), $Li_{1-x}Ni_{1/3}Co_{1/3}Mn_{1/3}O_2$ (Lawagon et al. 2018), and $Li_{1-x}Ni_{0.5}Mn_{1.5}O_2$ electrodes (Lawagon et al. 2019) were suggested as cathodes for the ELR system. Studies on Li^+ intercalation (Marchini et al. 2018b) and cathode degradation (Marchini et al. 2018a) were also conducted to better understand the underlying mechanism in this system. Nickel hexacyanoferrate (Trócoli et al. 2014, 2015, 2016, 2017), I^-/I_3^- redox couple (Kim et al. 2015a), activated carbon (Kim et al. 2015b), zinc (Kim et al. 2018b), polyaniline (Zhao et al. 2019), and polypyrrole (Marchini et al.

2016) electrodes were also utilized as economical alternatives for the silver counter electrode.

Along with studies on electrode materials, the study of efficient system design is essential for the commercialization of the technology. Rocking-chair ELR systems such as $LiFePO_4/FePO_4$ (Zhao et al. 2013; Liu et al. 2014; He et al. 2018) and $LiMn_2O_4/Li_{1-x}Mn_2O_4$ (Zhao et al. 2017; Marchini et al. 2018c) have been investigated. These systems consisted of two identical battery cathode materials, and the separator channels were divided by an anion exchange membrane (AEM), allowing the simultaneous capture and release of Li^+ without a distinct electrode regeneration step. However, little research has been done on the flow-type reactor that is advantageous for products with uniform quality, bulk processing for practical applications, and alleviating the concentration polarization. Meanwhile, for improving the mass transport of Li^+ by convective flow, a flow-through reactor has been developed whose performance was investigated by studying the effect of major parameters (Palagonia et al. 2017, 2019, 2020). Using the flow-type reactor, the concentration polarization of Li^+ around the electrode was reduced, leading to an increase in the energy efficiency of the system. However, the behavior of ion species with the convective mass transfer is not analyzed.

In recent studies, numerical simulations have been performed to investigate the behavior of symmetrical desalination systems adopting intercalation materials (Singh et al. 2019). The theory of capacitive deionization (CDI) with porous intercalation electrodes was suggested based on the Nernst–Planck equation and Frumkin isotherm (Singh et al. 2018). A novel desalination concept, Na-Ion Desalination (NID), was proposed, and the flow-through reactor composed of the two symmetrical sodium-ion battery electrodes ($Na_{0.44}MnO_2$) was analyzed based on the porous-electrode model (Smith and Dmello 2016). Prussian blue analogues were also utilized as the electrode material for the demonstration of the Cation Intercalation Desalination (CID) cell (Porada et al. 2017). The effects of the cell architectures on CID system performance were evaluated theoretically (Smith 2017) and the membrane-free CID system was examined in terms of energy consumption and salt removal rate (Liu and Smith 2018). Investigation and optimization of the formulation of the flow through electrode in CID cell were conducted (Reale et al. 2019).

In comparison with the study of desalination systems, there is not enough simulation study of ELR systems. To analyze the behavior of various ionic species in a packed bed reactor, a numerical simulation was conducted based on the Nernst–Planck equation and the battery intercalation model (Romero

et al. 2018). However, the effect of convective flow in the separator channel could not be examined because a one-dimensional model was used in this study, in which the mass transfer of the electrolyte would significantly be impacted by the flow characteristics of the separator channel (Gu et al. 2017; Jung et al. 2018; Usta et al. 2018).

In the present study, a rocking-chair ELR system is applied as a flow-type system with analysis based on experiment and simulation. To the best of our knowledge, this is the first study to apply a flow-type reactor to the λ-MnO_2/$LiMn_2O_4$ system and to attempt two-dimensional numerical simulations on a rocking-chair ELR system. The flow-type reactor is designed and operated under the constant-current mode, monitoring the effluent concentration and electrolyte conductivity. A two-dimensional numerical simulation is performed considering the flow characteristics of the separator channel to understand the system behavior. The concentration distributions of Li^+ in the spacer-filled and porous electrode channels are investigated during the electrochemical reaction. The energy consumption for Li^+ recovery is also calculated by considering energy recovery, indicating the high level of energy efficiency of this system. Although removing other cations (for example, Na^+ and Mg^{2+}) from the brine water and improving product purity are important issues for the ELR system, it is not possible to simulate a multi-cation system

precisely since the definite effect of other cations is not yet fully understood. Therefore, this study is focused on the understanding of the intercalation and ion transport phenomena of Li^+ in the reactor, as an early simulation research of the ELR system.

4.2. Experimental section

4.2.1 System definition

Figure 4-1 illustrates the schematic diagram of the rocking-chair ELR system. This system consisted of a pair of identical porous lithium manganese oxide (LMO) electrodes (λ-MnO_2 and $LiMn_2O_4$) with different state-of-charge (SoC). The separator channel between the electrodes was divided by the AEM, and the two channels were referred to as the catholyte channel (the separator channel adjacent to the cathode) and the anolyte channel (the separator channel adjacent to the anode). At step 1, by applying a negative current between the electrodes, the potential of the positive electrode (λ-MnO_2) decreased and the potential of the negative electrode ($LiMn_2O_4$) increased; therefore, the cell voltage decreased as step 1 proceeded. At the same time, Li^+ from the catholyte channel was intercalated into the λ-MnO_2 electrode by the reduction reaction and Li^+ from the anolyte channel was de-intercalated from the $LiMn_2O_4$ electrode by the oxidation reaction. The reaction equations were as follows:

$$Li^+ + 2\lambda - MnO_2 + e^- \rightarrow LiMn_2O_4 \text{ (at cathode interface)}$$

$$LiMn_2O_4 \rightarrow Li^+ + 2\lambda - MnO_2 + e^- \text{ (at anode interface)}$$

The intercalation and de-intercalation reactions of Li^+ caused a charge imbalance in the catholyte and anolyte, and Cl^- diffused from the catholyte channel to the anolyte channel through the AEM. Therefore, the concentrations of Li^+ and Cl^- decreased in the catholyte channel and increased in the anolyte channel. In summary, a Li^+ diluted solution was produced in the catholyte channel by the lithium-capturing step, and a Li^+ concentrated solution was produced in the anolyte channel by the lithium-releasing step.

When the cell voltage reached the voltage limit, the SoC of the two electrodes was reversed compared to the beginning of step 1, and step 1 was completed thereafter. At step 2, by applying a positive current between the electrodes, the potential of the positive electrode increased and that of the negative electrode decreased. Therefore, the cell voltage increased as step 2 proceeded. As step 2 was completely identical to step 1 with the opposite direction of the current, the directions of mass transfer and reaction in step 2 were opposite to those in step 1. When the cell voltage reached the voltage limit, step 2 was completed and step 1 was started again. By switching steps 1 and 2, lithium capturing, and releasing can be carried out simultaneously without any additional electrode regeneration steps.

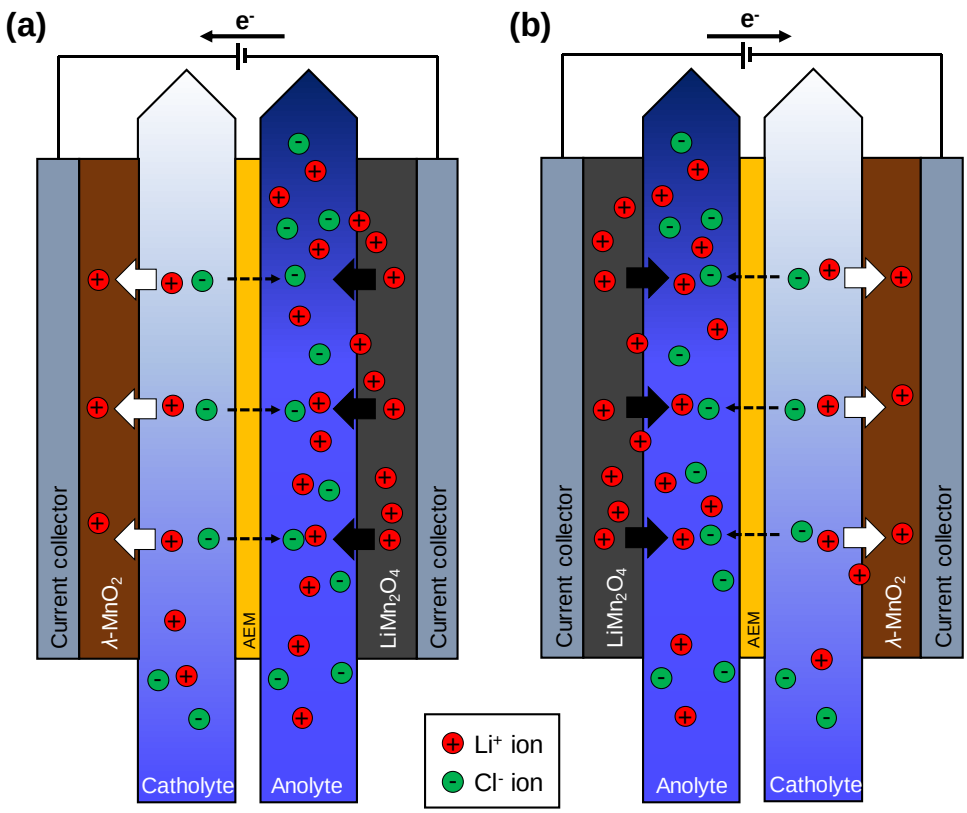

Figure 4-1 Schematic diagram of λ-MnO_2/$LiMn_2O_4$ system at (a) step 1 (intercalation reaction of Li^+ into positive electrode and de-intercalation reaction of Li^+ from negative electrode) and (b) step 2 (de-intercalation reaction of Li^+ from positive electrode and intercalation reaction of Li^+ into negative electrode). White arrows indicate intercalation reaction of Li^+, black arrows indicate de-intercalation reaction of Li^+, and dashed arrows indicate the diffusion of Cl^- through AEM.

4.2.2 Electrode fabrication and cell assembly

The $LiMn_2O_4$ composite electrode was fabricated as follows. 80 wt% $LiMn_2O_4$ (TOB New Energy, China), 10 wt% Super P (Timcal, Switzerland), and 10 wt% polyvinylidene fluoride (PVDF; Sigma-Aldrich, USA) were mixed with 1-methyl-2-pyrrolidone (NMP; Sigma-Aldrich, USA). The mixture was cast on a graphite sheet and dried at 120 °C in a vacuum oven (mass loading of active material: 5 mg cm^{-2}). After the $LiMn_2O_4$ composite electrode was obtained, it was electrochemically de-lithiated under a constant voltage of 1.2 V (vs Ag/AgCl, saturated KCl) for 120 min to prepare the λ-MnO_2 electrode. **Figure 4-2** illustrates the cell assembly of the flow-type ELR system based on the λ-MnO_2/$LiMn_2O_4$ electrode. The λ-MnO_2 electrode and $LiMn_2O_4$ electrode were cut in square shapes (2.0 cm × 2.0 cm) and placed on the rigid graphite. The separator channel was supported by a net-type nylon woven mesh filter (Yamanaka Industry Co., Ltd, Japan), and it was separated into two channels by the AEM (AMV; Selemion, Japan). The cell was packed using a silicon gasket and end plate.

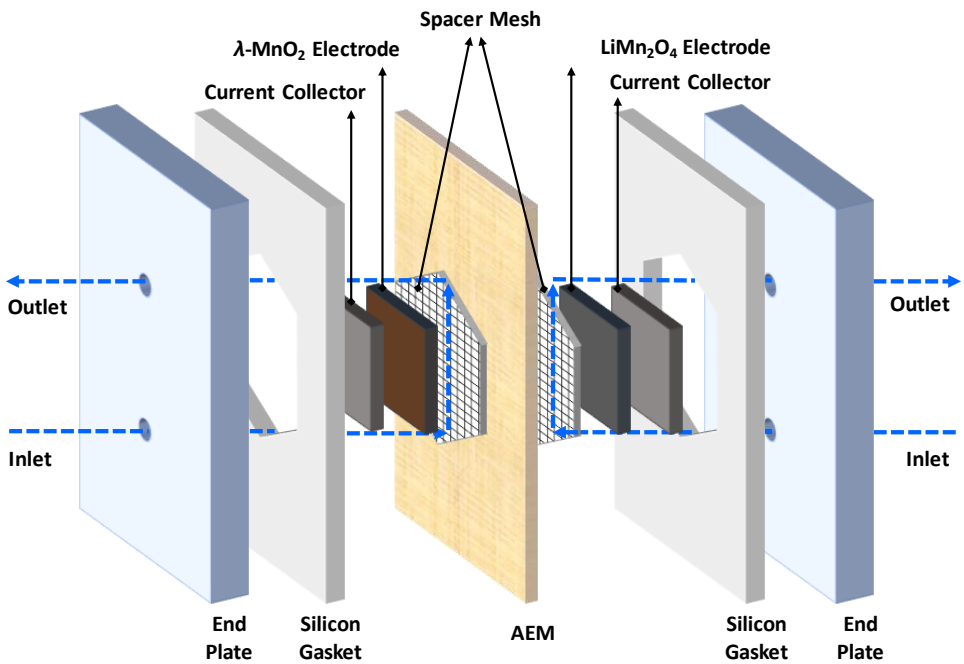

Figure 4-2 Cell assembly of flow-type rocking-chair ELR system. Two water streams (blue dashed arrows) enter two inlet holes, pass through spacer mesh, and drain through two outlet holes.

4.2.3 ELR process operation and performance parameter

In this study, the rocking-chair ELR system is a two-electrode system that was operated under a constant-current mode (current density: ± 6.25×10^{-2}, 1.25×10^{-1}, and 2.50×10^{-1} mA cm^{-2}). The negative current was applied to the system until the cell voltage reached –0.7 V in step 1 and the positive current was applied to the system until the cell voltage reached +0.7 V in step 2 using a battery cycler (WBCS3000; WonATech, Korea). Electrode characterization was performed by cyclic voltammetry (CV) analysis and the galvanostatic discharging/charging test using the same battery cycler (see **Figure 4-3**). Influent supplied to each separator channel (catholyte and anolyte channels) using a peristaltic pump (REGLO ICC; ISMATEC, USA) was 30 mM LiCl aqueous solution and the flow rate was 1 ml min^{-1} (Note that the target lithium sources in this study are brines such as Salar de Uyuni, which contains 10 to 220 mM of Li^+ (Ericksen et al. 1978). A concentration of 30 mM was selected which is within the lithium concentration range of Salar de Uyuni). The conductivity of the effluent was measured using a conductivity meter (3574-10C; Horiba, Japan) and the Li^+ concentration was calculated from the conductivity.

Several performance parameters were calculated using the voltage–capacity profile and conductivity data. The specific capacity (Q, unit: mAh g^{-1}) is defined as

$$Q = \frac{|I|t}{\alpha m_{\text{elec}}} \tag{4-1}$$

where I is the applied current (unit: mA), t is operation time (unit: h), α is the mass fraction of the electrode which consists of active material (the value is 0.8 in this paper), and m_{elec} is the mass of an electrode (unit: g).

The specific mass of Li^+ recovered (q_{Li^+}, unit: mg g^{-1}) is defined as

$$q_{Li^+} = \frac{\bar{u} m_{Li^+} \int |c(0) - c(t)| dt}{\alpha m_{\text{elec}}} \tag{4-2}$$

where $\bar{u}$ is the flow rate (unit: mL min^{-1}), m_{Li^+} is the molar mass of Li^+ (unit: g mol^{-1}), $c(0)$ is the initial concentration of LiCl, and $c(t)$ is the concentration of LiCl with respect to time (unit: mol mL^{-1}).

The energy consumption at the phase i (W_i, unit: Wh) is defined as

$$W_i = I \int \Delta E(t) dt \tag{4-3}$$

where ΔE is the cell voltage with respect to time (V). The ELR process is divided into the energy consumption phase (subscript: c) and the energy recovery phase (subscript: r).

The specific total energy consumption of the ELR system (W_{total}, Wh mol^{-1}) is defined as the net amount of energy consumed divided by the number of moles of recovered Li^+.

$$W_{total} = \frac{W_c}{\bar{u}\int |c(0) - c(t)|\, dt} \quad \text{(Without energy recovery)} \tag{4-4}$$

$$W_{total} = \frac{W_c - W_r}{\bar{u}\int |c(0) - c(t)|\, dt} \quad \text{(With energy recovery)} \tag{4-5}$$

Details of the calculation based on energy recovery will be explained in section 4.4.3.

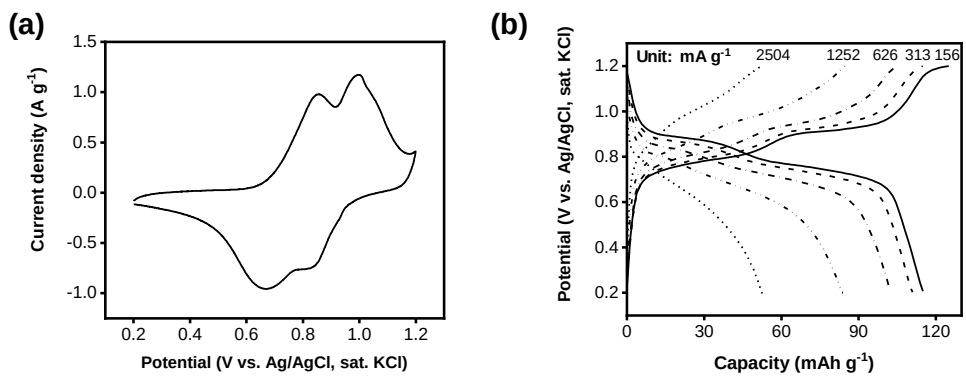

Figure 4-3 (a) Cyclic voltammetry (scan rate: 1 mV s^{-1}) and (b) galvanostatic charge/discharge test for the $LiMn_2O_4$ electrode in 1 M LiCl (current density: 156, 313, 626, 1252, 2504 mA g^{-1}).

4.3. Modeling and simulation

4.3.1 Problem statement

Figure 4-4 illustrates the simulation domain used in this study. To incorporate the crossflow operation of the electrochemical lithium recovery system, a two-dimensional simulation domain was constructed, which contains positive and negative electrodes (Ω_{ep} and Ω_{en} , respectively) connected to the imaginary current collectors, two separators (Ω_s) with feed spacers, AEM (Ω_m), and rectangular spacer meshes inserted into channel to mimic net-type mesh filter used in experiment (see **Figure 4-8a** and **Figure 4-9** to check the structure). Several previous models and simulation studies were referred for the development of our model (Doyle et al. 1993; Fuller 1994; Ramadesigan et al. 2012; Jokar et al. 2016).

A mass balance equation for Li^+ with its electrochemical intercalation reaction was solved in this study, incorporating its convective transport in the separator channel and its counter-ion transfer through a fully blocking AEM. The general form of the mass balance equation for the *i*th species in a porous material and the charge neutrality equation is as follows:

$$\varepsilon_l \frac{\partial c_i}{\partial t} + \nabla \cdot \mathbf{N}_i = S_i \qquad \text{in } \Omega_s, \Omega_{ep}, \text{and } \Omega_{en} \qquad (4\text{-}6)$$

$$\sum_i z_i c_i = 0 \qquad \text{in } \Omega_s, \Omega_{ep}, \text{and } \Omega_{en} \qquad (4\text{-}7)$$

in which ε_i is the volume fraction of the liquid phase, c_i is the concentration of species *i*, z_i is the variance in c_i, $\mathbf{N}_i$ is its total mass flux, and S_i is the source term, which is the rate of production or consumption of species *i*. The Nernst–Planck equation is introduced to describe the total mass flux of a charged chemical species (i.e., electrolyte), which includes diffusion, migration, and convection of the species.

$$\mathbf{N}_i = -D_{i,\text{eff}} \nabla c_i - z_i \mu_{i,\text{eff}} F c_i \nabla \varphi_l + \mathbf{u} c_i \qquad \text{in } \Omega_s, \Omega_{ep}, \text{and } \Omega_{en} \qquad (4\text{-}8)$$

in which D_i is the effective diffusivity of the species *i* in a porous media, $\mu_{i,\text{eff}}$ is its effective mobility in a porous media, F is Faraday's constant, φ_l is the electrolyte potential, and $\mathbf{u}$ is the flow velocity vector. The mobility of a species is calculated using the Nernst–Einstein relation (Eq. (4-9)), and the Bruggeman correction is introduced in this model to represent the effective mass transport in a porous media (Eq. (4-10)).

$$\mu_{i,\text{eff}} = D_{i,\text{eff}} / RT \qquad (4\text{-}9)$$

$$D_{i,\text{eff}} = \varepsilon_l^{1,5} D_i \qquad (4\text{-}10)$$

Where D_i is the bulk diffusivity of species *i*, R is the molar gas constant

and T is temperature, which is fixed at 298 K in this study.

In our electrochemical reactor consisting of two electrodes and separators ($\Omega_s, \Omega_{ep}, \text{and } \Omega_{en}$), the electronic current density in the solid and liquid phases are conserved, and, thus, the cell current density vector ($\mathbf{I}_{cell}$) is defined as follows:

$$\nabla \cdot \left(\mathbf{i}_l + \mathbf{i}_s \right) = 0 \qquad \text{in } \Omega_s, \Omega_{ep}, \text{and } \Omega_{en} \qquad (4\text{-}11)$$

$$\mathbf{I}_{cell} = \mathbf{i}_l + \mathbf{i}_s \qquad \text{in } \Omega_s, \Omega_{ep}, \text{and } \Omega_{en} \qquad (4\text{-}12)$$

in which $\mathbf{i}_l$ is the electrolyte current density vector and $\mathbf{i}_s$ is the electrode current density vector. $\mathbf{I}_{cell}$ is assumed to be a constant vector, which is imposed as the boundary condition at the outer boundaries of the electrodes. When $\mathbf{n}_x \cdot \mathbf{I}_{cell} < 0$, Li^+ is intercalated into the positive LMO electrode (reduction of the positive LMO electrode, see **Figure 4-1a**), whereas when $\mathbf{n}_x \cdot \mathbf{I}_{cell} > 0$, Li^+ is de-intercalated from the positive LMO electrode (oxidation of the positive LMO electrode, see **Figure 4-1b**). Here, $\mathbf{n}_x$ is the unit vector along the *x*-direction. The electrolyte and electrode current densities are computed using the following equations:

$$\mathbf{i}_l = F \sum_i z_i \left(-D_{i,\text{eff}} \nabla c_i - z_i \mu_{i,\text{eff}} F c_i \nabla \varphi_l \right) \qquad \text{in } \Omega_s, \Omega_{ep} \text{ and } \Omega_{en} \qquad (4\text{-}13)$$

$$\mathbf{i}_s = -\sigma_{s,\text{eff}} \nabla \varphi_s \qquad \text{in } \Omega_s, \Omega_{ep} \text{ and } \Omega_{en} \qquad (4\text{-}14)$$

in which $\sigma_{s,\text{eff}}$ is the effective conductivity of the solid material (i.e., LMO), expressed as

$$\sigma_{s,\text{eff}} = \varepsilon^{1.5}\sigma_s \qquad \text{in } \Omega_s, \Omega_{ep} \text{ and } \Omega_{en} \qquad (4\text{-}15)$$

where σ_s is the conductivity of the solid material, and φ_s is the electrode potential. The Bruggeman correction is also used to calculate $\sigma_{s,\text{eff}}$.

In each simulation sub-domain, the positive and negative electrodes (Ω_{ep} and Ω_{en}), the spacer channel (Ω_s), and the AEM domain (Ω_m)—the terms in Eq. (4-6) and Eq. (4-8)—are dealt with in different manners. After constructing the governing equations for the mass balance equation and the charge transfer equation, the initial and boundary conditions are imposed at each boundary. It should be mentioned here that, in the AEM domain (Ω_m), a fixed membrane charge was assumed and the Nernst–Planck equation was not solved in this domain (it is depicted in Eq. (4-26)).

In the separator channel domain (Ω_s), where a dilute LiCl solution is injected, ε_i is set to unity ($\varepsilon_i = 1$) and no additional reaction is assumed ($S_i = 0$), which yields a mass transport problem without a source term. To calculate the convective transport of the ion, a laminar flow field of the Newtonian fluid in Ω_s is given from the solution of the Navier-Stokes equation and the fluid continuity equation.

$$\rho_{\mathrm{f}}\left(\mathbf{u}\cdot\nabla\mathbf{u}\right)=-\nabla p+\eta_{\mathrm{f}}\nabla^{2}\mathbf{u} \qquad \text{in } \Omega_s \qquad (4\text{-}16)$$

$$\nabla\cdot\mathbf{u}=0 \qquad \text{in } \Omega_s \qquad (4\text{-}17)$$

in which ρ_{f} is the density of the fluid, p is the pressure, and η_{f} is the viscosity of the fluid. Since an extremely dilute LiCl solution (30 mM) is considered in this simulation, the density and the viscosity of the fluid are assumed to be constant same as those of pure water (see **Table 4-1**). The parabolic velocity field of a fully-developed laminar flow is assumed at the inlet of the channel (Γ_i), where the average inlet velocity is u_{avg}. Square-shaped obstacles are placed within the channel to model the net-type spacer used in the experiment. The length of the square obstacle is 80 μm, which corresponded to the hydraulic diameter of the cylindrically-shaped feed spacer threads which have the same diameter of 80 μm in the experiment. The surface-to-surface distance between two adjacent square obstacles is 220 μm. Buffer regions whose length is 400 μm was placed near the inlet and outlet, where no square obstacles are placed to avoid unexpected numerical artifacts by the presence of the obstacles near the inlet and outlet. No-slip and non-penetration boundary conditions ($\mathbf{u}=\mathbf{0}$) are imposed on the channel wall and surface of the feed spacer (Γ_w). A pressure boundary condition is assumed at the outlet (Γ_o).

In the electrode domains (Ω_{ep} and Ω_{en}), however, one should consider electrochemical reactions of lithium intercalation which provides the source term in the mass balance equation (S_i). It was assumed that a Butler-Volmer form of electrochemical kinetics is held in the lithium intercalation reaction as below:

$$i_{loc} = i_0 \left(\exp\left(\frac{\alpha_a F \eta}{RT} \right) - \exp\left(-\frac{\alpha_c F \eta}{RT} \right) \right) \qquad \text{in } \Omega_{ep} \text{ and } \Omega_{en} \qquad (4\text{-}18)$$

$$i_0 = F \left(k_c\right)^{\alpha_c} \left(k_a\right)^{\alpha_a} \left(c_{s,\max} - c_s\right)^{\alpha_a} \left(c_s\right)^{\alpha_c} \left(c_{\mathrm{Li}^+} / c_{\mathrm{Li}^+,\mathrm{ref}}\right)^{\alpha_a} \qquad \text{in } \Omega_{ep} \text{ and } \Omega_{en} \qquad (4\text{-}19)$$

$$\eta = \varphi_s - \varphi_l - E_{eq} \qquad \text{in } \Omega_{ep} \text{ and } \Omega_{en} \qquad (4\text{-}20)$$

$$S_i = \frac{v_{\mathrm{Li}^+} a_v i_{loc}}{nF} \qquad \text{in } \Omega_{ep} \text{ and } \Omega_{en} \qquad (4\text{-}21)$$

in which i_{loc} is the local current density, i_0 is the exchange current density, α_a is the anodic reaction rate coefficient in the electrode, α_c is the cathodic reaction rate coefficient in the electrode, η is the overpotential, k_a is the anodic reaction rate constant in the electrode, k_c is the cathodic reaction rate constant in the electrode, c_s is the concentration of lithium in the solid particle phase (i.e., in the LMO particles), $c_{s,\max}$ is the maximum concentration of lithium in the solid particle phase, c_{Li^+} is the concentration of Li^+ ion in the liquid phase, $c_{\mathrm{Li}^+,\mathrm{ref}}$ is the reference concentration of Li^+ in

the liquid phase, E_{eq} is the equilibrium potential (see **Figure 4-5**), v_{Li^+} is the stoichiometric coefficient of the reduction equation of Li^+, a_v is the active specific surface area [m^{-1}], and n is the number of electrons participating in the electrochemical reaction.

The concentration of lithium in the solid particle phase (c_s) at a specific time is given from the solution of an ordinary differential equation defined in the spherical coordinate system.

$$\frac{\partial c_s}{\partial t} = D_s\left[\frac{\partial^2 c_s}{\partial r^2} + \frac{2}{r}\frac{\partial c}{\partial r}\right] \qquad (0 \le r \le r_p) \qquad \text{in } \Omega_{ep} \text{ and } \Omega_{en} \qquad (4\text{-}22)$$

$$\frac{\partial c_s}{\partial r} = 0 \qquad \text{at } r = 0 \qquad (4\text{-}23)$$

$$-D_s\frac{\partial c_s}{\partial r} = \frac{v_{Li\theta} a_v i_{loc}}{nF}\frac{r_p}{3\varepsilon_s} \qquad \text{at } r = r_p \qquad (4\text{-}24)$$

in which D_s is the diffusion coefficient of lithium in the solid particle state, r_p is the radius of the LMO particle in the electrode, and $v_{Li\theta}$ is the stoichiometric coefficient of the reduction equation of lithium in the solid particle phase. The stoichiometric coefficients for lithium species, v_{Li^+} and $v_{Li\theta}$ are derived from the electrochemical equation of the reduction process.

$$Li^+ + \theta + v_{Li^+}e^- \rightleftarrows Li\theta \qquad \text{in } \Omega_{ep} \text{ and } \Omega_{en} \qquad (4\text{-}25)$$

in which θ means an active site of the solid intercalation material. As a

single electron participates in this reduction, it leads $v_{\mathrm{Li}^+} = 1$, while $v_{\mathrm{Li}\theta} = -1$ from the reverse reaction of Eq. (4-25). As the stoichiometric coefficients are defined in the reduction reaction, v_{Li^+} and $v_{\mathrm{Li}\theta}$ are constant throughout the whole simulation domain.

In the fully-blocking anion exchange membrane domain (Ω_m), i_l is defined in slightly different manners compared to the above cases, while $i_s = 0$ as non-conducting material is used in this domain.

$$\mathbf{i}_l = \mathbf{i}_m = -\sigma_m \nabla \varphi_m \qquad \text{in } \Omega_m \qquad (4\text{-}26)$$

in which $\mathbf{i}_m$ is the electrolyte current density in the membrane, σ_m is the electrolyte conductivity in the membrane, and φ_m is the electrolyte potential in the membrane. It is assumed here that the charge transfer is solely done by conduction through the fixed electrolyte (= positive charge, in this case) in this domain, which is the case of the fully blocking anion exchange membrane. The Nernst-Planck equation was not solved in this domain, while the electrolyte current density ($\mathbf{i}_l$) was matched with that solved in the adjacent domain.

In the numerical simulation, proper initial and boundary conditions for the constant-current operation were introduced for the ELR system, as below.

Initial conditions

$\varphi_l = 0,\ \varphi_s = E_{eq}(c_s),\ c_s = \mathrm{soc}_{0,\mathrm{int}} \cdot c_{s,\max}$	$0 \le x \le L_e$	(4-27)
$\varphi_l = 0,\ \varphi_s = 0$	$L_e < x < L_{tot} - L_e$	(4-28)
$\varphi_l = 0,\ \varphi_s = E_{eq}(c_s),\ c_s = \mathrm{soc}_{0,\mathrm{dei}} \cdot c_{s,\max}$	$L_{tot} - L_e < x < L_{tot}$	(4-29)
$c_i = 0$	$L_e + L_s < x < L_e + L_s + L_m$	(4-30)
$c_i = c_{i,0}$	otherwise	(4-31)

in which $L_{tot} = L_e + L_s + L_m + L_s + L_e$ where the outer boundary of the negative electrode.

Boundary conditions

$\mathbf{n} \cdot \mathbf{N}_\mathrm{i} = \mathbf{0},\ \mathbf{i}_l = 0,\ \mathbf{i}_s = \mathbf{I}_{cell},\ \varphi_l = 0$	$x = 0$	(4-32)
$\mathbf{n} \cdot \mathbf{N}_\mathrm{i} = \mathbf{0},\ \mathbf{i}_l = 0,\ \mathbf{i}_s = \mathbf{I}_{cell}$	$x = L_{tot}$	(4-33)
$\mathbf{n} \cdot \mathbf{N}_\mathrm{i} = \mathbf{0},\ \mathbf{n} \cdot \mathbf{i}_l = 0,\ \mathbf{n} \cdot \mathbf{i}_s = 0$	at the obstacle surface	(4-34)
$\mathbf{n} \cdot \mathbf{N}_\mathrm{i} = \mathbf{0},\ \mathbf{n} \cdot \mathbf{i}_l = 0,\ \mathbf{n} \cdot \mathbf{i}_s = 0$	$x = L_e + L_s$ or $x = L_e + L_s + L_m$	(4-35)
$\varphi_l - \varphi_m = \frac{RT}{z_{\mathrm{Cl}^-} F} \ln\left(\frac{c_{\mathrm{Cl}^-}}{c_{m,\mathrm{Cl}^-}}\right)$	$x = L_e + L_s$ or $x = L_e + L_s + L_m$	(4-36)
$c_i = c_{i,0}$	at the inlet of the separator	(4-37)
$\mathbf{n} \cdot D_i \nabla c_i = 0$	at the outlet of the separator	(4-38)

in which c_{m,Cl^-} is the concentration of the Cl^- ion fixed in the anion exchange membrane.

Table 4-1 summarizes the parameters used in the simulation. Although the values of most parameters are taken from our measurement or previous studies, those of several parameters have to be assumed to acquire reasonable numerical solutions.

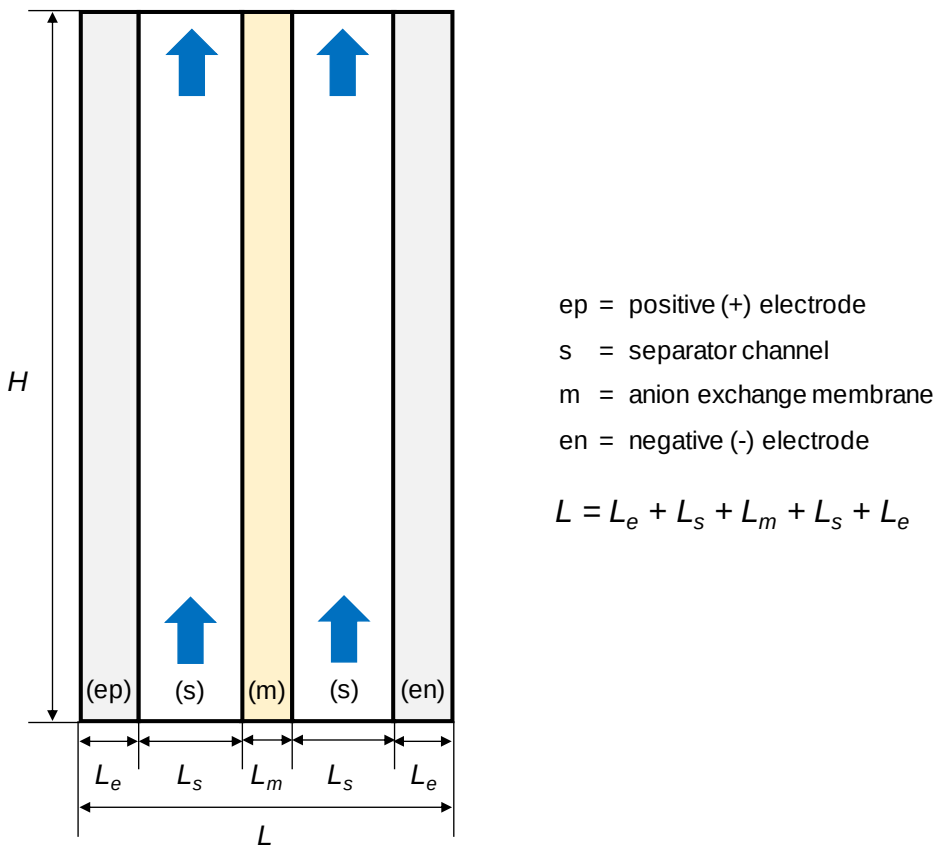

Figure 4-4 Simulation domain of flow-type rocking-chair ELR system. Rectangular spacer meshes are inserted into separator channel to mimic net-type mesh filter used in experiment. Blue arrows indicate flow direction.

Table 4-1 List of parameters used in simulation

Parameter	Description	Value	Reference
L_e	Thickness of electrode [m]	4×10^{-5}	b
L_s	Thickness of separator channel [m]	2×10^{-4}	b
L_m	Thickness of AEM [m]	1×10^{-4}	b
H	Height of electrode (= length of spacer channel) [m]	2×10^{-2}	b
a_v	Active specific surface area of electrode [m^{-1}]	5×10^{6}	(Romero et al. 2018)
D_{Li^+}	Diffusion coefficient of Li^+ [m^2 s^{-1}]	9.9×10^{-10}	(Turq et al. 1969)
D_s	Diffusion coefficient of lithium in solid particle phase [m^2 s^{-1}]	6×10^{-14}	(Marchini et al. 2016)
D_{Cl^-}	Diffusion coefficient of Cl^- [m^2 s^{-1}]	2.0×10^{-9}	(Turq et al. 1969)
$\varepsilon_{l,e}$	Volume fraction of liquid phase in electrode [-]	0.53	a
$\varepsilon_{s,e}$	Volume fraction of solid phase in electrode [-]	0.3	a
$\varepsilon_{i,e}$	Volume fraction of inert phase in electrode [-]	0.17	a
$\varepsilon_{l,s}$	Volume fraction of liquid phase in separator channel [-]	1	a

$c_{Li^+,0}$	Initial concentration of Li^+ in separator channel [mol m^{-3}]	30	b
$c_{Cl^-,0}$	Initial concentration of Cl^- in separator channel [mol m^{-3}]	30	b
$c_{Li^+,\mathrm{ref}}$	Reference concentration of Li^+ in liquid phase [mol m^{-3}]	1	(Romero et al. 2018)
$c_{s,\max}$	Maximum concentration of lithium in solid particle phase [mol m^{-3}]	22,860	b
c_m	Concentration of fixed positive charge in AEM [mol m^{-3}]	1000	a
$\mathrm{soc}_{0,\mathrm{int}}$	Initial electrode state-of-charge in electrode of intercalation [-]	0.001	a
$\mathrm{soc}_{0,\mathrm{dei}}$	Initial electrode state-of-charge in electrode of de-intercalation [-]	0.999	a
$\Delta\mathrm{soc}$	Allowed change in state-of-charge in electrode [-]	0.998	a
σ_s	Conductivity of solid phase in electrode [S m^{-1}]	3.8	c
σ_m	Electrolyte conductivity in AEM [S m^{-1}]	1	(COMSOL Inc. 2012)
r_p	Radius of LMO particle in electrode [m]	1.8×10^{-5}	a
k_a	Anodic reaction rate constant in	1×10^{-11}	(Romero et al. 2018)

	electrode [m s^{-1}]		
k_c	Cathodic reaction rate constant in electrode [m s^{-1}]	1×10^{-11}	(Romero et al. 2018)
α_a	Anodic reaction rate coefficient in electrode [-]	0.5	(Fuller 1994)
α_c	Cathodic reaction rate coefficient in electrode [-]	0.5	(Fuller 1994)
T	Temperature of system [K]	298.15	a
ρ_f	Density of working fluid [kg m^{-3}]	1000	a
η_f	Viscosity of working fluid [Pa·s]	0.001	a

a: assumed, b: measured, c: calculated.

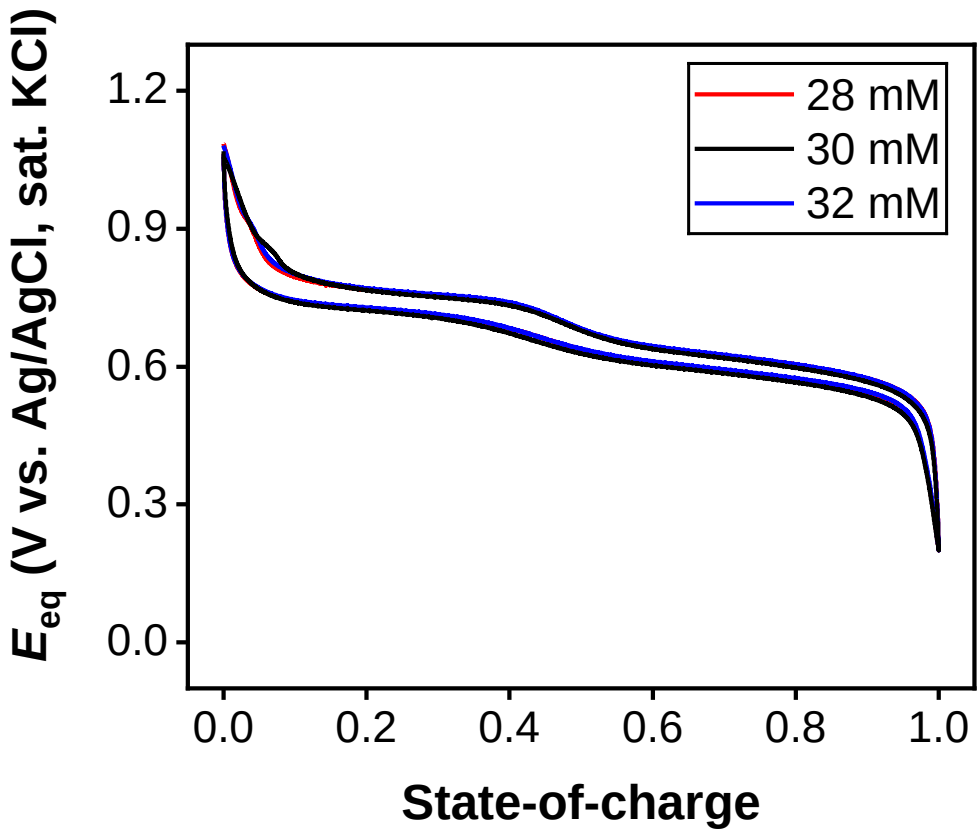

Figure 4-5 Change of the equilibrium potential (E_{eq}) of λ-MnO_2 ($LiMn_2O_4$) over State-of-charge. Measurement was conducted by galvanostatic discharge/charge test using 3-electrode cell (working: λ-MnO_2, counter: $LiMn_2O_4$, and reference: Ag/AgCl/KCl saturated) at 2.50×10^{-1} mA cm^{-2}. 28, 30, and 32 mM LiCl aqueous solution was used as electrolyte. This figure shows the equilibrium potentials of λ-MnO_2 ($LiMn_2O_4$) electrode as LiCl aqueous solution varied from 28 to 32 mM. The equilibrium potential shift appeared to be negligible in this range of concentration. The dependence of the equilibrium potential on the lithium ion concentration was excluded in the model.

4.3.2 Simulation details

A commercial software, COMSOL Multiphysics 5.4 (COMSOL inc., USA), was used in our simulation, based on the finite element method (FEM). For the details of the implementation of the intercalation model with the mass balance equation, a previous work by Romero et al. was referred (Romero et al. 2018). Four interconnected multiphysics modules were coupled and numerically solved using this software—the tertiary current distribution (tcdee) module for the whole system, the lithium-ion battery (liion) module for the two electrodes, the secondary current distribution (siec) module for the AEM, and the laminar flow (spf) module for the spacer channel. The two-dimensional simulation domain was prepared and discretized with 89,643 rectangular-shaped mapped meshes (see **Figure 4-6** for the mesh convergence test). The finer mesh elements were generated in the separator domain (Ω_s) near the interfaces with electrodes (Ω_e) or the AEM (Ω_m) to accurately calculate the boundary concentration. A workstation with two octa-core processors (Intel(R) Xeon(R) CPUs E5-2687W 3.1 GHz) and 192 GB memory was used in the numerical calculation. A stationary flow field was obtained first, and it is expected that it will remain constant throughout the simulation. Thereafter, the time-dependent mass balance equations coupled

with electrochemical reactions and the treatment of the AEM were solved. A direct solver named PARDISO was utilized both in the flow and in the mass transfer problem, whereas an implicit time-stepping method, the backward differentiation formula (BDF), was used to solve this time-dependent mass transfer problem.

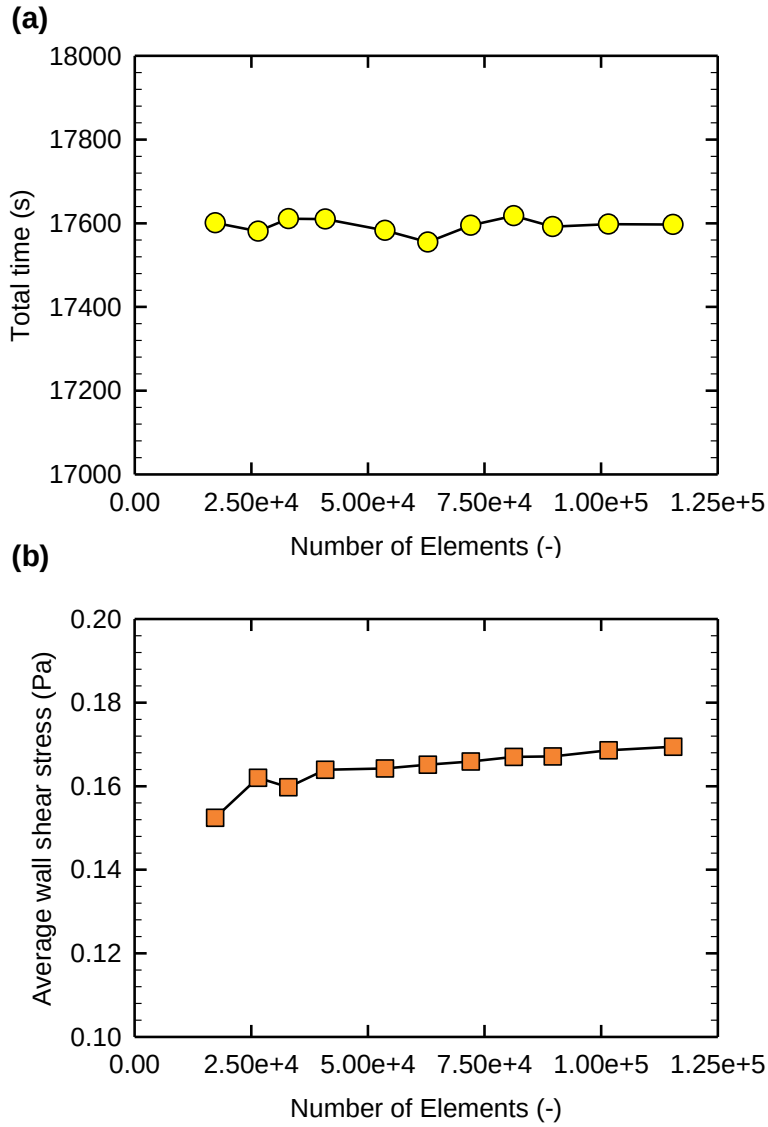

Figure 4-6 Mesh convergence test with (a) the total time and (b) the average wall shear stress on the positive electrode. It is revealed that refined computational mesh is needed to obtain average wall shear stress, however, the total time of the system operation (i.e., the time to reach to the limitation of voltage) is insensitive to the number of elements. It was determined that 89,643 rectangular meshes are enough to be used in our simulation.

4.4. Results and discussion

4.4.1 Electrochemical lithium recovery using λ-MnO_2/$LiMn_2O_4$ system

Figure 4-7a shows the concentration changes of the effluent during the operation of the ELR system. Both in step 1 and in step 2, the concentration of the effluent from the catholyte channel (red line of step 1 and blue line of step 2) decreases and the conductivity of the effluent from the anolyte channel (blue line of step 1 and red line of step 2) increases. The trend in the concentration changes is found to be symmetric in each channel and in each step. The behavior of this system can also be understood from the state-of-charge (SoC) profile of the electrodes calculated using numerical simulation, as shown in **Figure 4-7b**. The SoC of the cathode increases because of the intercalation reaction of Li^+ (red line of step 1 and blue line of step 2) and the SoC of the anode decreases because of the de-intercalation reaction of Li^+ (blue line of step 1 and red line of step 2). Similar to the trend in the conductivity changes, the increasing and decreasing trends in the SoC are identified to be symmetric in each channel and in each step shown in **Figure 4-7b**. These trends observed in the conductivity and SoC confirm that electrodes intercalated and de-intercalated Li^+ symmetrically and reversibly.

Figure 4-7c and **Figure 4-7d** show the cell voltage profiles with respect

to time in steps 1 and 2, respectively. The cell voltage decreases with time in step 1 and increases with time in step 2. Each cell voltage profile represents two plateaus from 0.1 to 0.3 V and –0.3 to –0.1 V, where Li^+ intercalation and de-intercalation occur simultaneously. This range corresponds with the potential difference of reduction/oxidation peak from the cyclic voltammogram (see **Figure 4-3a**) and the potential difference of plateaus presented in the galvanostatic charge/discharge curve (see **Figure 4-3b**). As the current increases, the time required to reach the voltage limit decreases, which indicates that the overall reaction time was shortened. Under all current conditions, the profile calculated in the numerical simulation fits well with the profile obtained from the experiment, indicating that our simulation reproduced well the kinetics and equilibrium of reaction of our ELR system under constant-current operation. The two cell voltage profiles are nearly symmetrical on the *x*-axis, which also indicates that our ELR system was operated reversibly and symmetrically.

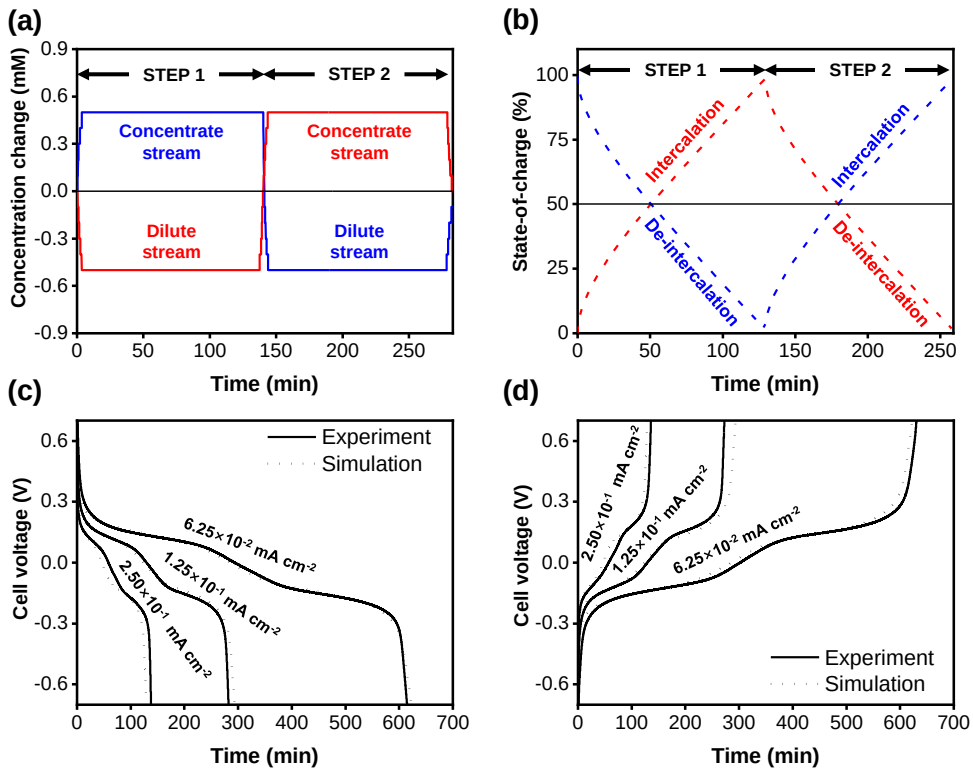

Figure 4-7 (a) The concentration changes of effluents from experiment and (b) state-of-charge (SoC) of $LiMn_2O_4$ electrode from simulation when 2.50×10^{-1} mA cm^{-2} current density is imposed. Red/blue lines represent left/right side of the reactor. Cell voltage profiles with respect to time during (c) step 1 and (d) step 2. Solid/dashed lines represent results from experiment/simulation. Current values used in experiment and simulation were 6.25×10^{-2}, 1.25×10^{-1}, and 2.50×10^{-1} mA cm^{-2}.

4.4.2 Concentration distribution of Li^+ in 2D domain with spacer mesh

Figure 4-8 depicts the concentration distribution of Li^+ over time and space. The spatiotemporal concentration distribution is indicated at three representative times and in the three representative regions (**Figure 4-8a**). As depicted in panels (i) to (ix), the shape of the concentration contour around the spacer mesh is closely related to the velocity profile affected by the presence of the spacer mesh (see **Figure 4-9**). It facilitates mass transfer perpendicular to the electrode, whereas the dominant convective mass transfer is induced by the pressure-driven flow in the separator channel along the flow direction. As our electrochemical system was operated in the constant-current mode, the resulting concentration distribution at each separator channel and electrode was immediately obtained at an early stage of the process. It is apparent that an almost identical concentration distribution was maintained right after the initiation of the process (i.e., the concentration distributions obtained at SoC = 50% and SoC = 100% are almost identical). The difference in c_{Li^+} between the two separator channels increases when one proceeds from region A to region C because Li^+ is diluted or concentrated along the flow direction as Li^+ is captured by or released from each electrode.

Figure 4-8b shows the temporal change in c_{Li^+} with normalized

horizontal coordinate (x/L) at the center of the channel ($y = H/2$). Before applying the current, c_{Li^+} in the entire simulation domain except in the AEM is constant (= 30 mM). When the current is applied, c_{Li^+} of the catholyte channel decreases with time and c_{Li^+} of the anolyte channel increases with time. After 10 seconds, the profile of c_{Li^+} is rapidly developed and is maintained until the end of the process. Three distinctive regions are defined for the discussion of the horizontal concentration distribution, as below. Regions 1 and 2 are specified by the interface of the porous electrode and the separator channel, whereas regions 2 and 3 are specified by the maximum/minimum points of the concentration profile when the SoC = 100%. In region 1, Li^+ is intercalated into the porous LMO in the positive electrode and de-intercalated from the porous LMO in the negative electrode, which leads to a decrease in the concentration of Li^+ in the positive electrode and an increase in the concentration of Li^+ in the negative electrode. c_{Li^+} is maintained constant after 10 seconds (29.6 to 29.7 on the cathode side and 30.4 to 30.3 on the anode side) because the balance in the charge transfer and mass transfer rates is rapidly obtained under constant-current operation. In regions 2 and 3, a parabolic shape of the c_{Li^+} profile is developed because the mass transfer of Li^+ through the AEM is prohibited, resulting in the dilution

of Li^+ in region 3 of the catholyte channel and the accumulation of Li^+ in region 3 of the anolyte channel. The change in concentration at the edge of region 3 is greater than that at the edge of region 2 because Li^+ in region 3 is transferred to region 2 (catholyte channel) and from the region 2 (anolyte channel), alleviating the change in concentration in region 2.

Figure 4-8c illustrates the temporal change in c_{Li^+} with normalized vertical length (y/H) at the surface of the positive electrode ($x = L_e$). When the current is applied, c_{Li^+} decreases rapidly in less than 2 seconds, resulting in a nearly linear profile. It is because the intercalation reaction of Li^+ occurs at a constant rate throughout the reactor under the constant-current operation. The profile of c_{Li^+} maintains its shape after 10 seconds till the end of the process because Li^+ is intercalated into the electrode at a constant rate as it passes through the separator channel. It should be noted here that the concentration polarization is reduced by the introduction of a spacer mesh (see **Figure 4-10**). Compared to the concentration distribution in a plane separator channel, a flat concentration distribution is induced with the spacer mesh in the separator channel, indicating that the concentration polarization is alleviated.

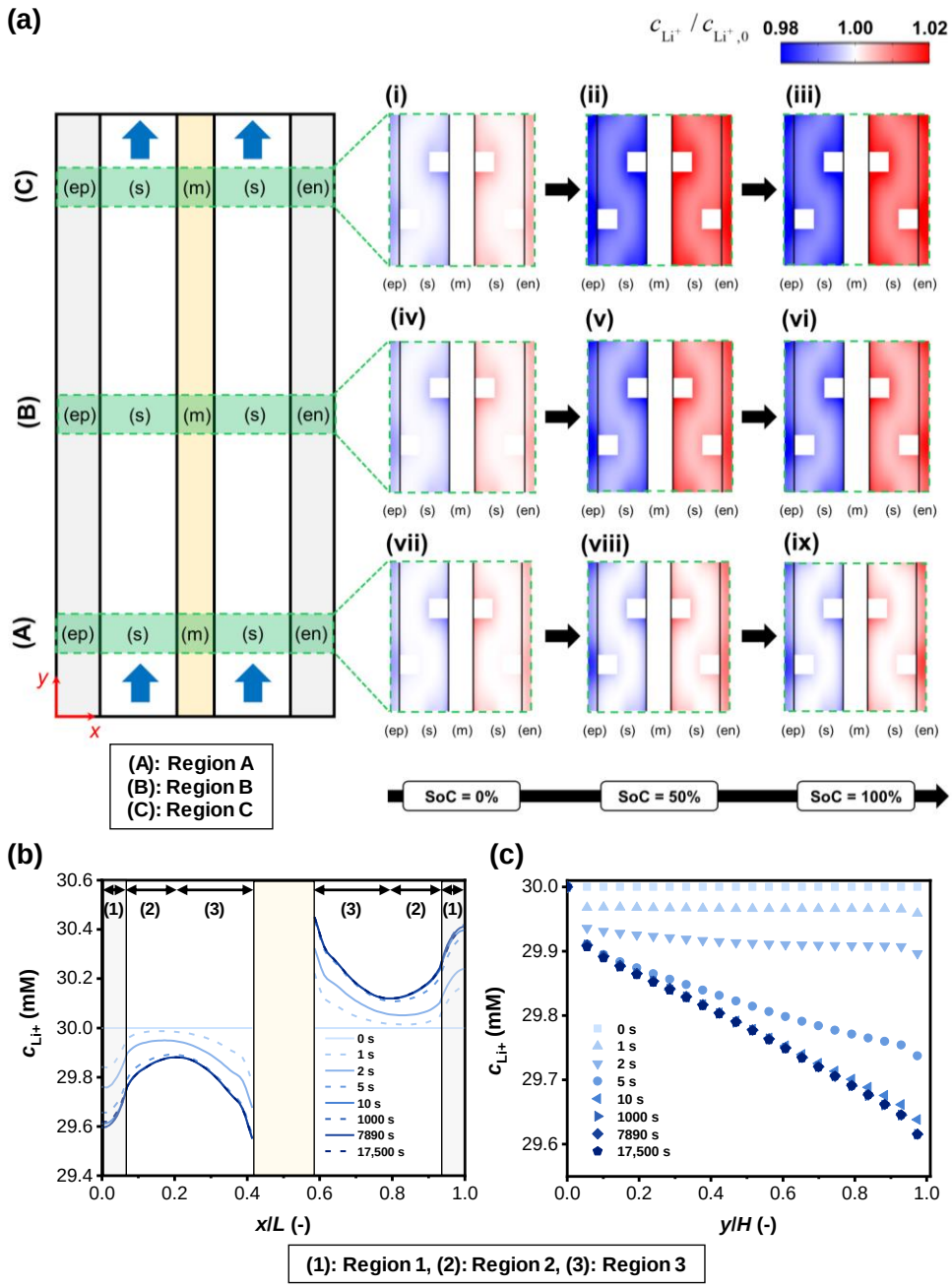

Figure 4-8 (a) Concentration distribution of Li^+ in three representative regions (A: initial, B: central, C: terminal) at three representative times (SoC = 0%, 50%, and

100% at step 1), i.e., concentration distribution in each separator channel and electrode is changed from (i) to (iii) in terminal region (region C). Color of region indicates Li^+ concentration (c_{Li^+}). Compared to inlet Li^+ concentration ($c_{Li^+,0}$, 30 mM), it is blue when $c_{Li^+} < c_{Li^+,0}$, whereas it is red when $c_{Li^+} > c_{Li^+,0}$. (b) Temporal change in c_{Li^+} with normalized horizontal coordinate (x/L) at the center of channel ($y = H/2$) when the current is imposed at 1.25×10^{-1} mA cm^{-2}. Region 1 denotes porous electrode, region 2 corresponds to separator channel adjacent to electrode, and region 3 corresponds to separator channel adjacent to AEM. (c) Temporal change in c_{Li^+} with normalized vertical coordinate (y/H) at surface of positive electrode ($x = L_e$) when current of 1.25×10^{-1} mA cm^{-2} is imposed at channel in step 1. To clearly illustrate temporal change in c_{Li^+}, concentration values in middle of two adjoint spacer meshes are exhibited in this figure.

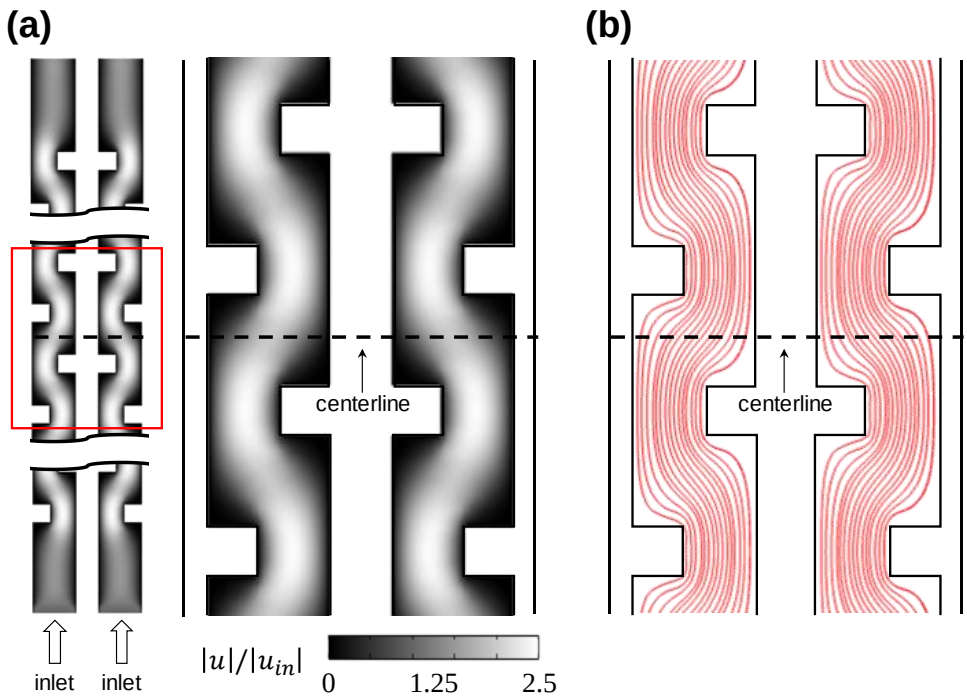

Figure 4-9 (a) Velocity contour plot of the flow in the system at the central region and (b) velocity contour line plot of the flow in the system. Flow rate was 1 ml/min for each channel. This figure shows the velocity contour plots of the flow in the separator channel filled with spacer meshes. The zigzag configuration of the spacer meshes has two main effects on the flow. First, the flow rate is increased up to 2.5 times the inlet flow rate as shown in (a**)**. The feed solution in contact with the electrode is renewed quickly compared to the absence of the spacer mesh and it is advantageous for mass transport of Li^+. Secondly, the vertical flow direction is altered by the presence of spacer meshes as shown in (b), which is beneficial for the mass transfer in the separator channel.

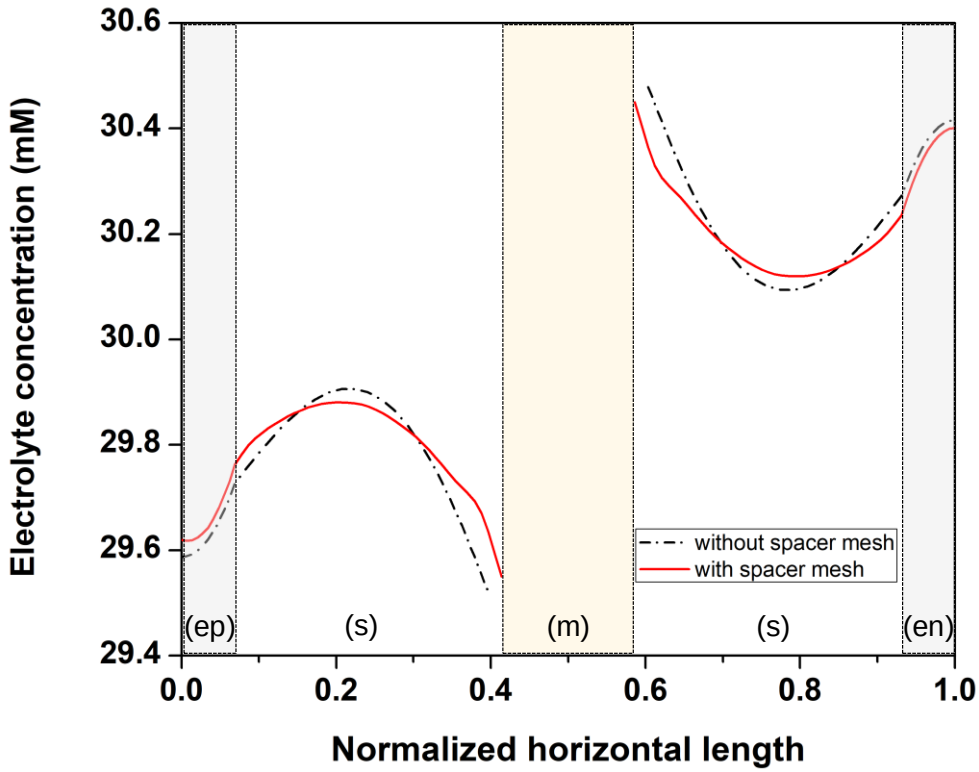

Figure 4-10 Electrolyte concentration profile with normalized horizontal length at the center of the system with (red solid line) and without spacer (black dash dot line) mesh at the step 1 (representative current: 0.5 mA). This figure shows the electrolyte concentration profile with and without spacer mesh in the cross-section perpendicular to the flow direction. In both cases, the shape of the profiles is parabola, indicating concentration polarization in the separator channel. In the presence of the spacer mesh, the difference between the maximum and minimum concentration is smaller than in the absence of the spacer mesh. In other words, the concentration polarization can be alleviated by the spacer mesh in the flow-type electrochemical ELR system.

4.4.3 Performance of λ-MnO_2/$LiMn_2O_4$ system from experiment and simulation

Table 4-2 summarizes the experimental values, simulation values, and errors in specific capacity (Q, mAh g^{-1}) and specific mass of Li^+ recovered at the LMO electrode (q_{Li^+}, mg g^{-1}) under three current density conditions. Q is the amount of specific charge used to recover Li^+ and q_{Li^+} is the amount of Li^+ recovered per electrode mass. Both values of Q, from the experiment and the simulation, decrease as the current is increased. This can be attributed to the fact that the available capacity reduces with the current as the Ohmic drop increases with the current. A similar trend is also observed in the case of q_{Li^+}. As the current increases, q_{Li^+} decreases because the number of electrons available for the electrochemical reaction decreases. When the simulation result is compared to the experimental one, the error in Q is 0.8% to 7.0% and the error in q_{Li^+} is 2.9% to 16.7%, indicating an increase in the error with the current, because our simulation does not consider the concentration overpotential caused by the mass transfer limitation (Tang et al. 2014). On the other hand, the error in q_{Li^+} is larger than that in Q for all cases because q_{Li^+} is more impacted by the concentration overpotential compared to Q.

Table 4-2 Effect of current density on specific capacity and specific mass of Li^+ recovered (a: Experiment, b: Simulation)

Current density ($mA\ cm^{-2}$)	6.25×10^{-2}			1.25×10^{-1}			2.50×10^{-1}		
Data classification	Exp.[a]	Sim.[b]	Error (%)	Exp.	Sim.	Error (%)	Exp.	Sim.	Error (%)
Q ($mAh\ g^{-1}$)	128	129	0.8	117	122	4.3	115	107	7.0
q_{Li^+} ($mg\ g^{-1}$)	35	34	2.9	28	32	14.3	24	28	16.7

Figure 4-11a exhibits the cell voltage profile at steps 1 and 2 and it is used in the calculation of energy recovery and consumption. The energy recovery/consumption of our system during time t is represented as the product of the area covered by the graph and the current (Eq. (4-3)). The blue area in the graph (W_r) indicates the amount of energy recovered in step 1 (discharging step) and the red area in the graph (W_c) indicates the amount of energy consumed in step 2 (charging step). The total energy consumption of our rocking-chair ELR system could be minimized through an efficient energy recovery method; for example, by connecting a supercapacitor to the electrochemical cell, the energy in the blue region (= the amount of energy recovery) can be stored in the supercapacitor at the discharging step. Here, one can refer to a recently developed technology for efficient energy recovery using a supercapacitor connected to a buck-boost converter (Kang et al. 2016). **Figure 4-11b** depicts the specific total energy consumption per mole of recovered Li^+ (W_{total}) without and with energy recovery according to three current conditions (Eq. (4-4) and (4-5)). By applying at 6.25×10^{-2}, 1.25×10^{-1}, and 2.50×10^{-1} mA cm^{-2} of current density, the total energy consumption is measured as 2.3, 2.7, and 5.4 Wh mol^{-1}, respectively, without energy recovery and as 0.56, 0.88, and 1.95 Wh mol^{-1}, respectively, with energy recovery. In previous studies on the ELR system, W_{total} is in the range 1.0 – 8.7 Wh mol^{-1}

(Pasta et al. 2012; Lee et al. 2013; Trócoli et al. 2014, 2015, 2017; Kim et al. 2015b, 2018b; Lawagon et al. 2018; Zhao et al. 2019) and 17.98 Wh mol^{-1} for the $LiMn_2O_4/Li_{1-x}Mn_2O_4$ system operated in the constant-voltage mode (Zhao et al. 2017) (note that the electrolyte conditions, which are closely related to the energy consumption, were different in the studies). Regardless of energy recovery, the total energy consumption tends to increase with increasing current. It is because a large overpotential is driven by the large Ohmic drop and the number of electrons available for the electrochemical reaction decreases as the current increases (see **Table 4-2**).

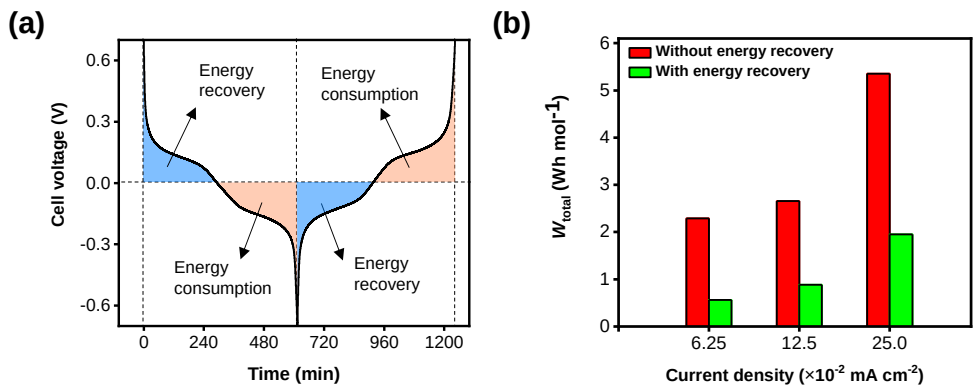

Figure 4-11 (a) Cell voltage profile with time during steps 1 and 2 for calculation of amount of energy recovery (blue) and energy consumption (orange) and (b) the specific total energy consumption per mole of recovered Li^+ (W_{total}) during a step without (red) and with energy recovery (green).

4.5. Summary

In this study, a flow-type λ-MnO_2/$LiMn_2O_4$ system was suggested and two-dimensional numerical simulations were performed to analyze the ionic behavior occurring in the flow channels. Reversible and symmetrical system behavior was confirmed in our system by experimentally measuring the conductivity, SoC, and cell voltage profile. The concentration distribution of Li^+ in our electrochemical reactor was obtained through numerical simulation by considering the flow behavior in the separator channel filled with a net-type spacer mesh. In the constant-current mode, the Li^+ concentration profile shows a parabolic shape along the horizontal direction and a linear shape along the vertical direction, implying the development of concentration polarization in this system. The performance of the system was evaluated using three parameters—specific capacity, the specific mass of Li^+ recovered, and total energy consumption. At 6.25×10^{-2} mA cm^{-2}, the specific capacity is 128 mAh g^{-1}, the specific mass of recovered Li^+ is 35 mg g^{-1}, and the total energy consumption with energy recovery is 0.56 Wh mol^{-1}. It was confirmed, both by electrochemical experiment and numerical simulation, that a stable recovery of lithium can be conducted through our flow-type rocking-chair ELR system. The system can be further improved by gaining an in-depth

understanding of the system behavior through the two-dimensional simulations conducted in this study, showing well-fitted system performance with the experimental results.

5. Electrode design and performance of flow-type electrochemical lithium recovery (ELR) systems

5.1. Introduction

As the climate crisis becomes a reality, technologies to attain carbon-neutrality are attracting ever increasing attention (Chen 2021). Since electricity can be produced and consumed with low carbon footprint and allow diversification of energy supply and storage, electric vehicle (EV) and energy storage system (ESS) have been being extensively studied in the last decade (Ghosh 2020; Agudosi et al. 2021; How et al. 2022), where battery is a key component. As the global markets for EV and ESS grow rapidly, the demand for lithium is expected to soar since the manufacturing of EVs and ESS requires a tremendous amount of batteries (Liu et al. 2019). Traditionally, lime soda evaporation has been used for the mass production of lithium compounds, which recovers lithium from aqueous sources (Xu et al. 2016; Fukuda and Eng 2019). However, the increasing demand for lithium compounds cannot be matched by this process alone, since it is a slow process involving the time-consuming evaporation step (over a year). Additional supply is also required to alleviate the increasing trend of lithium price, which is expected to persist in the future (Sun et al. 2017; Martin et al. 2017;

Calisaya-Azpilcueta et al. 2020; Tang et al. 2021). In addition, lime soda evaporation is not an attractive process from the sustainability point of view, as it produces some highly concentrated chemicals with negative environmental impacts (Xu et al. 2016, 2021). Thus, a sustainable alternative is required to address these issues.

Electrochemical lithium recovery (ELR) technology has been studied in recent years (Yoon et al. 2019; Calvo 2019; Battistel et al. 2020) to secure more sustainable production of lithium resources. Since the ELR system uses electricity to recover lithium compounds, its production rate can be easily controlled by the constant-current mode operation and no environmental pollutants are generated (Srimuk et al. 2020; Calvo 2021). Previous studies on the ELR system have mainly focused on improving the performance by material engineering or optimization of the operation conditions (Joo et al. 2020a). Starting with the first ELR system (λ-MnO_2/platinum system (Kanoh et al. 1993)), the $LiFePO_4$/silver (Pasta et al. 2012), and λ-MnO_2/silver (Lee et al. 2013) battery systems with the lithium-ion battery (LIB) cathode materials were proposed. Also, the electrochemical properties of the cathode material were improved by synthesizing the cathode materials in a different morphology (Xu et al. 2018; Xie et al. 2020), coating it with a polymer material (Kim et al. 2015a; Du et al. 2016; Zhao et al. 2020b, a; Niu et al.

2021; Fang et al. 2022), or doping other transition metals (Lawagon et al. 2018, 2019; Zhao et al. 2020c; Shang et al. 2021). Besides, some inexpensive anode materials with moderate performance (e.g., NiHCF (Trócoli et al. 2015, 2017), activated carbon (Kim et al. 2015b; Jang et al. 2021), polypyrrole (Missoni et al. 2016), zinc (Kim et al. 2018b), cathodic material (Liu et al. 2014; Zhao et al. 2017)) have been also investigated to replace the silver electrode.

Various analysis studies have been also applied for a deeper understanding of the characteristics and the operating principles of the ELR system. The chemical changes occurring on the cathode surface during lithium recovery were analyzed using X-ray measurement (Marchini et al. 2016, 2018a), and the causes of system degradation were investigated using electrochemical analysis (Marchini et al. 2018b; Guo et al. 2020; Wang et al. 2021). Several numerical studies have also been performed to understand the underlying system mechanisms of the ELR system (Romero et al. 2018, 2020, 2021b), and a similar system, battery (West et al. 1982) and capacitive deionization with intercalation materials (Smith and Dmello 2016; Singh et al. 2018). In previous study, a pseudo-two-dimensional (P2D) model was developed for a rocking chair ELR system with flow-channels, which was able to explain the experimental results very well (Joo et al. 2020a).

Although extensive studies have been performed in terms of the electrode materials, studies on the design of electrochemical lithium recovery system have been discussed only to a limited extent. A flow-through system was proposed whose system performance was evaluated by changing the flow rate and the electrode mass loading (Palagonia et al. 2017, 2019). In a study discussing the effect of the lithium concentration and current density on lithium recovery capacity, it was found that the recovery capacity is increased when ball-milled particles of cathode material were used instead of the pristine ones (Kim et al. 2020). A study that compared the performance of flow-by and flow-through reactors emphasized the need to increase the specific surface area of the active material of electrode for the higher capacity of the ELR system (Romero et al. 2021a). These studies found that the lithium recovery performance is significantly dependent on several design parameters such as flow rate, electrode mass loading, lithium concentration, current density, and specific surface area of the active material. To the best of our knowledge, however, there has been no study to guide the electrode fabrication by systematically analyzing the effect of multiple electrode design parameters on the ELR system performance.

In this study, to this end, a comprehensive numerical study is performed to evaluate the correlations between the electrode design parameters and the

performance of ELR system at a low current density of 62.5 μA/cm^2. Three design parameters (effective radius of lithium manganese oxide (LMO) particle (r_{p}), volume fraction of LMO particles in electrode (ε_{s}), and electrode thickness (δ)) and two performance indicators (specific mass of Li^+ recovered ($q_{\mathrm{Li^+}}$) and net energy consumption (W_{net})) are selected for the parameter study. The validated model from our previous research (Joo et al. 2020a) is adopted, which can simulate a flow-type rocking chair ELR system (λ-MnO_2/$LiMn_2O_4$). Correlations between the design parameters and the performance indicators are identified and explained by the working principles of the system. Sensitivity analysis is conducted to figure out the significance of each design parameter.

Table 5-1 Nomenclature list of symbols used in this section

Roman symbols	
A_{sec}	Cross-sectional area of the electrode [m^2]
c_i	Concentration of *i*th species [mol m^{-3}]
c_{s}	Concentration of lithium in the solid phase [mol m^{-3}]
$c_{\mathrm{s,max}}$	Maximum concentration of lithium in the solid phase [mol m^{-3}]
$c_{\mathrm{s,surface}}$	Concentration of lithium in the solid phase at the surface of LMO particle [mol m^{-3}]
c_{l}	Concentration of lithium in the liquid phase [mol m^{-3}]
$c_{\mathrm{l,ref}}$	Reference concentration of lithium in the liquid phase [mol m^{-3}]
$D_{i,\mathrm{eff}}$	Effective diffusivity of *i*th species in a porous medium [m^2 s^{-1}]
D_{s}	Diffusivity of Li^+ within the LMO particle [m^2 s^{-1}]
ΔE	Cell voltage [V]
E_{eq}	Equilibrium potential [V]
F	Faraday constant [C mol^{-1}]
$\boldsymbol{I}_{\mathrm{cell}}$	Current density within the electrochemical cell [A m^{-2}]
i_0	Exchange current density [A m^{-2}]
$\boldsymbol{i}_{\mathrm{l}}$	Electrolyte current density [A m^{-2}]
i_{loc}	Local current density [A m^{-2}]
$\boldsymbol{i}_{\mathrm{s}}$	Electrode current density [A m^{-2}]
k_{a}	Anodic reaction rate constant [m s^{-1}]
k_{c}	Cathodic reaction rate constant [m s^{-1}]
L_{sep}	Width of the separator channel [m]
L_{m}	Width of the anion exchange membrane [m]
LiΘ	Occupied reaction site
m_{elec}	Mass of the electrode [g]
$m_{\mathrm{Li^+}}$	Molar mass of Li^+ [g mol^{-1}]
n	Number of electrons participating in the reduction equation of Li^+ [-]
$\boldsymbol{N}_i$	Total mass flux of *i*th species [mol m^{-2} s^{-1}]
r_{p}	Effective radius of the active material [μm]
R	Molar gas constant [m^2 kg s^{-2} K^{-1} mol^{-1}]
R_i	Rate of production (or consumption) of *i*th species [mol m^{-3} s^{-1}]
Q	Specific capacity [mAh g^{-1}]
Q_{max}	Maximum specific capacity [mAh g^{-1}]
$q_{\mathrm{Li^+}}$	Specific mass of Li^+ recovered [mg g^{-1}]
$q_{\mathrm{Li^+,max}}$	Theoretical maximum value of $q_{\mathrm{Li^+}}$ [mg g^{-1}]
$\boldsymbol{u}$	Fluid velocity vector [m s^{-1}]
W_{net}	Net energy consumption [Wh mol^{-1}]
$W_{\mathrm{net,ref}}$	Reference energy consumption (=1.0 Wh mol^{-1})
t	Time [s]
t_{f}	Time elapsed until a lithium recovery step is finished [s]
T	Temperature [K]
V_{elec}	Volume of the electrode [m^3]
z_i	Charge number of *i*th species [-]

Greek symbols	
α	Mass fraction of the active material [-]
α_a	Anodic reaction rate coefficient [-]
α_c	Cathodic reaction rate coefficient [-]
δ	Electrode thickness [m]
ε_s	Volume fraction of the active material [-]
ε_l	Volume fraction of the liquid phase [-]
ϕ_l	Electrolyte potential [V]
ϕ_s	Electrode potential [V]
η	Overpotential [V]
Θ	Unoccupied reaction site
$\mu_{i,\mathrm{eff}}$	Effective mobility of *i*th species in a porous medium [s mol kg^{-1}]
v_{Li^+}	Stoichiometric coefficient in the reduction equation of Li^+ [-]
ρ_s	Density of the active material [kg m^{-3}]
$\sigma_{s,\mathrm{eff}}$	Effective conductivity of *i*th species in a porous medium [S m^{-1}]
Ω	Volume element
Ω_{ep}	Positive (λ-MnO_2) electrode domain
Ω_{en}	Negative ($LiMn_2O_4$) electrode domain
Ω_m	Anion exchange membrane domain
Ω_{sep}	Separator channel domain
Abbreviations	
EV	Electric vehicle
ESS	Energy storage system
ELR	Electrochemical lithium recovery
LIB	Lithium-ion battery
LMO	Lithium manganese oxide
SoC	State of charge

5.2. Model development

5.2.1 System description

Figure 5-1 shows the general description of the working principles of the ELR system, the simulation domain, and the electrode design parameters. The flow-type rocking chair ELR system (λ-MnO_2/$LiMn_2O_4$) is illustrated in **Figure 5-1a**. Two $Li_{1-x}Mn_2O_4$ (LMO) electrodes having different lithium-ion (Li^+) concentrations ($x = 1$ for λ-MnO_2 and $x = 0$ for $LiMn_2O_4$) are at both ends. The left electrode is marked as positive (sub-domain: Ω_{ep}), and the right electrode is marked as negative (sub-domain: Ω_{en}). Between the electrodes, there are two flow channels (sub-domain: Ω_{sep}) separated by an anion exchange membrane (AEM, sub-domain: Ω_{m}). AEM prevents the inter-channel mixing of the electrolytes and allows only anions to be transported. The thicknesses of electrodes, flow channels, and AEM are denoted by δ, L_{sep}, L_{m}, respectively. The area of each sub-domain in the depth direction is 4 cm^2 (2 cm × 2 cm).

The whole process operated by the rocking chair ELR system was divided into two steps (Step 1 and Step 2) based on the direction of the current. Specifically, a negative current was applied to the cell in Step 1, and a positive

current was applied to the cell in Step 2. In Step 1, a constant current was applied to the cell. Note that this simulation was performed under low current conditions to exclude the effect of concentration polarization, which readily occurs in low concentration electrolytes, and to observe the effect of the design parameters on the ELR system performance only. Li^+ in the electrolyte was captured into the LMO by the intercalation reaction at the interface between Ω_{ep} and Ω_{sep}, while it was released to the electrolyte by the de-intercalation reaction at the interface between Ω_{en} and Ω_{sep}. The intercalation and de-intercalation reactions can be written as follows:

$$\text{Reduction:}\quad Li^+ + 2\lambda - MnO_2 + e^- \rightarrow LiMn_2O_4 \tag{5-1}$$

$$\text{Oxidation:}\quad LiMn_2O_4 \rightarrow Li^+ + 2\lambda - MnO_2 + e^- \tag{5-2}$$

To balance the charge neutrality, chloride anions (Cl^-) move from the Ω_{ep} side flow channel to the Ω_{en} side flow channel through the AEM. As a result of the transport of Li^+ and Cl^-, the LiCl concentration decreases at the Ω_{ep} side and increases at the Ω_{en} side. At the same time, Li^+ diffuses into or out of the LMO particles, causing a change in solid-phase concentration, whose reaction formula takes the following form:

$$Li^+ + \Theta \rightleftharpoons Li\Theta \tag{5-3}$$

where Θ is an unoccupied reaction site and $Li\Theta$ is an occupied reaction site.

In summary, the movement of Li^+ from the electrolyte to LMO particle is divided into three stages: mass transport (diffusion and convection) in the electrolyte, intercalation/de-intercalation reactions at the electrolyte-solid interface, and mass transport (diffusion) in the solid phase particles. This movement of Li^+ changes the electric potential of the electrodes and electrolytes. The electric potential difference between the positive and negative electrodes measured at both ends is termed cell voltage. The specific changes in Li^+ concentration and electric potential with time are covered in detail in Section 5.2.5. A similar series of phenomena takes place in Step 2, however in an opposite direction.

Figure 5-1b shows three-electrode design parameters adopted in this study. The first parameter is the effective radius of the LMO particles (r_{p}). Although r_{p} has distribution in practice, for the numerical simulations, it is advantageous to specify an apparent value of r_{p}. As r_{p} increases, the diffusion length in the solid phase becomes longer. The second parameter is the volume fraction of LMO particles in the electrodes (ε_{s}), which represents the volume ratio of active material to a porous electrode. As ε_{s} increases, the density of electrodes increases even for electrodes with the same thickness. The third parameter is the electrode thickness (δ) which corresponds to the length of sub-domain Ω_{ep} or Ω_{en}. When δ increases while other electrode design

parameters are fixed, the mass of the active material increases proportionally to δ. In the following simulation, the effect of these design parameters on the performance of the ELR system is discussed.

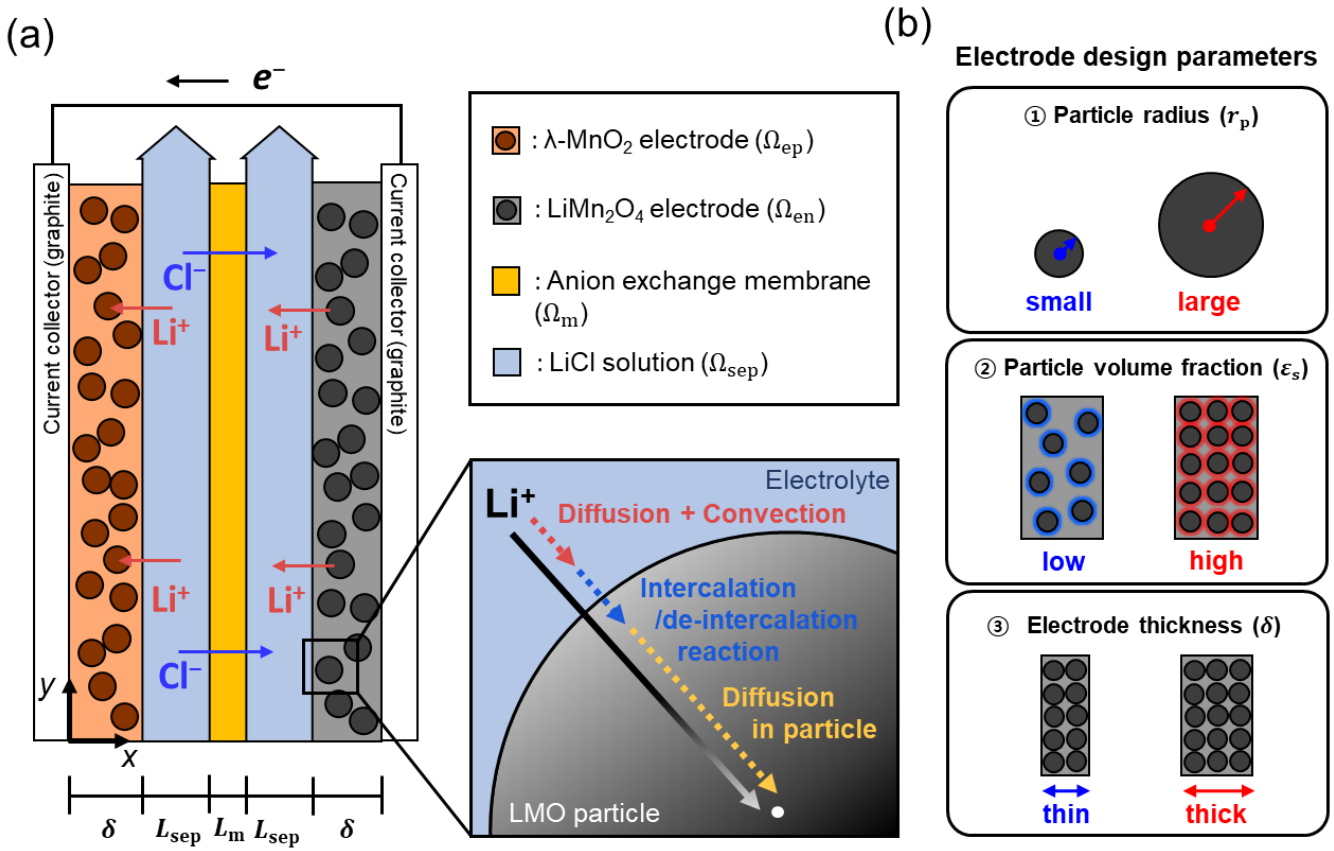

Figure 5-1 (a) Schematic diagram and simulation domain of the λ-MnO_2/$LiMn_2O_4$ ELR system and (b) electrode design parameters

5.2.2 Numerical simulation

To describe a flow-type ELR system with LMO electrodes, a pseudo two-dimensional (P2D) model was developed in previous study (Joo et al. 2020a). Since the model has been verified to successfully reproduce the temporal change in the cell voltage curve, the electrolyte concentration, and the concentration of recovered lithium in the solid phase, it is decided to utilize this model to perform a parameter study by changing several electrode design parameters. In this model, the simulation domain is composed of 4 sub-domains as described above (see **Figure 5-1a**). A 30 mM LiCl solution is injected at the inlet of the separator channels (at $y = 0$ in Ω_{sep}) at 1 mL/min. As Li^+ is intercalated into the positive electrode, the concentration of Li^+ in the left separator channel decreases. At the same time, Li^+ is de-intercalated from the negative electrode, and thus the concentration of Li^+ in the right separator channel increases.

Considering the charge neutrality in the system, the mass transfer of *i*th species (i = Li^+, Cl^-) in the electrochemical system is described by the mass conservation equation and the Nernst-Planck equation:

$$\varepsilon_l \frac{\partial c_i}{\partial t} + \nabla \cdot \boldsymbol{N}_i = R_i, \quad \text{in } \Omega_{\mathrm{ep}}, \Omega_{\mathrm{en}}, \text{and } \Omega_{\mathrm{sep}} \qquad (5\text{-}4)$$

$$\boldsymbol{N}_i = -D_{i,\mathrm{eff}} \nabla c_i - z_i \mu_{i,\mathrm{eff}} F c_i \nabla \phi_l + \boldsymbol{u} c_i, \quad \text{in } \Omega_{\mathrm{ep}}, \Omega_{\mathrm{en}}, \text{and } \Omega_{\mathrm{sep}} \qquad (5\text{-}5)$$

$$\sum_i z_i c_i = 0, \quad \text{in } \Omega_{\text{ep}}, \Omega_{\text{en}}, \text{and } \Omega_{\text{sep}} \qquad (5\text{-}6)$$

$$D_{i,\text{eff}} = \varepsilon_l^{1.5} D_i, \quad \text{in } \Omega_{\text{ep}}, \Omega_{\text{en}}, \text{and } \Omega_{\text{sep}} \qquad (5\text{-}7)$$

$$\mu_{i,\text{eff}} = D_{i,\text{eff}}/RT, \quad \text{in } \Omega_{\text{ep}}, \Omega_{\text{en}}, \text{and } \Omega_{\text{sep}} \qquad (5\text{-}8)$$

where ε_l is the volume fraction of the liquid phase, t is the time, F is the Faraday constant ($F = 96485.3\ \text{C/mol}$), ϕ_l is the electrolyte potential, $\boldsymbol{u}$ is the fluid velocity vector, R is the molar gas constant, and T is the temperature. c_i, $\boldsymbol{N}_i$, R_i, $D_{i,\text{eff}}$, z_i, and $\mu_{i,\text{eff}}$ denote the concentration, total mass flux, rate of production (or consumption), effective diffusivity, charge number, and effective mobility in a porous medium of *i*th species, respectively.

In the positive or negative electrode (Ω_{ep} or Ω_{en}), R_i is described by the Butler-Volmer-type electrochemical reaction equations as follows:

$$R_i = -\frac{v_{\text{Li}^+} i_{\text{loc}}}{nF}, \quad \text{in } \Omega_{\text{ep}} \text{ and } \Omega_{\text{en}} \qquad (5\text{-}9)$$

$$i_{\text{loc}} = i_0 \left[\exp\left(\frac{\alpha_{\text{a}} F\eta}{RT}\right) - \exp\left(-\frac{\alpha_c F\eta}{RT}\right)\right], \quad \text{in } \Omega_{\text{ep}} \text{ and } \Omega_{\text{en}} \qquad (5\text{-}10)$$

$$i_0 = F(k_{\text{c}})^{\alpha_{\text{c}}}(k_{\text{a}})^{\alpha_{\text{a}}}\left(c_{\text{s,max}} - c_{\text{s}}\right)^{\alpha_{\text{a}}}(c_{\text{s}})^{\alpha_{\text{c}}}\left(c_{\text{l}}/c_{\text{l,ref}}\right), \quad \text{in } \Omega_{\text{ep}} \text{ and } \Omega_{\text{en}} \qquad (5\text{-}11)$$

$$\eta = \phi_{\text{s}} - \phi_{\text{l}} - E_{\text{eq}}, \quad \text{in } \Omega_{\text{ep}} \text{ and } \Omega_{\text{en}} \qquad (5\text{-}12)$$

where v_{Li^+} is the stoichiometric coefficient in the reduction equation of Li^+ (i.e., $v_{\text{Li}^+} = -1$), i_{loc} is the local current density, n is the number of electrons participating in the reduction equation of Li^+, i_0 is the exchange current density, α_{a} is the anodic reaction rate coefficient, α_{c} is the cathodic reaction rate coefficient, η is the overpotential, ϕ_{s} is the electrode potential,

E_{eq} is the equilibrium potential, k_{a} is the anodic reaction rate constant, k_{c} is the cathodic reaction rate constant, c_{s} is the concentration of lithium in the solid phase (i.e., LiΘ), $c_{\mathrm{s,max}}$ is the maximum concentration of lithium in the solid phase ($c_{\mathrm{s,max}} = 22860\ \mathrm{mol/m^3}$ in LMO particles), c_{l} is the concentration of lithium in the liquid phase (i.e., Li^+), and $c_{\mathrm{l,ref}}$ is the reference concentration of lithium in the liquid phase.

The charge transfer is considered by solving the charge conservation equations while the electrochemical reaction takes place in each electrode:

$$\boldsymbol{I}_{\mathrm{cell}} = \boldsymbol{i}_{\mathrm{l}} + \boldsymbol{i}_{\mathrm{s}}, \quad \text{in } \Omega_{\mathrm{ep}}, \Omega_{\mathrm{en}}, \text{and } \Omega_{\mathrm{sep}} \quad (5\text{-}13)$$

$$\boldsymbol{i}_{\mathrm{l}} = F\sum_i z_i\left(-D_{i,\mathrm{eff}}\nabla c_i - z_i\mu_{i,\mathrm{eff}}Fc_i\nabla\phi_{\mathrm{l}}\right), \quad \text{in } \Omega_{\mathrm{ep}}, \Omega_{\mathrm{en}}, \text{and } \Omega_{\mathrm{sep}} \quad (5\text{-}14)$$

$$\boldsymbol{i}_{\mathrm{s}} = -\sigma_{\mathrm{s,eff}}\nabla\phi_{\mathrm{s}}, \quad \text{in } \Omega_{\mathrm{ep}} \text{ and } \Omega_{\mathrm{en}} \quad (5\text{-}15)$$

$$\sigma_{\mathrm{s,eff}} = {\varepsilon_{\mathrm{s}}}^{1.5}\sigma_{\mathrm{s}}, \quad \text{in } \Omega_{\mathrm{ep}} \text{ and } \Omega_{\mathrm{en}} \quad (5\text{-}16)$$

where $\boldsymbol{I}_{\mathrm{cell}}$ is the current density within the electrochemical cell, $\boldsymbol{i}_{\mathrm{l}}$ is the electrolyte current density, $\boldsymbol{i}_{\mathrm{s}}$ is the electrode current density, $\sigma_{\mathrm{s,eff}}$ is the effective conductivity of *i*th species in a porous medium.

As Li^+ is inserted by the electrochemical reaction at the LMO particle surface, Li^+ diffuses into the center of the LMO particle because of its concentration gradient. If the LMO particle is modeled as an ideal sphere with a radius of r_{p}, the concentration of recovered lithium in the solid phase (c_{s}) is described by the following mass balance equations:

$$\frac{\partial c_s}{\partial t} = \nabla \cdot (-D_s \nabla c_s) \quad (0 \le r \le r_p), \qquad \text{in } \Omega_{ep} \text{ and } \Omega_{en} \qquad (5\text{-}17)$$

$$\left.\frac{\partial c_s}{\partial r}\right|_{r=0} = 0, \qquad \text{in } \Omega_{ep} \text{ and } \Omega_{en} \qquad (5\text{-}18)$$

$$-D_s \left.\frac{\partial c_s}{\partial r}\right|_{r=r_p} = \frac{\nu_{Li\Theta} i_{loc}}{nF}, \qquad \text{in } \Omega_{ep} \text{ and } \Omega_{en} \qquad (5\text{-}19)$$

where D_s is the diffusivity of Li^+ within the LMO particle. At the surface of LMO particle ($r = r_p$), c_s increases by the lithium intercalation reaction. As the recovered lithium diffuses into the center of the LMO particle, c_s within the particle ($0 < r < r_p$) gradually increases.

In the separator channel (Ω_{sep}), $R_i = 0$ because there is no electrochemical reaction. The velocity profile ($\boldsymbol{u}$) in Ω_{sep} is obtained by solving the Navier-Stokes equation and the continuity equation.

$$\rho_l(\boldsymbol{u} \cdot \nabla \boldsymbol{u}) = -\nabla p + \mu_l \nabla^2 \boldsymbol{u} \qquad \text{in } \Omega_{sep} \qquad (5\text{-}20)$$

$$\nabla \cdot \boldsymbol{u} = 0 \qquad \text{in } \Omega_{sep} \qquad (5\text{-}21)$$

where ρ_l is the density of the liquid water, p is the pressure, and μ_l is the density of the liquid water. Square-shaped obstacles are placed within the channel to mimic the flow patterns in the spacer-filled channel. The flow field obtained in this study identical with that used in our previous study (Joo et al. 2020a).

In the AEM (Ω_m), the mass transfer of cations is assumed to be completely blocked, where the charge transfer is performed solely by the conduction through the fixed positive electrolyte as below:

$$\boldsymbol{i}_{\mathrm{l}} = -\sigma_{\mathrm{m}} \nabla \phi_{\mathrm{m}}, \qquad \text{in } \Omega_{\mathrm{m}} \tag{5-22}$$

$$\phi_{\mathrm{l}} - \phi_{\mathrm{m}} = \frac{RT}{z_{\mathrm{Cl}^-} F} \ln\left(\frac{c_{\mathrm{Cl}^-}}{c_{\mathrm{m}}}\right) \qquad \text{at } x = \delta + L_{\mathrm{sep}},\ \delta + L_{\mathrm{sep}} + L_{\mathrm{m}} \tag{5-23}$$

where σ_{m} is the electrolyte conductivity in the membrane, ϕ_{m} is the electrolyte potential in the membrane, and c_{m} is the concentration of immobilized charged species (i.e., ionomers) in the membrane. Since the AEM is modeled as a non-conducting material, $\boldsymbol{i}_{\mathrm{s}} = 0$.

Table 5-2 summarizes the initial and boundary conditions applied in our simulation. Other parameters used in our simulation are listed in **Table 5-3**. The number of computational elements was 89,643, whose mesh independence was tested in our previous study (Joo et al. 2020a). A commercial software, COMSOL Multiphysics 5.6 (COMSOL Inc.), was used to perform the numerical simulations. A workstation with a hexacore processor (Intel® Xeon® E-2286G CPU 4.01GHz) and 64 GB memory was used in the numerical calculation.

Table 5-2 Initial and boundary conditions

Initial conditions

Equations	**Location**
$c_i = 0,\ c_\mathrm{s} = \mathrm{soc}_\mathrm{min} \cdot c_\mathrm{s,max}, \phi_\mathrm{l} = 0,\ \phi_\mathrm{s} = E_\mathrm{eq}(c_\mathrm{s})$	Positive electrode (Ω_ep)
$c_i = 0,\ c_\mathrm{s} = \mathrm{soc}_\mathrm{max} \cdot c_\mathrm{s,max}, \phi_\mathrm{l} = 0,\ \phi_\mathrm{s} = E_\mathrm{eq}(c_\mathrm{s})$	Negative electrode (Ω_en)
$c_i = c_{i,0},\ \phi_\mathrm{l} = 0,\ \phi_\mathrm{s} = 0$	Separator channel (Ω_sep)
$c_\mathrm{m} = 0,\ \phi_\mathrm{l} = 0,\ \phi_\mathrm{s} = 0$	AEM (Ω_m)

Boundary conditions

Equations	**Location**
$c_i = c_{i,0}$	at $y = 0$
$\boldsymbol{n} \cdot D_i \nabla c_i = 0$	at $y = H$
$\boldsymbol{n} \cdot \boldsymbol{N}_i = \boldsymbol{0}, \boldsymbol{i}_\mathrm{l} = \boldsymbol{0}, \boldsymbol{i}_\mathrm{s} = \boldsymbol{I}_\mathrm{cell}, \phi_\mathrm{l} = 0$	at $x = 0, 2\delta + 2L_\mathrm{sep} + L_\mathrm{m}$
$\boldsymbol{n} \cdot \boldsymbol{N}_i = \boldsymbol{0}, \boldsymbol{n} \cdot \boldsymbol{i}_\mathrm{l} = 0, \phi_\mathrm{l} - \phi_\mathrm{m} = \frac{RT}{z_{\mathrm{Cl}^-}F} \ln\left(\frac{c_{\mathrm{Cl}^-}}{c_\mathrm{m}}\right)$	at $x = \delta + L_\mathrm{sep}, \delta + L_\mathrm{sep} + L_\mathrm{m}$
$\boldsymbol{n} \cdot \boldsymbol{N}_i = \boldsymbol{0}, \boldsymbol{n} \cdot \boldsymbol{i}_\mathrm{l} = 0, \boldsymbol{n} \cdot \boldsymbol{i}_\mathrm{s} = 0$	otherwise

Table 5-3 Simulation parameters (a: assumed, c: calculated)

Symbol	Description	Value	Reference
L_s	Thickness of separator channel [μm]	200	(Joo et al. 2020a)
L_m	Thickness of AEM [μm]	100	(Joo et al. 2020a)
H	Height of electrode [cm]	2	(Joo et al. 2020a)
A_{sec}	Sectional area of the electrode [cm^2]	4	(Joo et al. 2020a)
D_{Li^+}	Diffusivity of Li^+ in liquid phase [$m^2\ s^{-1}$]	9.9×10^{-10}	(Vitagliano and Lyons 1956)
D_s	Diffusivity of Li^+ in solid phase [$m^2\ s^{-1}$]	6.0×10^{-14}	(Marchini et al. 2016)
D_{Cl^-}	Diffusivity of Cl^- [$m^2\ s^{-1}$]	2.0×10^{-9}	(Vitagliano and Lyons 1956)
ε_p	Volume fraction of non-conducting solid material in the electrode [-]	0.17	a
ε_l	Volume fraction of liquid in the electrode [-]	$1 - \varepsilon_p - \varepsilon_s$	c
$c_{Li^+,0}$	Initial concentration of Li^+ in separator channel [mol m^{-3}]	30	(Joo et al. 2020a)
$c_{Li^+,ref}$	Initial concentration of Li^+ in separator channel [mol m^{-3}]	1	(Romero et al. 2018)
$c_{Cl^-,0}$	Initial concentration of Cl^- in separator channel [mol m^{-3}]	30	(Joo et al. 2020a)
$c_{s,max}$	Maximum concentration of lithium in solid particle phase [mol m^{-3}]	22,860	(Joo et al. 2020a)

c_{m}	Concentration of fixed positive charge in AEM [mol m^{-3}]	1000	a
$\mathrm{soc}_{\mathrm{min}}$	Initial electrode state-of-charge in electrode of intercalation [-]	0.001	a
$\mathrm{soc}_{\mathrm{max}}$	Initial electrode state-of-charge in electrode of de-intercalation [-]	0.999	a
σ_{s}	Conductivity of solid phase in electrode [S m^{-1}]	3.8	c
σ_{m}	Electrolyte conductivity in AEM [S m^{-1}]	1	(COMSOL Inc. 2012)
k_{a}	Anodic reaction rate constant in electrode [m s^{-1}]	1.0×10^{-11}	(Romero et al. 2018)
k_{c}	Cathodic reaction rate constant in electrode [m s^{-1}]	1.0×10^{-11}	(Romero et al. 2018)
α_{a}	Anodic reaction rate coefficient in electrode [-]	0.5	(Doyle et al. 1993)
α_{c}	Cathodic reaction rate coefficient in electrode [-]	0.5	(Doyle et al. 1993)
T	Temperature of system [K]	298.15	a
ρ_{s}	Density of LMO [kg m^{-3}]	4140	(Schilcher et al. 2016)
ρ_{l}	Density of liquid water [kg m^{-3}]	1000	a
ρ_{p}	Density of non-conducting material [kg m^{-3}]	1780	(Ramazanov et al. 2018)
μ_{l}	Viscosity of liquid water [Pa·s]	0.001	a

5.2.3 Electrochemical cell test for the experimental input data

An electrochemical cell test was performed to confirm that our P2D model could adequately reproduce the cell voltage profile. Cell test conditions are basically similar to those in previous study (Joo et al. 2020a).

The cell configuration was as follows. $LiMn_2O_4$ electrode was fabricated by applying the slurry to graphite sheets using a doctor blade, followed by drying at 120 °C and vacuum. The slurry was a mixture of $LiMn_2O_4$ powder (TOB New Energy, China), Super P powder (Timcal, Switzerland), and polyvinylidene fluoride powder (PVDF; Sigma-Aldrich, USA) (weight ratio=80:10:10), which are combined with the solvent, 1-methyl-2-pyrrolidone (NMP; Sigma-Aldrich, USA). The value of the design parameters of this electrode were r_p=0.311 μm, ε_s=0.28, and δ=40 μm. The λ-MnO_2 electrode was fabricated through de-lithiation of the $LiMn_2O_4$ electrode under the constant voltage mode (operation time: 120 min, potential: 1.2V vs reference) in the three-electrode cell configuration (working: λ-MnO_2, counter: Pt mesh, reference: Ag/AgCl/KCl saturated). The rocking-chair flow type ELR cell consists of the separator (Yamanaka Industry Co., Ltd, Japan), anion exchange membrane (AMV; Selemion, Japan), and another separator between two square shaped electrodes ($LiMn_2O_4$ and λ-MnO_2 electrode) of

2.0 cm × 2.0 cm. Both ends were packed with silicon gasket and end plate.

The cell test was performed as follows. In the galvanostatic charge/discharge test using a battery cycler (WBCS3000; WonATech, Korea), the current density of $62.5\ \mu A/cm^2$ was applied with voltage cut of ±0.7 V (the direction of current was opposite at Step 1 and 2). At the same time, electrolyte (30 mM LiCl) was supplied to both flow channels at a rate of 1 ml/min using a peristaltic pump (REGLO ICC; ISMATEC, USA).

The result of an electrochemical cell test is included in the **Figure 5-2**. Our ELR system is operated at a constant current density, $|\boldsymbol{I}_{\text{cell}}| = 62.5\ \mu A/cm^2$, which is low enough to avoid severe Ohmic drop. Note that under the low current condition, the electrochemical reaction is limited by charge transfer rather that mass transfer, which can be described by Bulter-Volmer kinetics (Equation (5-10)).

Figure 5-3 shows the Tafel plot of λ-MnO_2 and $LiMn_2O_4$ electrode in 30 mM LiCl electrolyte. The potential step is 1 mV with the step time of 3 seconds. The current density of this study ($62.5\ \mu A/cm^2$) corresponds to a section where the value of overpotential is relatively small. Therefore, in this voltage range, the electrochemical reaction is limited by the charge transfer rather than the mass transfer, and the Butler-Volmer kinetics can be used.

For the validation of the simulation results, experiments were conducted

with varying r_p. r_p was controlled by using standard test sieve (CHUNG GYE SANG GONG SA, Korea) with sieve size of 20, 75, and 180 μm (10, 38, 90 μm for r_p, respectively). These sieves were used to separate LMO particles into three ranges: under 10, from 10 to 38, and from 38 to 90 μm. Except these r_p controls, the electrochemical cell test for experimental validation was performed identically as previously mentioned.

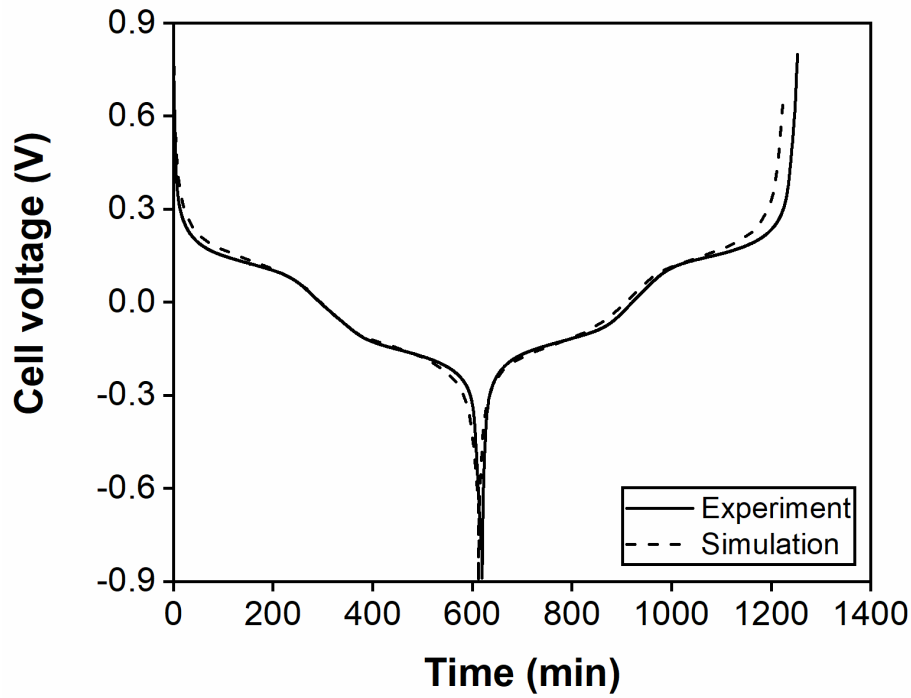

Figure 5-2 Galvanostatic charge/discharge profile of the λ-MnO_2/$LiMn_2O_4$ ELR system (current density=62.5 μA/cm^2, r_p=0.311 μm, ε_s=0.28, δ=40 μm). The cell voltage profile calculated by the numerical simulation matches well with the profile from the experimental result.

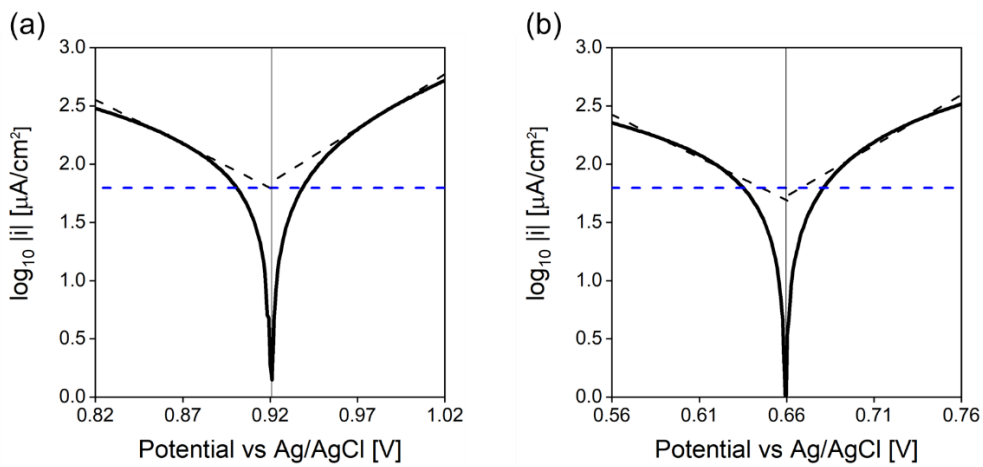

Figure 5-3 Tafel plot for anodic and cathodic branches of the current density-potential curve for (a) λ-MnO_2 electrode and (b) $LiMn_2O_4$ electrode. The blue line represents the current density condition of 62.5 $\mu A/cm^2$.

5.2.4 Electrode design parameters and performance indicators

Using the model above, the effect of three major electrode design parameters was investigated and their definitions were summarized in **Table 5-4**. The values of electrode design parameters were assigned in a typical range of an electrode fabrication. A relatively wide range of r_{p} is studied, from 0.1 μm to 10 μm, considering the size distribution of LMO particles in the previous experimental studies (Lee 2006; Cui et al. 2017). ε_{s} is changed from 0.16 to 0.4 which falls in its typical range in the conventional electrode fabrication (Devan et al. 2004; Smith and Bazant 2017). ε_{s} is known to be affected by complex colloidal interaction, rheological properties, and the evaporation behavior of the slurry. δ is manipulated from 40 μm to 160 μm to represent typical electrode thickness in the previous studies (Joo et al. 2020a; Niu et al. 2021).

To quantitatively evaluate the system performance, three performance indicators (Q, $q_{\mathrm{Li^+}}$ and W_{net}) are calculated from the voltage-capacity profile and the amount of recovered lithium in the solid phase. The specific capacity (Q, in mAh $\mathrm{g^{-1}}$), the specific mass of $\mathrm{Li^+}$ recovered per 1 g of LMO particles ($q_{\mathrm{Li^+}}$, in mg $\mathrm{g^{-1}}$), and the net energy consumption per 1 mole of $\mathrm{Li^+}$ recovered (W_{net}, in Wh $\mathrm{mol^{-1}}$) are defined as:

$$Q = \frac{|\boldsymbol{I}_{\text{cell}}|t}{\alpha m_{\text{elec}}} \tag{5-24}$$

$$q_{\text{Li}^+} = \frac{m_{\text{Li}^+} \int_{\Omega_{\text{ep}}} [c_{\text{s}}(t_{\text{f}}) - c_{\text{s}}(0)] \varepsilon_{\text{s}} d\Omega}{\alpha m_{\text{elec}}} \tag{5-25}$$

$$W_{\text{net}} = \frac{|\boldsymbol{I}_{\text{cell}}| \left(\int_{\Delta E<0} |\Delta E| dt - \int_{\Delta E>0} \Delta E dt \right)}{\int_{\Omega_{\text{ep}}} [c_{\text{s}}(t_{\text{f}}) - c_{\text{s}}(0)] \varepsilon_{\text{s}} d\Omega} \tag{5-26}$$

where α is the mass fraction of the active material (in this study, LMO particles) in the electrode, m_{elec} is the mass of the electrode, m_{Li^+} is the molar mass of Li^+ (= 6.941 g mol^{-1}), t_{f} is the time elapsed until a lithium recovery step is finished, Ω is the volume element, and ΔE is the cell voltage. αm_{elec} is determined by the choice of ε_{s} and δ, since $\alpha m_{\text{elec}} = \varepsilon_{\text{s}} \rho_{\text{s}} V_{\text{elec}} = \varepsilon_{\text{s}} \rho_{\text{s}} \delta A_{\text{sec}}$, where ρ_{s} is the density of the LMO, V_{elec} is the volume of the electrode (Ω_{ep}), and A_{sec} is the cross-sectional area of the electrode.

Table 5-4 Electrode design parameters

Symbol	Definition	Values
r_{p}	Effective radius of LMO particles [μm]	0.1, 3.4, 6.7, 10
ε_{s}	Volume fraction of LMO particles in the electrode [-]	0.16, 0.24, 0.32, 0.40
δ	Electrode thickness [μm]	40, 100, 160

5.2.5 Working principles

In this section, it is explained how the ELR system works by inspecting the potential change in the positive and negative electrodes and the lithium concentration in the separator channels and in the LMO particle. **Figure 5-4** shows profiles of LMO electrode potential and Li^+ concentration in each sub-domain, obtained from a numerical simulation when $\{r_p, \varepsilon_s, \delta\}$ = {0.1 μm, 0.4, 40 μm}. Although this one case was analyzed in this section, the overall change in the potential and concentration profiles are typical enough to represent the other cases. **Figure 5-4a** represents the electric potential profile with respect to the normalized specific capacity of the Li^+ capturing electrode. The electric potential of the LMO electrode is determined by two factors: thermodynamics and kinetics. The thermodynamic factor is correlated with Li^+ contents in the LMO particle. When Li^+ is intercalated into the host structure of λ-MnO_2, the electrode potential decreases due to the configurational entropy of guest ions (Li^+) and the Fermi level of electrons (Huggins 2008). When Q/Q_{max} is 0 to 0.5 and 0.5 to 1.0, two intervals with relatively small potential changes appear. These intervals are called plateau where phase transition occurs. The kinetic factor is correlated with the current density applied to the LMO particle surface, which is called local current

density. When a local current density higher than the exchange current density is applied, the electrode potential becomes lower than the thermodynamic potential. The difference between two potentials is called overpotential which is determined by the Bulter-Volmer equation (see Equation (5-10)). An opposite trend can be observed in the Li^+ releasing electrode (**Figure 5-4b**). When Li^+ is de-intercalated from the host structure of $LiMn_2O_4$, the electrode potential increases. Due to the kinetic effect, the electrode potential becomes higher than the thermodynamic potential. The potential difference between the two electrodes is expressed as cell voltage (see **Figure 3** below).

Figure 5-4c and **d** show the concentration distribution of Li^+ with time in the electrolyte region. A dashed line divides the porous electrode region (narrow part) and flow channel region (wide part). As shown in **Figure 5-4c**, Li^+ is captured by the λ-MnO_2 electrode and Li^+ concentration of electrolyte adjacent to Ω_{ep} decreases. Li^+ concentration decreases sharply in the porous electrode sub-domain (Ω_{ep}). Conversely, Li^+ is released from the $LiMn_2O_4$ electrode and Li^+ concentration of electrolyte adjacent to Ω_{en} increases as depicted in **Figure 5-4d**. Li^+ concentration increases sharply in the porous electrode sub-domain (Ω_{en}). In both sub-domains, the concentration change is not large near the middle of the flow channel. This is because the new influent (30 mM LiCl) is continuously supplied, and the flow rate is the fastest

in this part. Note that the change of electrolyte concentration within the electrode can cause the change of E_{eq}. However, in this study, the change of concentration is so slight (less than 0.5 mM) that the change of E_{eq} is negligible. It was proved by the experimental test performed in the previous study (Joo et al. 2020a).

Figure 5-4e and **f** show the concentration distribution of lithium with time in the solid phase. **Figure 5-4e** illustrates the c_{s} distribution of the LMO particle in Ω_{ep}. $r/r_{\mathrm{p}} = 1$ and 0 correspond to the surface and the center of the LMO particle, respectively. As Li^+ is inserted into the LMO particle, Li^+ diffuses toward the center of the particle, and the state-of-charge (SoC) value increases from 0% to 100%. The extent of intercalation reaction has a positive correlation with c_{s} at the surface of LMO particle ($c_{\mathrm{s,surface}}$); therefore, if $c_{\mathrm{s,surface}}$ reaches around $c_{\mathrm{s,max}}$ $(= 22860\ \mathrm{mol/m^3})$, the electrochemical reaction is terminated (note that termination condition of the step is decided by cell voltage which is influenced by two factors: $c_{\mathrm{s,surface}}$ and overpotential). In this process, even if the inside of the particle is not fully utilized, the reaction can be terminated. An opposite trend is shown in **Figure 5-4f**, which represents the c_{s} distribution of the LMO particle in Ω_{en}. Li^+ is released through the surface of the LMO particle, which induces a concentration gradient of Li^+ inside the particle. Li^+ inside a particle diffuses

toward the surface of the LMO particle. Contrary to the case of **Figure 5-4e**, when the $c_{\mathrm{s,surface}}$ is reached around 0, the electrochemical reaction is terminated. As a result, unreleased lithium ions remain inside the particle. The utilization of the intercalation site inside the LMO particle can be estimated by $q_{\mathrm{Li^+}}$.

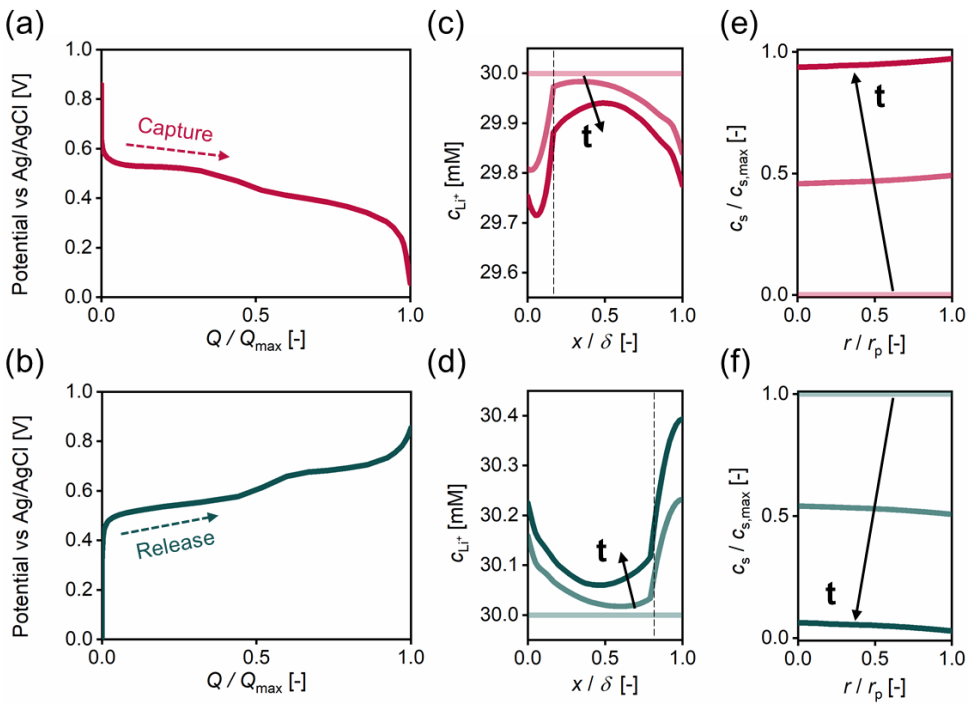

Figure 5-4 Potential profiles of electrodes and concentration profiles in separator channels and LMO particles, obtained from a numerical simulation when $\{r_p, \varepsilon_s, \delta\}$ = {0.1 μm, 0.4, 40 μm}. Red indicates the capturing electrode (λ-MnO_2) and blue indicates the releasing electrode ($LiMn_2O_4$). (a) and (b) are potential curves of each electrode, (c) and (d) are the concentration profiles of the lithium-ion in the separator channel including Ω_{ep} and Ω_{en}, respectively, and (e) and (f) are the concentration profiles of the lithium-ion in the LMO particles in the sub-domain Ω_{ep} and Ω_{en}, respectively.

5.3. Results and discussion

5.3.1 Overall voltage profile acquired from the parameter study

Figure 5-5 represents the effect of design parameters on the cell voltage profiles. Cell voltage is determined by the difference between the potential at the positive and the negative electrodes (represented in **Figure 5-4a** and **d**, respectively) and the Ohmic drop. In all cases, this electrochemical system is operated in a low voltage range. Specifically, cell voltage decreases from +0.9 V to −0.9 V in Step 1, while cell voltage increases from −0.9 V to +0.9 V in Step 2. Cell voltage profiles of Step 1 and Step 2 are symmetric to each other as discussed in 5.2. Two plateaus are identified in all the cell voltage curves, as Li^+ intercalation and de-intercalation occur simultaneously. As r_p increases, the cell voltage curve moves vertically down and the width of the curve ($= Q_{max}$) is shortened in Step 1. As ε_s or δ increases, on the other hand, the cell voltage curve moves vertically up and the width of the curve is lengthened in Step 1. In the following sections, these changes in the cell voltage profile with respect to electrode design parameters are further analyzed in terms of the performance indicators, q_{Li^+} and W_{net}.

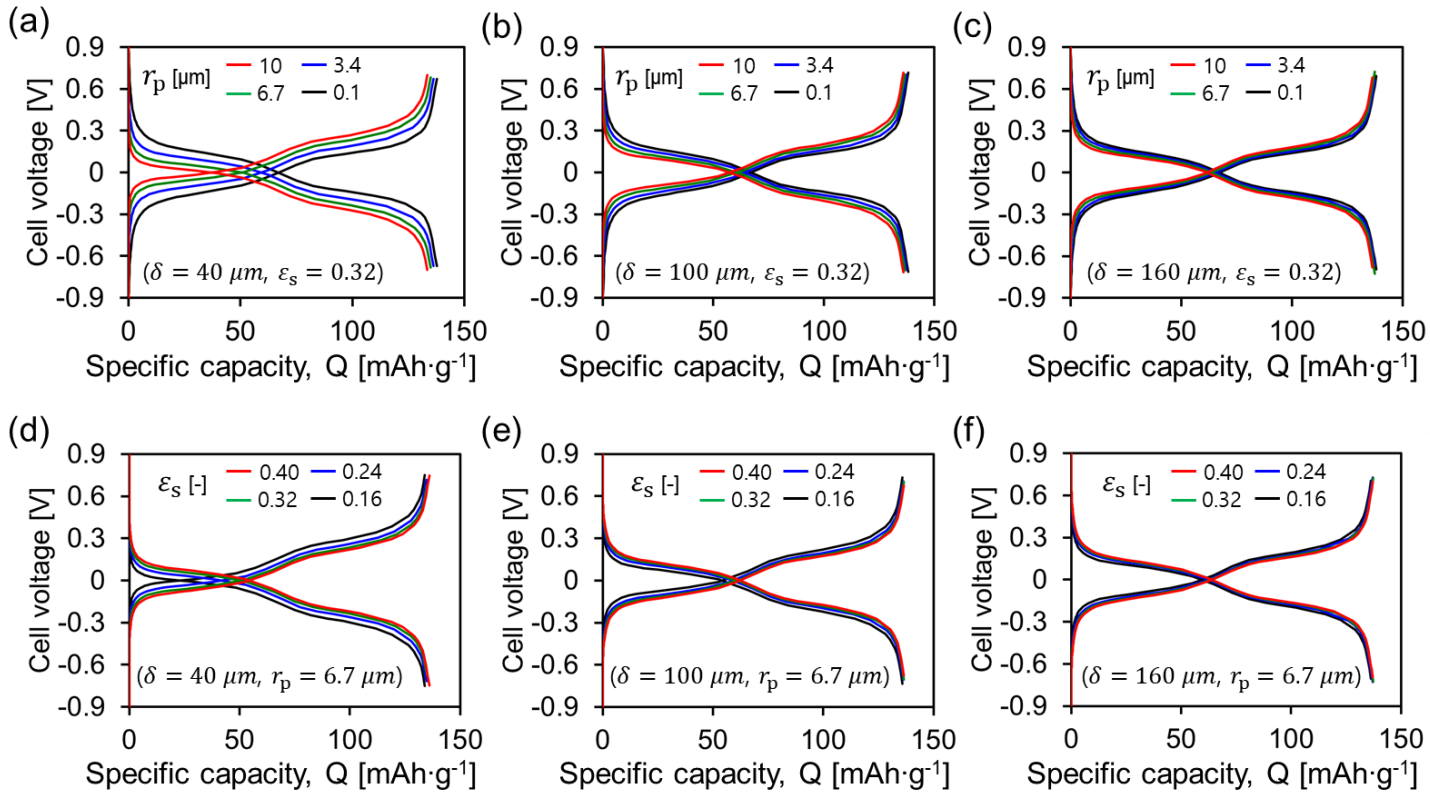

Figure 5-5 Cell voltage profiles with specific capacity (Q) at varying combinations of r_p, ε_s, and δ. Effect of r_p on the cell voltage profiles when (a) $\delta = 40$ μm, (b) $\delta = 100$ μm, and (c) $\delta = 160$ μm (ε_s is fixed at 0.32). Effect of ε_s on the cell voltage profile when (d) $\delta = 40$ μm, (e) $\delta = 100$ μm, and (f) $\delta = 160$ μm (r_p is fixed at 6.7 μm).

5.3.2 Effect of electrode design parameters on the specific mass of Li^+ recovered (q_{Li^+})

Figure 5-6 illustrates the effect of electrode design parameters on q_{Li^+}. The calculated q_{Li^+} is changed from 37.66 mg/g to 35.71 mg/g, showing a 5.5% difference between them. When $\delta = 40\ \mu m$, the maximum and the minimum of q_{Li^+} are 37.59 mg/g and 35.71 mg/g, respectively, whose difference is 1.88 mg/g (a 5.25% difference between them). As δ increases from 40 μm to 160 μm, the maximum and the minimum of q_{Li^+} become 37.66 mg/g and 37.05 mg/g, whose difference decreases to 0.61 mg/g (a 1.63% difference between them). Similar trends were found in **Figure 5-5**, where the difference in cell voltage curves is diminished as δ increases. It is also found that q_{Li^+} is negatively correlated with r_p, while it is negatively correlated with ε_s and δ. Further investigation on the Li^+ intercalation into the LMO particle is performed to unveil the correlation between the electrode design parameters and q_{Li^+}.

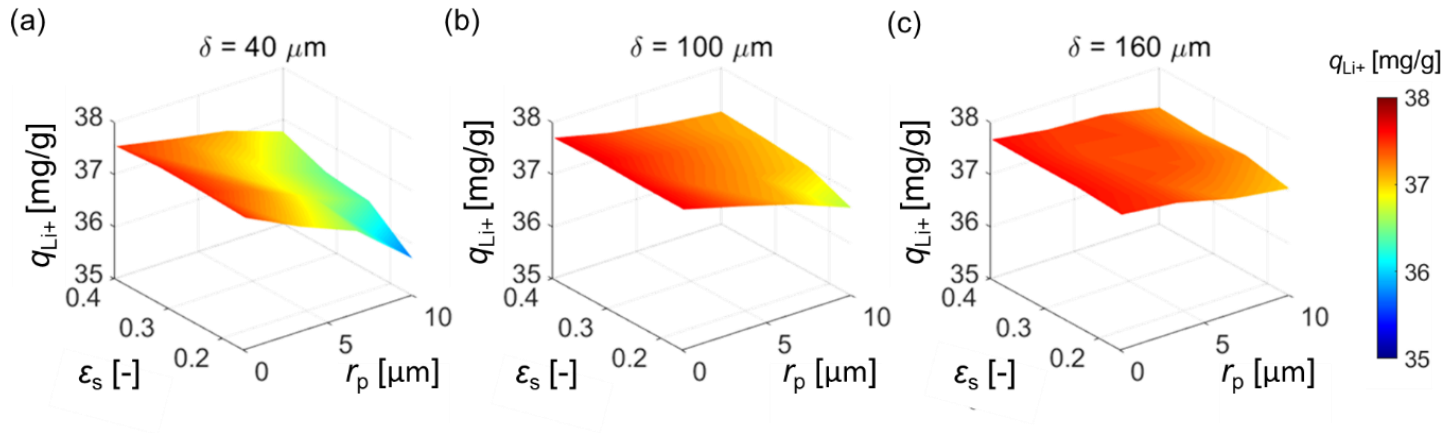

Figure 5-6 Contour plots of the specific mass of Li^+ recovered (q_{Li^+}) when (a) $\delta = 40$ μm, (b) $\delta = 100$ μm, and (c) $\delta = 160$ μm

Figure 5-7a shows the effect of r_p on the concentration of lithium in the solid phase (c_s) within the LMO particle at SoC = 100% (see **Figure 5-8** to **Figure 5-10** for c_s at intermediate SoC values). When $r_p = 0.1$ μm, c_s at the center of the LMO particle almost reaches $c_{s,max}$. As r_p increases to 10 μm, however, c_s at the center of the LMO particle gradually decreases, leaving the core region unsaturated. This trend is observed since the time required for the saturation of surface (by the Li^+ intercalation reaction) becomes far shorter than that of the core region (by the Li^+ diffusion), as r_p increases from 0.1 μm to 10 μm. This discrepancy in the saturation time is related to the specific area of the LMO particle. As r_p increases, the specific area of the LMO particle decreases, which in turn increases the local current density applied to the particle surface. As the local current density increases, the rate of Li^+ intercalation reaction at the particle surface is accelerated, exceeding the rate of Li^+ diffusion into the center of the particle. Note that diffusion coefficient in the LMO particle is not changed when r_p is changed. Instead, the flux of Li^+ increases linearly as r_p increases.

Figure 5-7b shows the effect of ε_s on c_s within the LMO particle. As ε_s increases, $c_s/c_{s,max}$ profiles move vertically up, resulting in more Li^+ insertion into the particle. This tendency is associated with the local current

density applied to the electrode. As ε_s increases, the mass of the active material in unit volume ($\alpha m_{elec} = \varepsilon_s \rho_s \delta A_{sec}$) increases, making the local current density applied to each LMO particle reduced. As the local current density decreases, Li^+ flux at the surface of the particle is lowered due to the slow intercalation reaction. Thus, as discussed above, Li^+ can diffuse into the center of the particle for a longer time before the surface saturation, hence an enhanced lithium recovery performance.

The effect of δ on c_s is illustrated in **Figure 5-7c**. As δ increases, $c_s/c_{s,max}$ profiles move vertically up, showing a similar trend as ε_s. Thus, a similar argument can be made again by noting that the local current density is reduced with increasing δ and fixed ε_s. Based on this discussion, to enhance the recovery efficiency of Li^+ in the ELR system, it is preferred to design thicker electrodes with smaller LMO particles and high solid volume fraction.

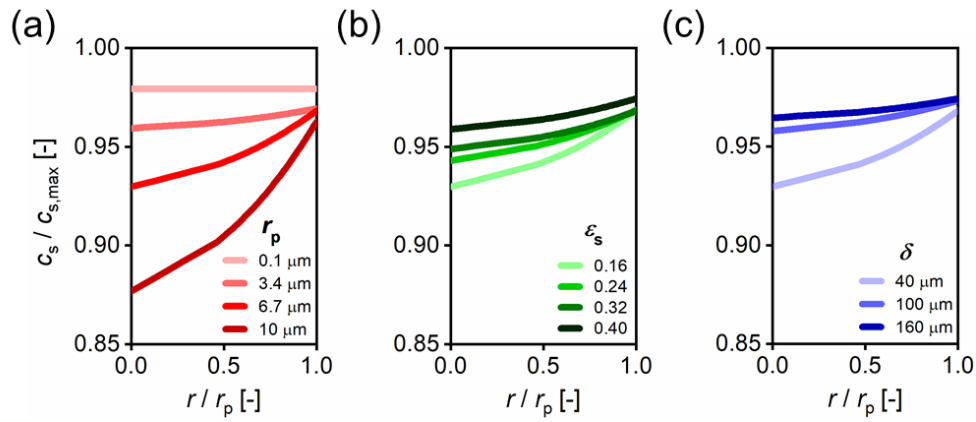

Figure 5-7 The dimensionless concentration of lithium in the solid phase (c_s) within the LMO particle at SoC = 100 % when (a) r_p = 0.1, 3.4, 6.7, and 10 μm (δ = 40 μm and ε_s = 0.16), (b) ε_s = 0.16, 0.24, 0.32, and 0.40 (δ = 40 μm and r_p = 6.7 μm), and (c) δ = 40, 100, and 160 μm (ε_s = 0.32 and r_p = 6.7 μm)

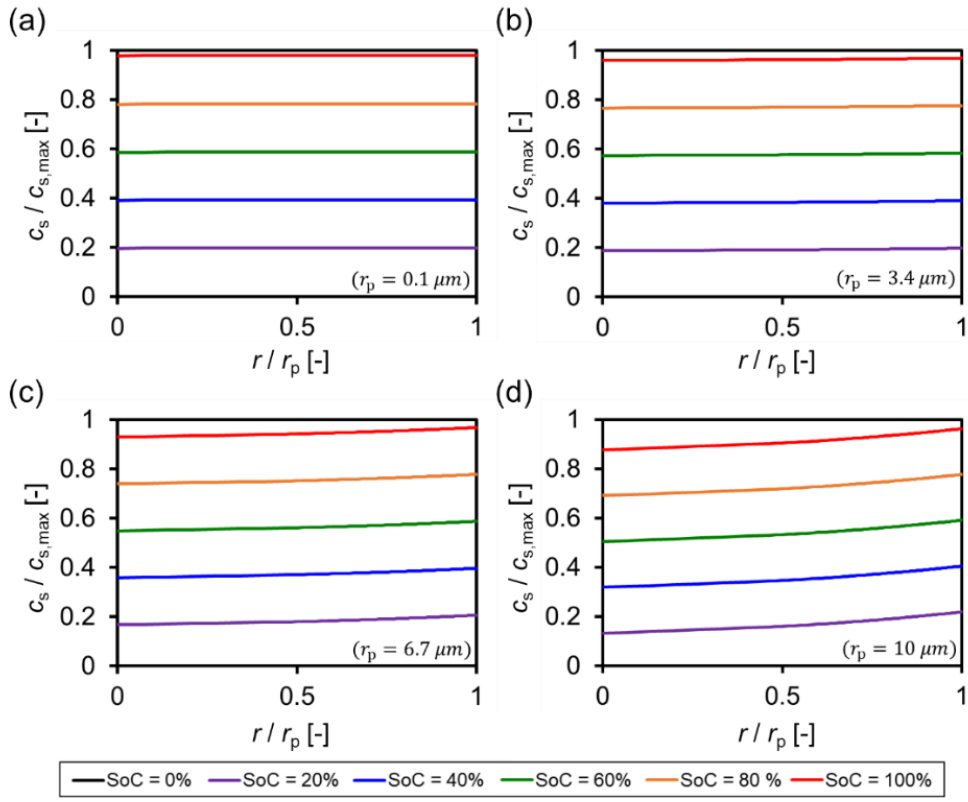

Figure 5-8 The dimensionless concentration of lithium in the solid phase (c_s) within the LMO particle when (a) $r_p = 0.1$ µm, (b) $r_p = 3.4$ µm, (c) $r_p = 6.7$ µm, and (d) $r_p = 10$ µm. Other electrode design parameters are fixed at constant values: $\delta = 40\ \mu m$ and $\varepsilon_s = 0.16$.

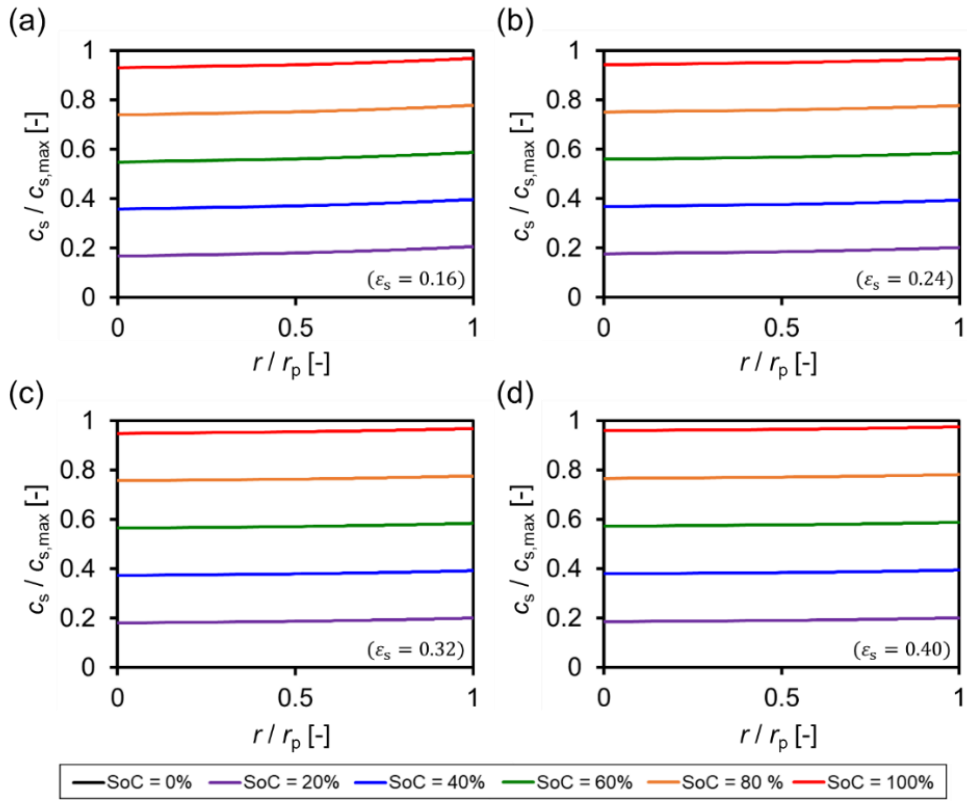

Figure 5-9 The dimensionless concentration of lithium in the solid phase (c_s) within the LMO particle when (a) $\varepsilon_s = 0.16$, (b) $\varepsilon_s = 0.24$, (c) $\varepsilon_s = 0.32$, and (d) $\varepsilon_s = 0.40$. Other electrode design parameters are fixed at constant values: $\delta = 40\ \mu m$ and $r_p = 6.7\ \mu m$

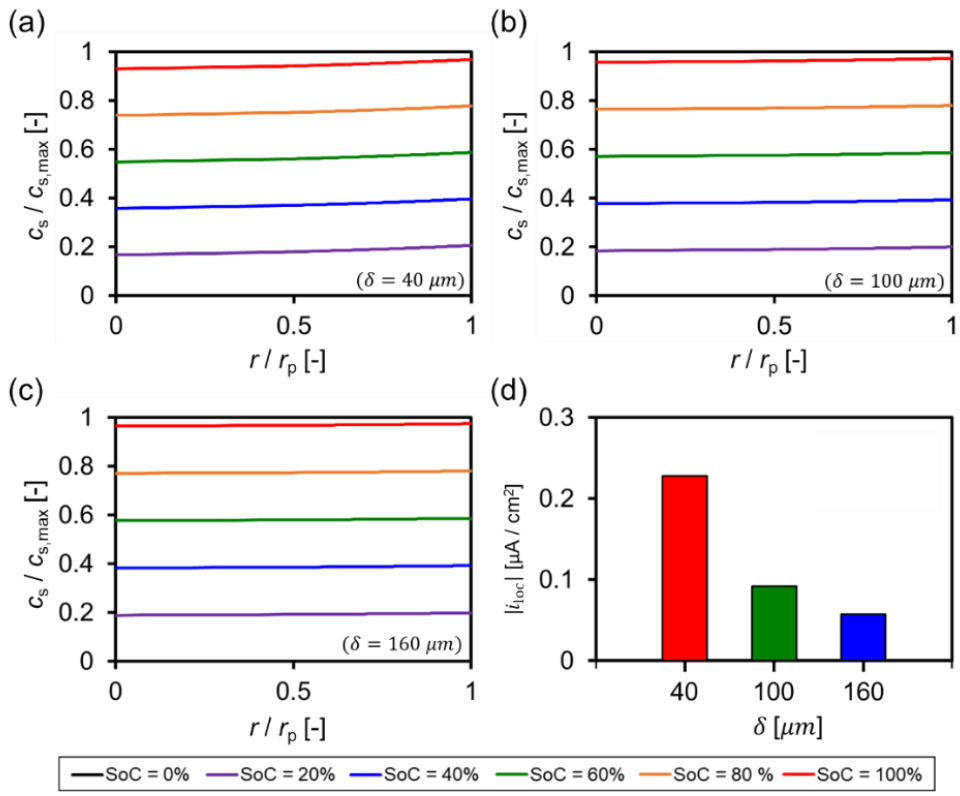

Figure 5-10 The dimensionless concentration of lithium in the solid phase (c_s) within the LMO particle when (a) $\delta = 40$ µm, (b) $\delta = 100$ µm, and (c) $\delta = 40$ µm. Other electrode design parameters are fixed at constant values: $\varepsilon_s = 0.32$, $r_p = 6.7$ µm. (d) The local current density value at varying electrode thickness

5.3.3 Effect of electrode design parameters on the net energy consumption (W_{net})

To evaluate the net energy consumption per 1 mole of Li^+ recovered (W_{net}), the voltage-capacity profiles in **Figure 5-5** are numerically integrated (see Equation (5-26) and **Figure 5-11**). The following discussion is for Step 1 (similar statements can be made for Step 2). When $\Delta E > 0$, a spontaneous electrochemical reaction takes place, where energy is generated. When $\Delta E < 0$, a specific amount of energy should be consumed to proceed with the electrochemical reaction. In this study, it is assumed that the energy generated in the region with $\Delta E > 0$ can be fully recovered, which compensates for the energy consumption in the region with $\Delta E < 0$. Please refer to the previous study (Joo et al. 2020a) for a further discussion on energy consumption with and without energy recovery.

Figure 5-12 illustrates the effect of electrode design parameters on W_{net}. The calculated W_{net} varies from 5.44 Wh/mol to 0.17 Wh/mol, whose difference is 5.27 Wh/mol (a 3075% difference between them). It is apparent that the difference in W_{net} is much more significant than that in $q_{\mathrm{Li^+}}$. Interestingly, the dependence of W_{net} on the electrode design parameters behaves similarly with that of $q_{\mathrm{Li^+}}$, i.e. W_{net} is positively correlated with r_{p}, and negatively correlated with ε_{s} and δ.

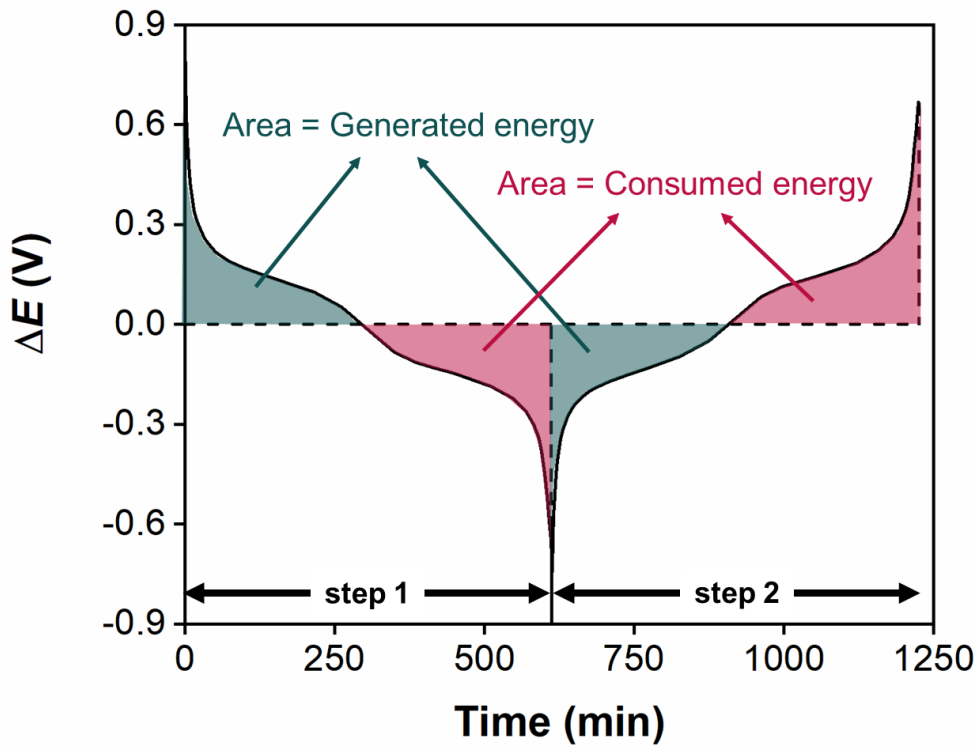

Figure 5-11 Graphical illustration of the energy consumption with energy recovery. The green area ($\Delta E > 0$ in step 1 and $\Delta E < 0$ in step 2) represents the amount of generated energy and the red area ($\Delta E < 0$ in step 1 and $\Delta E > 0$ in step 2) represents the amount of consumed energy. Net energy consumption (W_{net}) is the difference between the consumed energy and generated energy in a step.

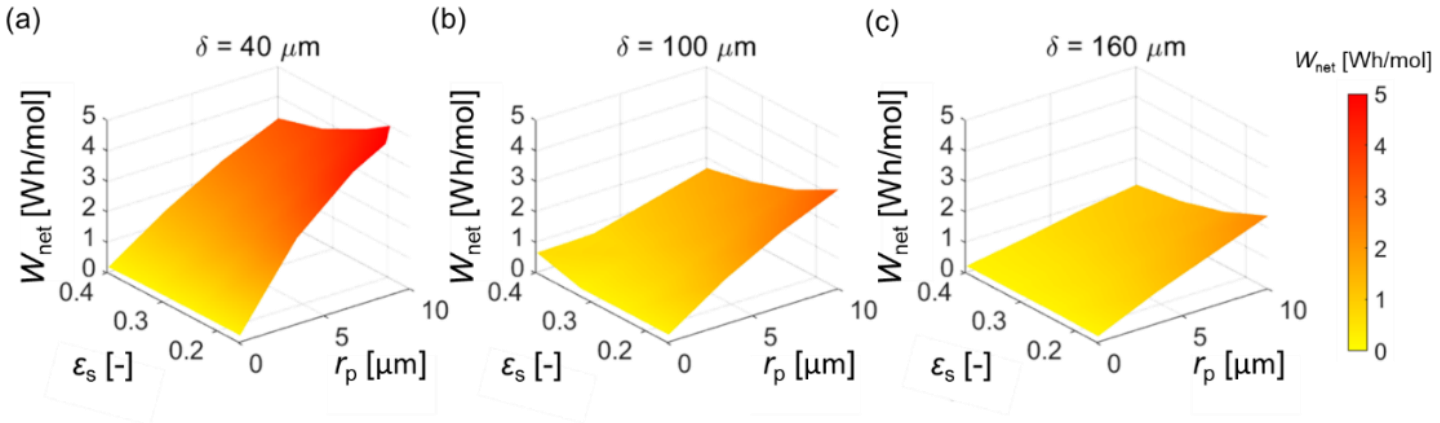

Figure 5-12 Contour plots of the net energy consumption (W_{net}) when (a) $\delta = 40$ μm, (b) $\delta = 100$ μm, and (c) $\delta = 160$ μm

The effect of each electrode design parameter on W_{net} is found to be related to the amount of electrochemical reaction occurring at the LMO particle surface. **Figure 5-13a** represents the dimensionless concentration of lithium in the solid phase at the LMO particle surface (i.e. $c_{\mathrm{s,surface}}/c_{\mathrm{s,max}}$) as a function of dimensionless specific capacity (i.e. Q/Q_{max}). It can be seen that the change in the overall profile is minimal with varying r_{p}. At the initial phase, however, the slope becomes steeper as r_{p} increases from 0.1 μm to 10 μm. It is because the cell voltage profile is significantly changed by the overpotential from a high level of local current density (see **Figure 5-13b**). As r_{p} increases, the cell voltage profile is vertically moved down to shrink the area of the energy recovery, and to enlarge the area of the energy consumption. Thus, W_{net} increases when a significant overpotential is provided in the system. The effects of ε_{s} and δ on W_{net} are also correlated with the local current density applied at the electrode. As ε_{s} and δ increase, the mass of active material in unit volume increases ($\alpha m_{\mathrm{elec}} = \varepsilon_{\mathrm{s}}\rho_{\mathrm{s}}\delta A_{\mathrm{sec}}$), which reduces the local current density. As the local current density decreases, the amount of overpotential is reduced, resulting in a reduction in energy consumption.

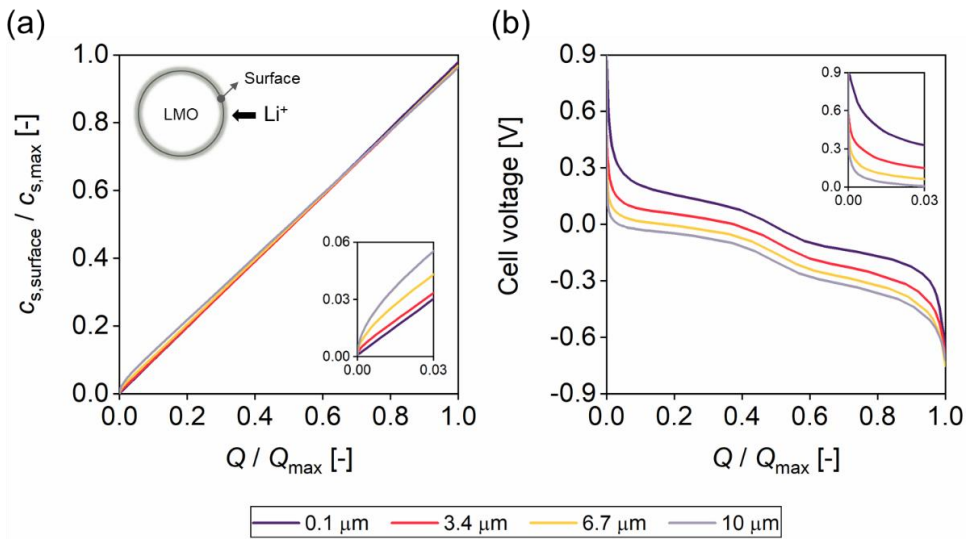

Figure 5-13 (a) Normalized $C_{\mathrm{s,surface}}$ profile and (b) cell voltage profile varying effective radius of LMO particle (r_{p}) when $\delta = 40\ \mu m$ and $\varepsilon_{\mathrm{s}} = 0.16$.

5.3.4 Experimental validation of the simulation data

Experiments were performed to verify the simulation results. **Figure 5-14** shows the changes of q_{Li^+} and W_{net} according to r_{p} by experiment and simulation. In both figures (**Figure 5-14a** and **Figure 5-14b**), r_{p} and q_{Li^+} show negative correlations, and r_{p} and W_{net} show positive correlations. In other words, it shows that the simulation results reflect the experimental tendency well in the change of r_{p}. Note that there are differences between the absolute values of the experimental and simulation results, which is because r_{p} could not be controlled small and constant in the real world as the simulation.

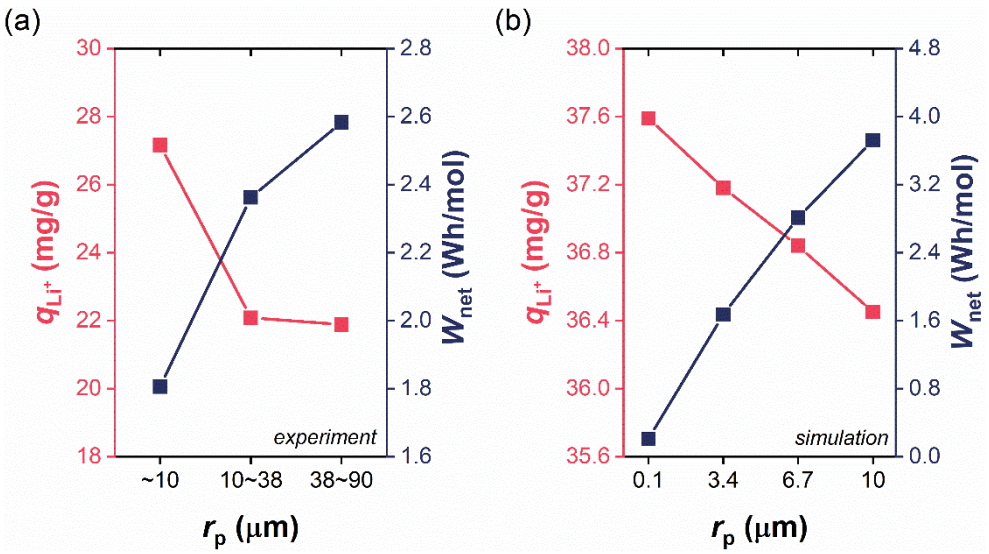

Figure 5-14 Variation of the specific mass of Li^+ recovered (q_{Li^+}) and the net energy consumption (W_{net}) with effective radius of LMO particle (r_p) in (a) experiments and (b) simulations

5.3.5 Sensitivity analysis of the electrode design parameters

A sensitivity analysis is performed to investigate the significance of the electrode design parameters on the ELR system performance. A three-dimensional interpolation is employed to evaluate $q_{\mathrm{Li^+}}$ and W_{net} at any specific combination of $\{r_{\mathrm{p}}, \varepsilon_{\mathrm{s}}, \delta\}$. **Figure 5-15** summarizes the dependence of $q_{\mathrm{Li^+}}$ and W_{net} on the design parameters (for global and local sensitivity analysis results, see **Figure 5-16** to **Figure 5-18**). $q_{\mathrm{Li^+}}$ and W_{net} are respectively normalized by $q_{\mathrm{Li^+,max}}$ (= 38.33 mg/g), the theoretical maximum value of $q_{\mathrm{Li^+}}$, and $W_{\mathrm{net,ref}}$ (= 1.0 Wh/mol), the reference energy consumption in the experimental ELR system (Lee et al. 2013). There are several aspects in these sensitivity plots, which can give us different insights: 1) the slope of average values (dotted lines), 2) the confidence intervals (shaded areas), and 3) the maximum and minimum values (solid lines).

From the dotted lines, it can be concluded that r_{p} is negatively correlated with $q_{\mathrm{Li^+}}$, while ε_{s} and δ are positively correlated with $q_{\mathrm{Li^+}}$, which is in line with **Figure 5-6**. It can be also seen that the slope of red dotted line is almost constant, meaning that r_{p} has equally strong effects on $q_{\mathrm{Li^+}}$ regardless of its value. The slope of green dotted line is quite small, implying that ε_{s} has weak

effects on q_{Li^+}. The blue dotted line tells us that δ has a strong impact on q_{Li^+} when it is small, which however diminishes as δ increases.

The shaded region corresponds to the region of possible values of q_{Li^+} as the design parameters change. The confidence interval is reduced as r_{p} decreases, and as ε_{s} or δ increases, which corresponds to the direction of increasing q_{Li^+}. The overall area of the shaded region in each plot is inversely proportional to the significance of each parameter's effect on q_{Li^+} value. It is again found that r_{p} and δ are slightly more influential than ε_{s} (see **Figure 5-16**, for global sensitivity analysis result). From the maximum lines in **Figure 5-15a**, it can be noted that the achievable maximum of q_{Li^+} is almost constant regardless of the values of ε_{s} and δ, while it decreases with increasing r_{p}, implying that r_{p} is more important than the other parameters to enhance q_{Li^+}.

Similar trends are identified in **Figure 5-15b**, which represents the sensitivity of W_{net} on the electrode design parameters. W_{net} is in a negative correlation with r_{p}, and is in a positive correlation with ε_{s} and δ, as found in **Figure 5-12**. The overall area of the shaded region in each plot is found to be similar, however, r_{p} and δ are again found to be slightly more influential than ε_{s}. It is also found that the confidence interval is reduced as r_{p} decreases, and

as ε_s or δ increases, which corresponds to the direction to decrease W_{net}. As found in the trend of q_{Li^+}, the minimum W_{net} achievable highly depends on r_p, while it is almost independent of ε_s or δ. In this regard, r_p is found to be the most influential parameter to minimize W_{net} (and to maximize q_{Li^+}).

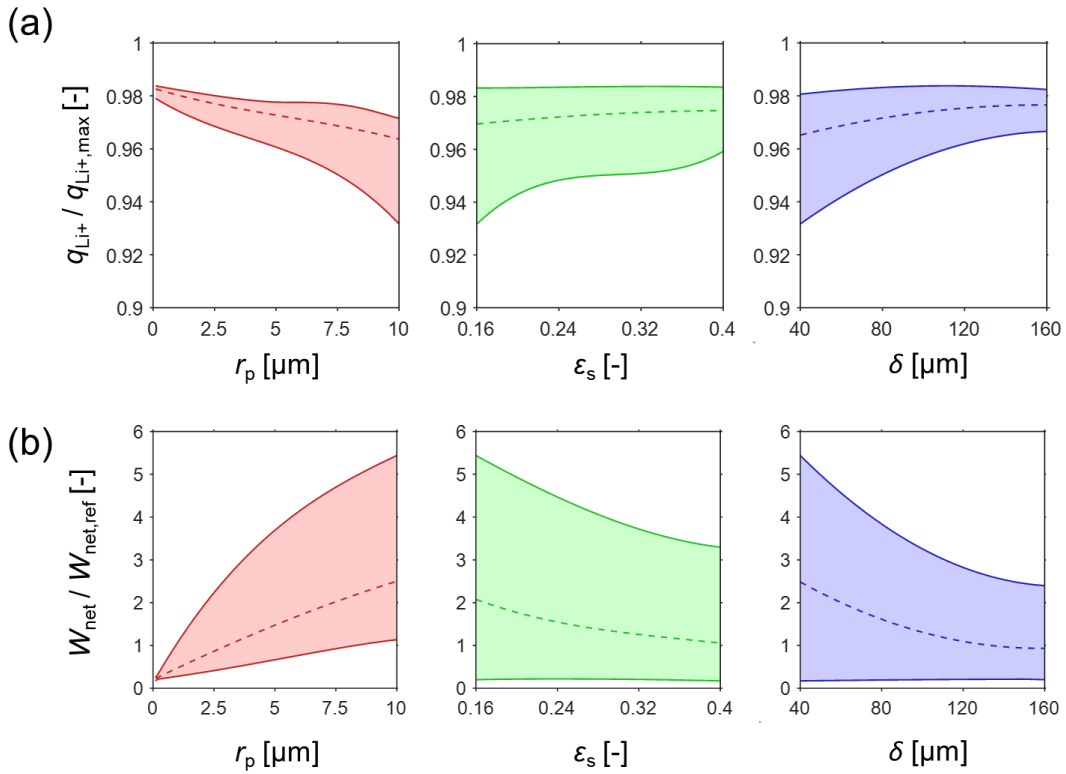

Figure 5-15 Sensitivity analysis results of (a) q_{Li^+} and (b) W_{net} on the electrode design parameters (r_{p}, ε_{s}, and δ). $q_{\mathrm{Li}^+,\mathrm{max}}$ (= 38.33 mg/g) is the theoretical maximum value of q_{Li^+}, and $W_{\mathrm{net,ref}}$ (= 1.0 Wh/mol) is the reference energy consumption in the experimental ELR system (Lee et al. 2013).

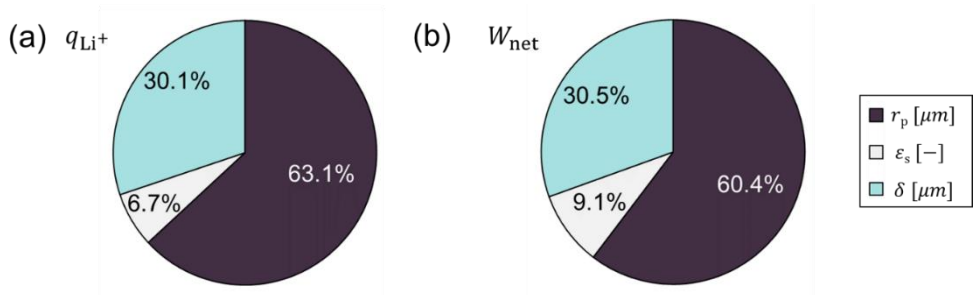

Figure 5-16 Global sensitivity analysis results of q_{Li^+} and W_{net} on each electrode design parameter

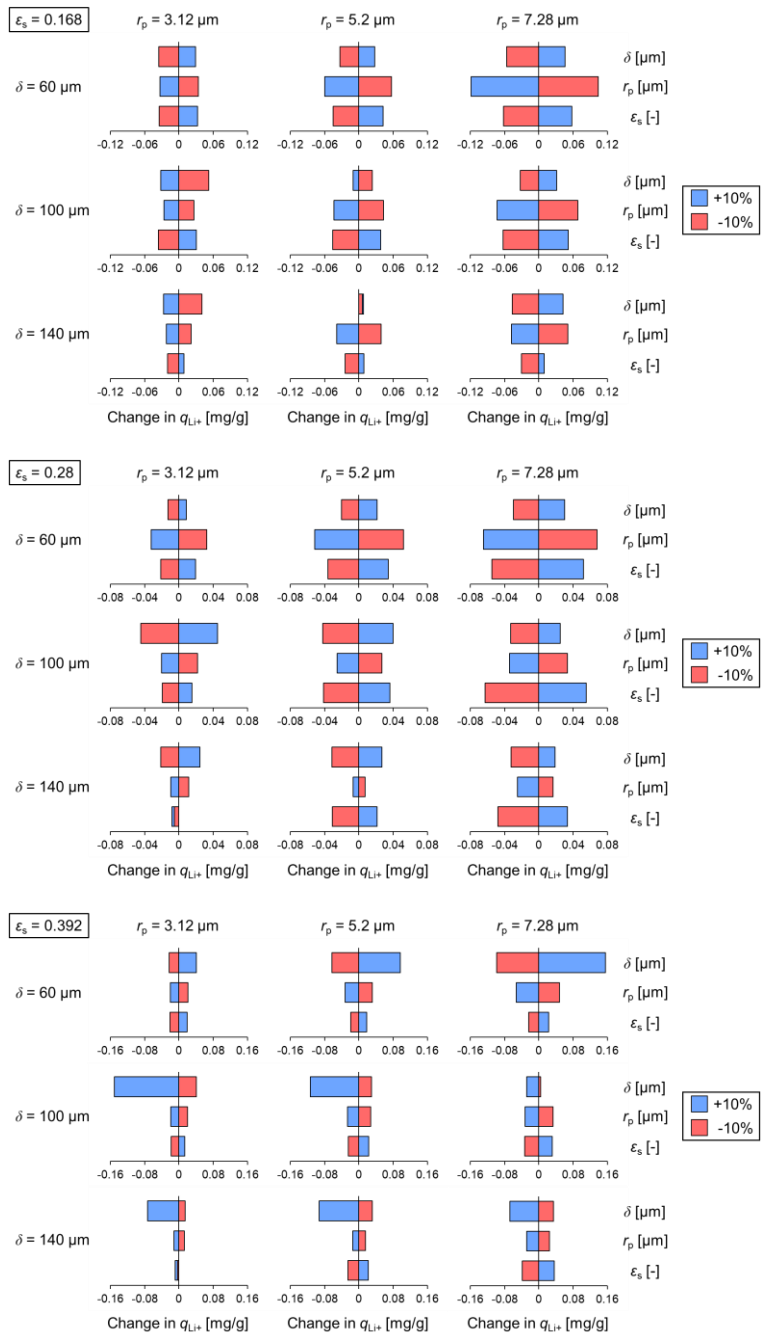

Figure 5-17 Local sensitivity analysis results of q_{Li^+} on each electrode design parameter

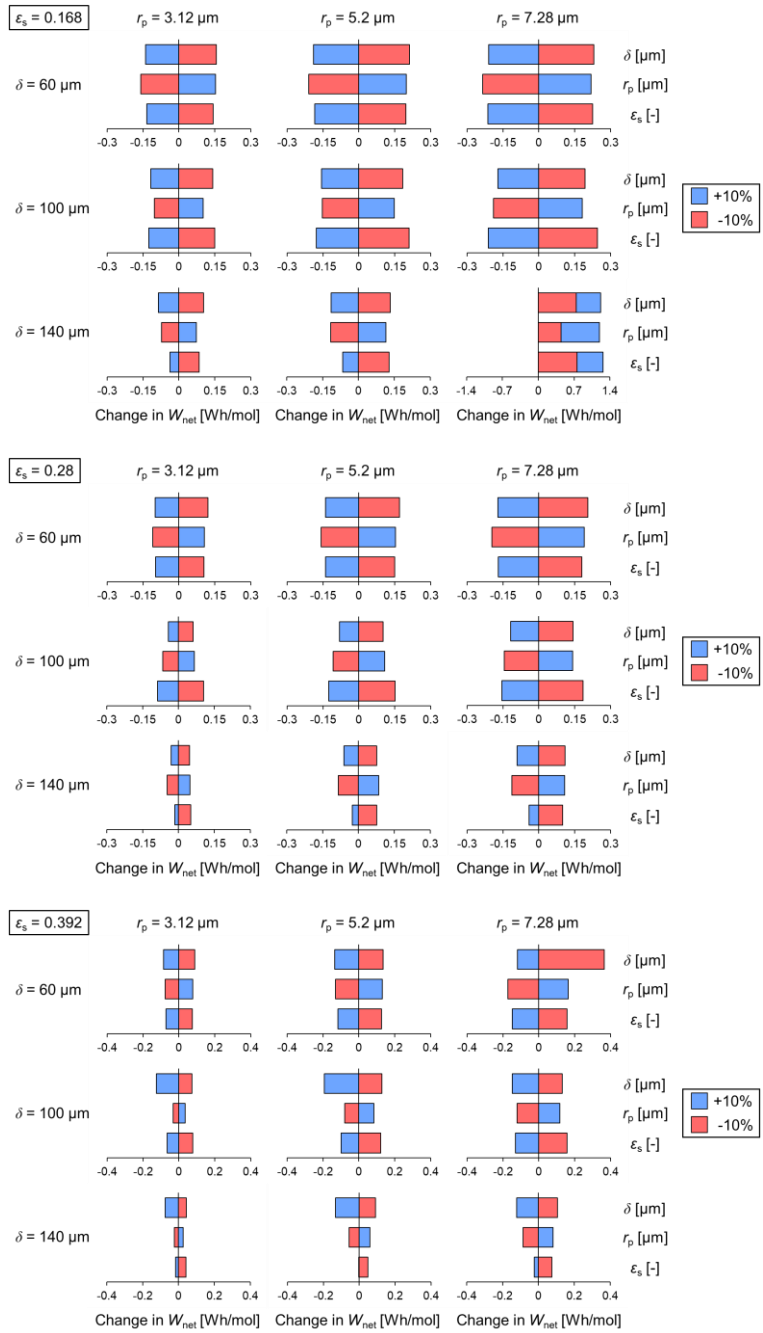

Figure 5-18 Local sensitivity analysis results of W_{net} on each electrode design parameter

5.4. Summary

The effect of electrode design parameters (r_p, ε_s, and δ) on the ELR system performance is numerically investigated in this study. The cell voltage profile and the intercalation/de-intercalation of Li^+ in the ELR system are successfully reproduced in the P2D model. The current density was fixed at a low value of $62.5\ \mu A/cm^2$ to allow the system to be operated in a near equilibrium state. The specific mass of Li^+ recovered (q_{Li^+}) and the net energy consumption (W_{net}) are affected by the combinations of electrode design parameters. q_{Li^+} is changed from 37.66 mg/g to 35.71 mg/g, while W_{net} is varied from 5.44 Wh/mol to 0.17 Wh/mol. As r_p increases $0.1\ \mu m$ to $10\ \mu m$, the system recovers less amount of Li^+, and requires more energy consumption. As either ε_s or δ increases, however, the amount of Li^+ recovered increases, and the system requires less energy consumption. These opposite correlations of electrode design parameters are explained with the Li^+ diffusion and the local current density applied to the LMO particle surface. As r_p increases, the time required to fully saturate an LMO particle by the Li^+ diffusion increases, which leads to a charge/discharge step is terminated before the saturation of the LMO particle. The local current density, proportional to r_p and inversely proportional to ε_s and δ, is correlated with

the amount of overpotential in the electrochemical reaction. As the local current density increases, a high level of overpotential is formed and the ELR system performance is degraded even though the current applied to the electrode is identical. The sensitivity analysis is also performed to assess the significance of each design parameter on the ELR system performance. It is found that r_{p} is needed to be kept as small as possible to minimize the effects of the other parameters on the system performance, i.e., for the robustness of the system performance. Since the results provided in this study are only applicable to a low current density regime, the effect of electrode design parameters at a high current density condition will be covered in the future study for a more comprehensive understanding of ELR systems.

6. Conclusion and perspectives

In this dissertation, the continuous ELR systems were developed by two ways.

First, a pilot-scale ELR system including a unit CSTR process was designed and demonstrated. To design industrially feasible systems a mobile-type electrode configuration was developed. The system was successfully demonstrated in the actual seawater desalination plant and treated 6 tons of desalination concentrate per day. From the results of the trial run of the system, a Li^+ was enriched 1800 times that of desalination concentrate, and the final product was 88.0% pure.

Next, an LMO-based flow-type rocking-chair ELR was developed, and a numerical simulation was conducted for understanding system behavior. The data from the numerical simulation was well fitted with experimentally measured data. Spatiotemporal concentration and voltage distribution can be identified from simulation results, which is a useful tool for understanding phenomena in flow-type ELR systems. In addition, the effect of electrode design parameters on the performance indicator of a flow-type ELR system was investigated by numerical simulation. The amount of Li^+ recovered increased with the increment of ε_s and δ and the decrement of r_p, and the

energy consumption showed the opposite trend. By the sensitivity analysis, it was revealed that the most decisive parameter that determines the performance is r_p among the three design parameters.

In conclusion, this dissertation shows the successful transition of ELR into continuous systems and the possibility of industrial application. The engineering design methods developed in this study will improve ELR's technical maturity and help the commercialization of the ELR system.

Future ELR systems are expected to be developed and researched as follows. First, various types of continuous flow-type reactors will be studied. In addition to the flow-by method studied in this study, there are flow-through and pack bed methods. Depending on the brine conditions and operating conditions, a method advantageous to lithium extraction can be selected differently. Considering that continuous flow-type research in the ELR system has been conducted since 2020, including this study, it is still in the early stages of research, so there is room for various studies.

Next, it is expected that various applications of ELR technology to treat various brine resource will be attempted. Decentralized facilities based on electrochemistry can be applied economically even in small-scale processes, and ELR technology has a unique high lithium selectivity compared to competing technologies. Because of these two advantages, ELR can be

applied as a niche technology in undeveloped brine that cannot be exploited by the conventional lime soda evaporation method. In other words, it is possible to expand the range of lithium resources that can be mined. This study also confirmed that lithium can be recovered from the desalination concentrate under extreme conditions. Therefore, it is expected that ELR technology can be effectively applied to various undeveloped aqueous lithium resources, not only lithium brine with high Li^+ concentration. In addition, the possibility of recovering lithium using ELR technology from waste lithium-ion batteries should be examined.

ELR research, which is variously combined with computer-aided engineering, is also expected to increase. Applicable computer-aided engineering is limitless, including the computational simulation performed in this study, the DFT technique for electrode material research, and the AI technique for predicting the performance of ELR technology in various brine compositions. Combining with digital technology will further promote the development of ELR technology.

ELR technology should also be studied in relation to carbon neutrality. Although ELR technology is expected to be more environmentally friendly than other competing technologies, there is no research that has been analyzed through sophisticated life cycle assessment (LCA) techniques. In the future,

environmental regulations will become more stringent around the world. If eco-friendly characteristic of ELR technology is emphasized, this technology will emerge as a promising next-generation lithium recovery technology.

Finally, the ELR system treating the actual lithium brine such as Salar de Atacama should be scaled up. So far, there has been no research case where a large-scale ELR system has been applied to recover lithium from a brine. If such research is done, high technological maturity will be secured and it will be able to lead the next generation of lithium recovery technology, which currently has no clear winner.

7. References

Abu Qdais H (2008) Environmental impacts of the mega desalination project: the Red–Dead Sea conveyor. Desalination 220:16–23. https://doi.org/10.1016/j.desal.2007.01.019

Agudosi ES, Abdullah EC, Numan A, et al (2021) Optimisation of NiO electrodeposition on 3D graphene electrode for electrochemical energy storage using response surface methodology. Journal of Electroanalytical Chemistry 882:. https://doi.org/10.1016/j.jelechem.2021.114992

Battistel A, Palagonia MS, Brogioli D, et al (2020) Electrochemical Methods for Lithium Recovery: A Comprehensive and Critical Review. Advanced Materials 32

Cabello J (2021) Lithium brine production, reserves, resources and exploration in Chile: An updated review. Ore Geol Rev 128:103883. https://doi.org/https://doi.org/10.1016/j.oregeorev.2020.103883

Calisaya-Azpilcueta D, Herrera-Leon S, Cisternas LA (2020) Current and Future Global Lithium Production Till 2025. The Open Chemical Engineering Journal 14:36–51. https://doi.org/10.2174/1874123102014010036

Calvo EJ (2021) Direct Lithium Recovery from Aqueous Electrolytes with Electrochemical Ion Pumping and Lithium Intercalation. ACS Omega 6:35213–35220. https://doi.org/10.1021/acsomega.1c05516

Calvo EJ (2019) Electrochemical methods for sustainable recovery of lithium from natural brines and battery recycling. Curr Opin Electrochem 15:102–108

Chen JM (2021) Carbon neutrality: Toward a sustainable future. Innovation(China) 2

Chiang F, Mazdiyasni O, AghaKouchak A (2021) Evidence of anthropogenic impacts on global drought frequency, duration, and intensity. Nat Commun 12:. https://doi.org/10.1038/s41467-021-22314-w

Chitrakar R, Kanoh H, Miyai Y, Ooi K (2001) Recovery of Lithium from Seawater Using Manganese Oxide Adsorbent (H1.6Mn1.6O4) Derived from Li1.6Mn1.6O4. Ind Eng Chem Res 40:2054–2058. https://doi.org/10.1021/ie000911h

Chordia M, Wickerts S, Nordelöf A, Arvidsson R (2022) Life cycle environmental impacts of current and future battery-grade lithium supply from brine and spodumene. Resour Conserv Recycl 187:106634. https://doi.org/https://doi.org/10.1016/j.resconrec.2022.106634

Choubey PK, Chung K-S, Kim M, et al (2017) Advance review on the exploitation of the prominent energy-storage element Lithium. Part II: From sea water and spent lithium ion batteries (LIBs). Miner Eng 110:104–121. https://doi.org/https://doi.org/10.1016/j.mineng.2017.04.008

Chung K-S, Lee J-C, Kim W-K, et al (2008) Inorganic adsorbent containing polymeric membrane reservoir for the recovery of lithium from seawater. J Memb Sci 325:503–508. https://doi.org/https://doi.org/10.1016/j.memsci.2008.09.041

COMSOL Inc. (2012) Batteries & Fuel Cells Module User's Guide

Corcoran E (2010) Sick water?: the central role of wastewater management in sustainable development: a rapid response assessment. UNEP/Earthprint

Cui X, Feng H, Xue Y, et al (2017) Convenient synthesis and electrochemical performance investigation of nano-sized LiMn2O4. Journal of Materials Science: Materials in Electronics 28:8529–8536. https://doi.org/10.1007/s10854-017-6575-5

Devan S, Subramanian VR, White RE (2004) Analytical solution for the impedance of a porous electrode. J Electrochem Soc 151:A905

Doyle M, Fuller TF, Newman J (1993) Modeling of Galvanostatic Charge and Discharge of the Lithium/Polymer/Insertion Cell. J Electrochem Soc 140:1526–1533. https://doi.org/10.1149/1.2221597

Du X, Guan G, Li X, et al (2016) A novel electroactive λ-MnO2/PPy/PSS core-shell nanorod coated electrode for selective recovery of lithium ions at low concentration. J Mater Chem A Mater 4:13989–13996. https://doi.org/10.1039/c6ta05985f

Elimelech M, Phillip WA (2011) The Future of Seawater Desalination: Energy, Technology, and the Environment. Science (1979) 333:712–717. https://doi.org/10.1126/science.1200488

Ericksen GE, Vine JD, Raul Ballón A (1978) Chemical composition and distribution of lithium-rich brines in salar de Uyuni and nearby salars in southwestern Bolivia. Energy 3:355–363. https://doi.org/10.1016/0360-5442(78)90032-4

Fang JW, Wang J, Ji ZY, et al (2022) Establishment of PPy-derived carbon encapsulated LiMn2O4 film electrode and its performance for efficient Li+ electrosorption. Sep Purif Technol 280:. https://doi.org/10.1016/j.seppur.2021.119726

Fankhauser S, Smith SM, Allen M, et al (2022) The meaning of net zero and how to get it right. Nat Clim Chang 12:15–21

Feng Q, Miyai Y, Kanoh H, Ooi K (1992) Li+ Extraction/Insertion with Spinel-Type Lithium Manganese Oxides. Characterization of Redox-Type and Ion-Exchange-Type Sites. Langmuir 8:1861–1867. https://doi.org/10.1021/la00043a029

Flexer V, Baspineiro CF, Galli CI (2018) Lithium recovery from brines: A vital raw material for green energies with a potential environmental impact in its mining and processing. Science of The Total Environment 639:1188–1204. https://doi.org/https://doi.org/10.1016/j.scitotenv.2018.05.223

Fukuda H (2019) Lithium extraction from brine with ion exchange resin and ferric phosphate

Fukuda H, Eng B (2019) LITHIUM EXTRACTION FROM BRINE WITH ION EXCHANGE RESIN AND FERRIC PHOSPHATE

Fuller TF (1994) Simulation and Optimization of the Dual Lithium Ion Insertion Cell. J Electrochem Soc 141:1. https://doi.org/10.1149/1.2054684

Gerlach SA (1981) Marine Pollution. Springer Berlin Heidelberg, Berlin,

Heidelberg

Ghaffour N, Missimer TM, Amy GL (2013) Technical review and evaluation of the economics of water desalination: Current and future challenges for better water supply sustainability. Desalination 309:197–207. https://doi.org/10.1016/J.DESAL.2012.10.015

Ghosh A (2020) Possibilities and challenges for the inclusion of the electric vehicle (EV) to reduce the carbon footprint in the transport sector: A review. Energies (Basel) 13:. https://doi.org/10.3390/en13102602

Giwa A, Dufour V, Marzooqi F Al, et al (2017) Brine management methods: Recent innovations and current status. Desalination 407:1–23. https://doi.org/https://doi.org/10.1016/j.desal.2016.12.008

Greedan JE, Raju NP, Wills AS, et al (1998) Structure and Magnetism in λ-MnO_2 . Geometric Frustration in a Defect Spinel. Chemistry of Materials 10:3058–3067. https://doi.org/10.1021/cm9801789

Gu B, Adjiman CS, Xu XY (2017) The effect of feed spacer geometry on membrane performance and concentration polarisation based on 3D CFD simulations. J Memb Sci 527:78–91. https://doi.org/10.1016/j.memsci.2016.12.058

Guo ZY, Ji ZY, Chen HY, et al (2020) Effect of Impurity Ions in the Electrosorption Lithium Extraction Process: Generation and Restriction of “Selective Concentration Polarization.” ACS Sustain Chem Eng 8:11834–11844. https://doi.org/10.1021/acssuschemeng.0c04359

Hawks SA, Ramachandran A, Porada S, et al (2019) Performance metrics for the objective assessment of capacitive deionization systems. Water Res 152:126–137. https://doi.org/10.1016/j.watres.2018.10.074

He L, Xu W, Song Y, et al (2018) Lithium-Ion Batteries: New Insights into the Application of Lithium-Ion Battery Materials: Selective Extraction of Lithium from Brines via a Rocking-Chair Lithium-Ion Battery System (Global Challenges 2/2018). Global Challenges 2:1870020. https://doi.org/10.1002/gch2.201870020

Hoekstra AY, Mekonnen MM, Chapagain AK, et al (2012) Global Monthly Water Scarcity: Blue Water Footprints versus Blue Water Availability. PLoS One 7:e32688. https://doi.org/10.1371/journal.pone.0032688

Hoshino T (2013a) Preliminary studies of lithium recovery technology from seawater by electrodialysis using ionic liquid membrane. Desalination 317:11–16. https://doi.org/https://doi.org/10.1016/j.desal.2013.02.014

Hoshino T (2015) Innovative lithium recovery technique from seawater by using world-first dialysis with a lithium ionic superconductor. Desalination 359:59–63. https://doi.org/https://doi.org/10.1016/j.desal.2014.12.018

Hoshino T (2013b) Development of technology for recovering lithium from seawater by electrodialysis using ionic liquid membrane. Fusion Engineering and Design 88:2956–2959. https://doi.org/https://doi.org/10.1016/j.fusengdes.2013.06.009

How YY, Bibi F, Numan A, et al (2022) Fabrication of binary metal phosphate-

based binder-free electrode for new generation energy storage device. Surf Coat Technol 429:. https://doi.org/10.1016/j.surfcoat.2021.127924

Huggins R (2008) Advanced batteries: materials science aspects. Springer Science & Business Media

International Desalination Association (2019) Dynamic growth for desalination and water reuse in 2019. IDA In the News 15

Jang Y, Hou CH, Park S, et al (2021) Direct electrochemical lithium recovery from acidic lithium-ion battery leachate using intercalation electrodes. Resour Conserv Recycl 175:. https://doi.org/10.1016/j.resconrec.2021.105837

JOGMEC (2010) Metal Resources Report, Current Situation of Lithium Resources

Jokar A, Rajabloo B, Désilets M, Lacroix M (2016) Review of simplified Pseudo-two-Dimensional models of lithium-ion batteries. J Power Sources 327:44–55. https://doi.org/10.1016/j.jpowsour.2016.07.036

Joo H, Jung SY, Kim S, et al (2020a) Application of a Flow-Type Electrochemical Lithium Recovery System with λ-MnO2/LiMn2O4: Experiment and Simulation. ACS Sustain Chem Eng 8:9622–9631. https://doi.org/10.1021/acssuschemeng.9b07427

Joo H, Lee J, Yoon J (2020b) Short review: Timeline of the electrochemical lithium recovery system using the spinel LIMN2o4 as a positive electrode. Energies (Basel) 13:. https://doi.org/10.3390/en13236235

Joo H, Yoon JY (2022) Basic Concept of Carbon Neutral Engineering in the Chemical Industry to Overcome the Climate Crisis. Korean Industrial Chemistry News 25:34–39

Jung SY, Ahn KH, Kang TG, et al (2018) Chaotic mixing in a barrier-embedded partitioned pipe mixer. AIChE Journal 64:717–729. https://doi.org/10.1002/aic.15929

Kang J, Kim T, Shin H, et al (2016) Direct energy recovery system for membrane capacitive deionization. Desalination 398:144–150. https://doi.org/10.1016/J.DESAL.2016.07.025

Kanoh H, Ooi K, Miyai Y, Katoh S (1993) Electrochemical recovery of lithium ions in the aqueous phase. In: Separation Science and Technology. pp 643–651

Kanoh H, Ooi K, Miyai Y, Katoh S (1991) Selective Electroinsertion of Lithium Ions into a Pt/λ-MnO2Electrode in the Aqueous Phase. Langmuir 7:1841–1842. https://doi.org/10.1021/la00057a002

Khalil A, Mohammed S, Hashaikeh R, Hilal N (2022) Lithium recovery from brine: Recent developments and challenges. Desalination 528:115611. https://doi.org/https://doi.org/10.1016/j.desal.2022.115611

Kim DH (2011) A review of desalting process techniques and economic analysis of the recovery of salts from retentates. Desalination 270:1–8. https://doi.org/https://doi.org/10.1016/j.desal.2010.12.041

Kim JS, Lee YH, Choi S, et al (2015a) An Electrochemical Cell for Selective

Lithium Capture from Seawater. Environ Sci Technol 49:9415–9422. https://doi.org/10.1021/acs.est.5b00032

Kim S, Joo H, Moon T, et al (2019) Rapid and selective lithium recovery from desalination brine using an electrochemical system. Environ Sci Process Impacts 21:667–676. https://doi.org/10.1039/c8em00498f

Kim S, Kang JS, Joo H, et al (2020) Understanding the Behaviors of λ-MnO2in Electrochemical Lithium Recovery: Key Limiting Factors and a Route to the Enhanced Performance. Environ Sci Technol 54:9044–9051. https://doi.org/10.1021/acs.est.9b07646

Kim S, Kim J, Kim S, et al (2018a) Electrochemical lithium recovery and organic pollutant removal from industrial wastewater of a battery recycling plant. Environ Sci (Camb) 4:175–182. https://doi.org/10.1039/c7ew00454k

Kim S, Lee J, Kang JS, et al (2015b) Lithium recovery from brine using a λ-MnO2/activated carbon hybrid supercapacitor system. Chemosphere 125:50–56. https://doi.org/10.1016/j.chemosphere.2015.01.024

Kim S, Lee J, Kim S, et al (2018b) Electrochemical Lithium Recovery with a LiMn2O4–Zinc Battery System using Zinc as a Negative Electrode. Energy Technology 6:340–344. https://doi.org/10.1002/ente.201700488

Lattemann S, Höpner T (2008) Environmental impact and impact assessment of seawater desalination. Desalination 220:1–15. https://doi.org/10.1016/J.DESAL.2007.03.009

Lawagon CP, Nisola GM, Cuevas RAI, et al (2018) Li1−xNi0.33Co1/3Mn1/3O2/Ag for electrochemical lithium recovery from brine. Chemical Engineering Journal 348:1000–1011. https://doi.org/10.1016/j.cej.2018.05.030

Lawagon CP, Nisola GM, Cuevas RAI, et al (2019) Li1−xNi0.5Mn1.5O4/Ag for electrochemical lithium recovery from brine and its optimized performance via response surface methodology. Sep Purif Technol 212:416–426. https://doi.org/10.1016/j.seppur.2018.11.046

Lee CW (2006) Effect of Binary Conductive Agents in Spinel LiMn 2 O 4 Cathodes on Electrochemical Performance of Li-ion Batteries

Lee J, Yu SH, Kim C, et al (2013) Highly selective lithium recovery from brine using a λ-MnO 2-Ag battery. Physical Chemistry Chemical Physics 15:7690–7695. https://doi.org/10.1039/c3cp50919b

Liu D, Gao X, An H, et al (2019) Supply and demand response trends of lithium resources driven by the demand of emerging renewable energy technologies in China. Resour Conserv Recycl 145:311–321. https://doi.org/10.1016/j.resconrec.2019.02.043

Liu S, Smith KC (2018) Quantifying the trade-offs between energy consumption and salt removal rate in membrane-free cation intercalation desalination. Electrochim Acta 271:652–665. https://doi.org/10.1016/j.electacta.2018.03.065

Liu W, Kowal K, Farrington GC (1998) Mechanism of the Electrochemical

Insertion of Lithium into LiMn2 O 4 Spinels. J Electrochem Soc 145:459–465. https://doi.org/10.1149/1.1838285

Liu X, Chen X, Zhao Z, Liang X (2014) Effect of Na+ on Li extraction from brine using LiFePO 4/FePO4 electrodes. Hydrometallurgy 146:24–28. https://doi.org/10.1016/j.hydromet.2014.03.010

Magnan AK, Pörtner HO, Duvat VKE, et al (2021) Estimating the global risk of anthropogenic climate change. Nat Clim Chang 11:879–885. https://doi.org/10.1038/s41558-021-01156-w

Maljuric S, Jud W, Kappe CO, Cantillo D (2020) Translating batch electrochemistry to single-pass continuous flow conditions: an organic chemist's guide. J Flow Chem 10:181–190. https://doi.org/10.1007/s41981-019-00050-z

Marchini F, Calvo EJ, Williams FJ (2018a) Effect of the electrode potential on the surface composition and crystal structure of LiMn2O4 in aqueous solutions. Electrochim Acta 269:706–713. https://doi.org/10.1016/j.electacta.2018.02.108

Marchini F, Rubi D, del Pozo M, et al (2016) Surface Chemistry and Lithium-Ion Exchange in LiMn2O4 for the Electrochemical Selective Extraction of LiCl from Natural Salt Lake Brines. Journal of Physical Chemistry C 120:15875–15883. https://doi.org/10.1021/acs.jpcc.5b11722

Marchini F, Williams FJ, Calvo EJ (2018b) Electrochemical impedance spectroscopy study of the LixMn2O4 interface with natural brine. Journal of Electroanalytical Chemistry 819:428–434. https://doi.org/10.1016/j.jelechem.2017.11.071

Marchini F, Williams FJ, Calvo EJ (2018c) Sustainable selective extraction of lithium chloride from natural brine using a Li 1-x Mn 2 O 4 ion pump. J Electrochem Soc 165:A3292–A3298. https://doi.org/10.1149/2.0291814jes

Martin G, Rentsch L, Höck M, Bertau M (2017) Lithium market research – global supply, future demand and price development. Energy Storage Mater 6:171–179. https://doi.org/10.1016/j.ensm.2016.11.004

Meinshausen M, Lewis J, McGlade C, et al (2022) Realization of Paris Agreement pledges may limit warming just below 2 °C. Nature 604:304–309. https://doi.org/10.1038/s41586-022-04553-z

Meshram P, Pandey BD, Mankhand TR (2014) Extraction of lithium from primary and secondary sources by pre-treatment, leaching and separation: A comprehensive review. Hydrometallurgy 150:192–208. https://doi.org/https://doi.org/10.1016/j.hydromet.2014.10.012

Missimer TM, Maliva RG (2018) Environmental issues in seawater reverse osmosis desalination: Intakes and outfalls. Desalination 434:198–215. https://doi.org/10.1016/J.DESAL.2017.07.012

Missoni LL, Marchini F, del Pozo M, Calvo EJ (2016) A LiMn 2 O 4 -Polypyrrole System for the Extraction of LiCl from Natural Brine . J Electrochem Soc 163:A1898–A1902. https://doi.org/10.1149/2.0591609jes

Morillo J, Usero J, Rosado D, et al (2014) Comparative study of brine management technologies for desalination plants. Desalination 336:32–49. https://doi.org/https://doi.org/10.1016/j.desal.2013.12.038

Niu J, Yan W, Song X, et al (2021) An electrically switched ion exchange system with self-electrical-energy recuperation for efficient and selective LiCl separation from brine lakes. Sep Purif Technol 274:. https://doi.org/10.1016/j.seppur.2021.118995

Ooi K, Miyai Y, Katoh S, et al (1989) Topotactic Li+Insertion to λ-MnO2in the Aqueous Phase. Langmuir 5:150–157. https://doi.org/10.1021/la00085a028

Ooi K, Miyai Y, Katoh S, et al (1988) Lithium-ion Insertion/Extraction Reaction with λ-MnO 2 in the Aqueous Phase . Chem Lett 17:989–992. https://doi.org/10.1246/cl.1988.989

Ooi K, Miyai Y, Sakakihara J (1991) Mechanism of Li Insertion in Spinel-Type Manganese Oxide. Redox and Ion-Exchange Reactions. Langmuir 7:1167–1171. https://doi.org/10.1021/la00054a025

Palagonia MS, Brogioli D, la Mantia F (2019) Effect of Current Density and Mass Loading on the Performance of a Flow-Through Electrodes Cell for Lithium Recovery. J Electrochem Soc 166:E286–E292. https://doi.org/10.1149/2.0221910jes

Palagonia MS, Brogioli D, la Mantia F (2020) Lithium recovery from diluted brine by means of electrochemical ion exchange in a flow-through-electrodes cell. Desalination 475:. https://doi.org/10.1016/j.desal.2019.114192

Palagonia MS, Brogioli D, Mantia FL (2017) Influence of Hydrodynamics on the Lithium Recovery Efficiency in an Electrochemical Ion Pumping Separation Process. J Electrochem Soc 164:E586–E595. https://doi.org/10.1149/2.1531714jes

Panagopoulos A, Haralambous K-J, Loizidou M (2019) Desalination brine disposal methods and treatment technologies - A review. Science of The Total Environment 693:. https://doi.org/10.1016/j.scitotenv.2019.07.351

Park J, Willenbacher N, Ahn KH (2019) How the interaction between styrene-butadiene-rubber (SBR) binder and a secondary fluid affects the rheology, microstructure and adhesive properties of capillary-suspension-type graphite slurries used for Li-ion battery anodes. Colloids Surf A Physicochem Eng Asp 579:123692. https://doi.org/10.1016/j.colsurfa.2019.123692

Pasta M, Battistel A, la Mantia F (2012) Batteries for lithium recovery from brines. Energy Environ Sci 5:9487–9491. https://doi.org/10.1039/c2ee22977c

Porada S, Shrivastava A, Bukowska P, et al (2017) Nickel Hexacyanoferrate Electrodes for Continuous Cation Intercalation Desalination of Brackish Water. Electrochim Acta 255:369–378. https://doi.org/10.1016/j.electacta.2017.09.137

Pramanik BK, Asif MB, Roychand R, et al (2020) Lithium recovery from salt-lake brine: Impact of competing cations, pretreatment and preconcentration. Chemosphere 260:127623. https://doi.org/10.1016/j.chemosphere.2020.127623

Qu Y, Campbell PG, Gu L, et al (2016) Energy consumption analysis of constant voltage and constant current operations in capacitive deionization. Desalination

400:18–24. https://doi.org/https://doi.org/10.1016/j.desal.2016.09.014

Ramadesigan V, Northrop PWC, De S, et al (2012) Modeling and Simulation of Lithium-Ion Batteries from a Systems Engineering Perspective. J Electrochem Soc 159:R31–R45. https://doi.org/10.1149/2.018203jes

Ramazanov MA, Maharramov AM, Shirinova HA, Palma L di (2018) Structure and electrophysical properties of polyvinylidene fluoride (PVDF)/magnetite nanocomposites. Journal of Thermoplastic Composite Materials 33:138–149. https://doi.org/10.1177/0892705718796542

Ravikumar B, Mynam M, Rai B (2018) Effect of Salt Concentration on Properties of Lithium Ion Battery Electrolytes: A Molecular Dynamics Study. Journal of Physical Chemistry C 122:8173–8181. https://doi.org/10.1021/acs.jpcc.8b02072

Reale ER, Shrivastava A, Smith KC (2019) Effect of conductive additives on the transport properties of porous flow-through electrodes with insulative particles and their optimization for Faradaic deionization. Water Res 165:114995. https://doi.org/10.1016/j.watres.2019.114995

Rock MT (1998) Freshwater Use, Freshwater Scarcity, and Socioeconomic Development. J Environ Dev 7:278–301. https://doi.org/10.1177/107049659800700304

Romero VCE, Llano K, Calvo EJ (2021a) Electrochemical extraction of lithium by ion insertion from natural brine using a flow-by reactor: Possibilities and limitations. Electrochem commun 125:. https://doi.org/10.1016/j.elecom.2021.106980

Romero VCE, Putrino DS, Tagliazucchi M, et al (2020) Electrochemical Flow Reactor for Selective Extraction of Lithium Chloride from Natural Brines. J Electrochem Soc 167:120522. https://doi.org/10.1149/1945-7111/abace8

Romero VCE, Putrino DS, Tagliazucchi M, et al (2021b) Sustainable Electrochemical Extraction of Lithium from Natural Brine: Part II. Flow Reactor. J Electrochem Soc 168:020518. https://doi.org/10.1149/1945-7111/abde81

Romero VCE, Tagliazucchi M, Flexer V, Calvo EJ (2018) Sustainable Electrochemical Extraction of Lithium from Natural Brine for Renewable Energy Storage. J Electrochem Soc 165:A2294–A2302. https://doi.org/10.1149/2.0741810jes

Rousi E, Kornhuber K, Beobide-Arsuaga G, et al (2022) Accelerated western European heatwave trends linked to more-persistent double jets over Eurasia. Nat Commun 13:3851. https://doi.org/10.1038/s41467-022-31432-y

Schilcher C, Meyer C, Kwade A (2016) Structural and electrochemical properties of calendered lithium manganese oxide cathodes. Energy Technology 4:1604–1610

Shahmansouri A, Min J, Jin L, Bellona C (2015) Feasibility of extracting valuable minerals from desalination concentrate: A comprehensive literature review. J Clean Prod 100:4–16. https://doi.org/10.1016/j.jclepro.2015.03.031

Shang X, Hu B, Nie P, et al (2021) LiNi0.5Mn1.5O4-based hybrid capacitive deionization for highly selective adsorption of lithium from brine. Sep Purif Technol 258:. https://doi.org/10.1016/j.seppur.2020.118009

Singh K, Bouwmeester HJM, de Smet LCPM, et al (2018) Theory of Water Desalination with Intercalation Materials. Phys Rev Appl 9:. https://doi.org/10.1103/PhysRevApplied.9.064036

Singh K, Porada S, de Gier HD, et al (2019) Timeline on the application of intercalation materials in Capacitive Deionization. Desalination 455:115–134. https://doi.org/10.1016/j.desal.2018.12.015

Smith KC (2017) Theoretical evaluation of electrochemical cell architectures using cation intercalation electrodes for desalination. Electrochim Acta 230:333–341. https://doi.org/10.1016/j.electacta.2017.02.006

Smith KC, Dmello R (2016) Na-Ion Desalination (NID) Enabled by Na-Blocking Membranes and Symmetric Na-Intercalation: Porous-Electrode Modeling. J Electrochem Soc 163:A530–A539. https://doi.org/10.1149/2.0761603jes

Smith RB, Bazant MZ (2017) Multiphase porous electrode theory. J Electrochem Soc 164:E3291

Song JF, Nghiem LD, Li X-M, He T (2017) Lithium extraction from Chinese salt-lake brines: opportunities, challenges, and future outlook. Environ Sci (Camb) 3:593–597. https://doi.org/10.1039/C7EW00020K

Srimuk P, Su X, Yoon J, et al (2020) Charge-transfer materials for electrochemical water desalination, ion separation and the recovery of elements. Nat Rev Mater 5:517–538

Sun X, Hao H, Zhao F, Liu Z (2017) Tracing global lithium flow: A trade-linked material flow analysis. Resour Conserv Recycl 124:50–61. https://doi.org/10.1016/j.resconrec.2017.04.012

Sung SH, Kim DH, Kim S, et al (2019) Effect of neutralization of poly(acrylic acid) binder on the dispersion heterogeneity of Li-ion battery electrodes. J Mater Sci 54:13208–13220. https://doi.org/10.1007/s10853-019-03846-5

Tang A, Bao J, Skyllas-Kazacos M (2014) Studies on pressure losses and flow rate optimization in vanadium redox flow battery. J Power Sources 248:154–162. https://doi.org/10.1016/J.JPOWSOUR.2013.09.071

Tang C, Sprecher B, Tukker A, Mogollón JM (2021) The impact of climate policy implementation on lithium, cobalt and nickel demand: The case of the Dutch automotive sector up to 2040. Resources Policy 74:. https://doi.org/10.1016/j.resourpol.2021.102351

Trócoli R, Battistel A, La Mantia F (2015) Nickel Hexacyanoferrate as Suitable Alternative to Ag for Electrochemical Lithium Recovery. ChemSusChem 8:2514–2519. https://doi.org/https://doi.org/10.1002/cssc.201500368

Trócoli R, Battistel A, Mantia F la (2014) Selectivity of a lithium-recovery process based on LiFePO4. Chemistry - A European Journal 20:9888–9891. https://doi.org/10.1002/chem.201403535

Trócoli R, Bidhendi GK, Mantia F la (2016) Lithium recovery by means of electrochemical ion pumping: a comparison between salt capturing and selective

exchange. Journal of Physics: Condensed Matter 28:114005. https://doi.org/10.1088/0953-8984/28/11/114005

Trócoli R, Erinmwingbovo C, la Mantia F (2017) Optimized Lithium Recovery from Brines by using an Electrochemical Ion-Pumping Process Based on λ-MnO2 and Nickel Hexacyanoferrate. ChemElectroChem 4:143–149. https://doi.org/10.1002/celc.201600509

Turq P, Lantelme F, Chemla M (1969) Coefficients d'autodiffusion dans les solutions aqueuses de NaF ET NaCl. Electrochim Acta 14:1081–1088. https://doi.org/10.1016/0013-4686(69)80035-6

Ulrich RN (2022) When Texas went dark. Nat Rev Earth Environ 3:105–105. https://doi.org/10.1038/s43017-022-00267-y

Usta M, Morabito M, Anqi A, et al (2018) Twisted hollow fiber membrane modules for reverse osmosis-driven desalination. Desalination 441:21–34. https://doi.org/10.1016/j.desal.2018.04.027

Vikström H, Davidsson S, Höök M (2013) Lithium availability and future production outlooks. Appl Energy 110:252–266. https://doi.org/10.1016/J.APENERGY.2013.04.005

Vitagliano V, Lyons PA (1956) Diffusion coefficients for aqueous solutions of sodium chloride and barium chloride. J Am Chem Soc 78:1549–1552

Wang L, Frisella K, Srimuk P, et al (2021) Electrochemical lithium recovery with lithium iron phosphate: What causes performance degradation and how can we improve the stability? Sustain Energy Fuels 5:3124–3133. https://doi.org/10.1039/d1se00450f

Wang L, Meng C, Ma W (2009) Preparation of lithium ion-sieve and utilizing in recovery of lithium from seawater. Frontiers of Chemical Engineering in China 3:65–67. https://doi.org/10.1007/s11705-009-0105-9

Wanger TC (2011) The Lithium future-resources, recycling, and the environment. Conserv Lett 4:202–206. https://doi.org/10.1111/j.1755-263X.2011.00166.x

West K, Jacobsen T, Atlung S (1982) Modeling of Porous Insertion Electrodes with Liquid Electrolyte. J Electrochem Soc 129:1480–1485. https://doi.org/10.1149/1.2124188

Xiao JL, Sun SY, Wang J, et al (2013) Synthesis and adsorption properties of Li1.6Mn 1.6O4 spinel. Ind Eng Chem Res 52:11967–11973. https://doi.org/10.1021/ie400691d

Xie N, Li Y, Lu Y, et al (2020) Electrochemically Controlled Reversible Lithium Capture and Release Enabled by LiMn2O4 Nanorods. ChemElectroChem 7:105–111. https://doi.org/10.1002/celc.201901728

Xu P, Cath TY, Robertson AP, et al (2013) Critical review of desalination concentrate management, treatment and beneficial use. Environ Eng Sci 30:502–514. https://doi.org/10.1089/ees.2012.0348

Xu P, Hong J, Qian X, et al (2020) Materials for lithium recovery from salt lake brine. J Mater Sci. https://doi.org/10.1007/s10853-020-05019-1

Xu P, Hong J, Qian X, et al (2021) Materials for lithium recovery from salt lake brine. J Mater Sci 56:16–63

Xu X, Chen Y, Wan P, et al (2016) Extraction of lithium with functionalized lithium ion-sieves. Prog Mater Sci 84:276–313

Xu X, Zhou Y, Feng Z, et al (2018) A Self-Supported λ-MnO2 Film Electrode used for Electrochemical Lithium Recovery from Brines. Chempluschem 83:521–528. https://doi.org/10.1002/cplu.201800185

Yang S, Zhang F, Ding H, et al (2018) Lithium Metal Extraction from Seawater. Joule 2:1648–1651. https://doi.org/https://doi.org/10.1016/j.joule.2018.07.006

Yoon H, Lee J, Kim S, Yoon J (2019) Review of concepts and applications of electrochemical ion separation (EIONS) process. Sep Purif Technol 215:190–207

Yu J, Fang D, Zhang H, et al (2020) Ocean Mining: A Fluidic Electrochemical Route for Lithium Extraction from Seawater. ACS Mater Lett 2:1662–1668. https://doi.org/10.1021/acsmaterialslett.0c00385

Zhang H, Du X, Ding S, et al (2019a) DFT calculations of the synergistic effect of λ-MnO 2 /graphene composites for electrochemical adsorption of lithium ions. Physical Chemistry Chemical Physics 21:8133–8140. https://doi.org/10.1039/c9cp00714h

Zhang Y, Hu Y, Wang L, Sun W (2019b) Systematic review of lithium extraction from salt-lake brines via precipitation approaches. Miner Eng 139:105868. https://doi.org/https://doi.org/10.1016/j.mineng.2019.105868

Zhao A, Liu J, Ai X, et al (2019) Highly Selective and Pollution-Free Electrochemical Extraction of Lithium by a Polyaniline/Li x Mn 2 O 4 Cell. ChemSusChem 12:1361–1367. https://doi.org/10.1002/cssc.201803045

Zhao MY, Ji ZY, Zhang YG, et al (2017) Study on lithium extraction from brines based on LiMn2O4/Li1-xMn2O4 by electrochemical method. Electrochim Acta 252:350–361. https://doi.org/10.1016/j.electacta.2017.08.178

Zhao X, Feng M, Jiao Y, et al (2020a) Lithium extraction from brine in an ionic selective desalination battery. Desalination 481:. https://doi.org/10.1016/j.desal.2020.114360

Zhao X, Jiao Y, Xue P, et al (2020b) Efficient Lithium Extraction from Brine Using a Three-Dimensional Nanostructured Hybrid Inorganic-Gel Framework Electrode. ACS Sustain Chem Eng 8:4827–4837. https://doi.org/10.1021/acssuschemeng.9b07644

Zhao X, Li G, Feng M, Wang Y (2020c) Semi-continuous electrochemical extraction of lithium from brine using CF-NMMO/AC asymmetric hybrid capacitors. Electrochim Acta 331:. https://doi.org/10.1016/j.electacta.2019.135285

Zhao X, Yang S, Hou Y, et al (2023) Recent progress on key materials and

technical approaches for electrochemical lithium extraction processes. Desalination 546:116189. https://doi.org/https://doi.org/10.1016/j.desal.2022.116189

Zhao Z, Si X, Liu X, et al (2013) Li extraction from high Mg/Li ratio brine with LiFePO4/FePO 4 as electrode materials. Hydrometallurgy 133:75–83. https://doi.org/10.1016/j.hydromet.2012.11.013

국문 초록

기후위기가 실제로 눈앞에 찾아옴에 따라 온실가스를 배출하지 않는 탄소중립 엔지니어링 기반 기술의 도입이 필수적이며, 전기화학적 이온 분리 (electrochemical ion separation, EIONS) 기술은 그 중 수자원 및 염 확보를 위한 친환경적인 기술이다. 한편, 전기자동차 시장의 폭발적 성장으로 인해 리튬 수요 또한 폭증하고 있어 리튬 수급이 불안정해지고 있다. 이에 대응하기 위해선 기존 기술 대비 빠른 리튬 생산 방식의 개발이 필요하다.

전기화학적 리튬 회수 (electrochemical lithium recovery, ELR) 기술은 이 조건에 만족하는 EIONS 기술이다. ELR 기술이 기술적 우위를 가지는 대체 기술이 되기 위해서는 빠르게 리튬을 회수할 수 있고 급변하는 리튬 수요에 탄력적으로 대응할 수 있는 연속 생산 공정으로 구성되어야 한다. 하지만 기존의 선행 연구는 회분식 구성 하에 새로운 전극 쌍 구성을 제안하는 개념 증명 단계에 머물러 있으며, 연속식 구성에 대한 체계적인 고찰은 거의 없는 상황이다. 본 연구에서는 연속식 구성을 선도적으로 ELR 기술에 도입하여 새로운 시스템과 반응기의 형태를 개발하였다.

첫째, 연속적인 리튬 회수를 위한 연속 교반 탱크 반응기 기반의 대용량 ELR 시스템을 고안하였고 실제 해수담수화 농축수를 처리하는 후공정으로 구현하였다. 전극 탱크반응조를 옮겨 다니며 전해질 환경을 전환할 수 있는 모빌형 전극 구

성 방법을 개발하여 고농도의 불순물을 포함하는 해수담수화 농축수에서 리튬을 더 높은 순도로 회수하고, 시스템을 자동화할 수 있었으며, 전극의 유지 보수를 용이하게 하였다.

둘째, 흡착/탈착 단계를 통합하고 정전류 모드 하에서 운전되는 완전 연속식 시스템인 'LMO 기반 흐름식 흔들의자 ELR 시스템'을 최초로 제안하고 구현하였다. 새로운 시스템의 해석을 위해 기존에 일차원 상에서만 이루어지던 전산 시뮬레이션을 이차원 기반으로 확장하였으며, 3가지 물리적 전극 변수들의 성능에의 영향을 분석하여 전극 설계 가이드라인을 제시하였다.

본 연구에서는 ELR 시스템의 잠재적인 이점인 연속식 구성으로서의 활용 가능성을 확인하고, 공학적 반응기 설계를 통해 선도적으로 연속식 ELR 시스템을 구현했다는데 의의가 있다. 본 연구에서 개발한 공학적 설계방식이 ELR 시스템의 기술적 성숙도를 향상시키고 추후 기술의 상용화에 도움을 줄 수 있길 기대한다.

주요어: 전기화학적 이온 분리; 전기화학적 리튬 회수; 연속식; 공학적 설계; 모빌형 전극구성; 전극 설계 가이드라인

학번: 2016-24679